FIELD OF SCIENCE ENGINEERING AND TECHNOLOGY

SCIENTIFIC DISCIPLINE ENVIRONMENTAL ENGINEERING, MINING AND ENERGY

DOCTORAL DISSERTATION

Plasma-catalytic coupling in a ns pulsed discharge for the DRM reaction

Author: Marzia Faedda

First supervisor: Prof. Monika Motak
Second supervisor: Prof. Paolo Tosi
Assisting supervisor: Dr. Eng. Bogdan Samojeden

Completed in: AGH University of Krakow, Faculty of Energy and Fuels
University of Trento, Faculty of Physics

Kraków, 2025

AGH UNIVERSITY OF KRAKOW

UNIVERSITÀ DI TRENTO

The research presented in this PhD Thesis is part of a co-tutelle agreement between the AGH University of Krakow and the University of Trento.

This project has received funding from the European Union's Horizon 2020 research and innovation programme under the Marie Skłodowska-Curie grant agreement No 813393.

Abstract

In recent years, a continuous increase in carbon dioxide (CO_2) emissions has been observed in both the energy sector and the cement and metallurgical industries. While CO_2 emissions from the energy sector can be reduced, the issue of emissions from the cement and metallurgical industries remains unresolved. The dry reforming of methane (DRM) reaction converts equimolar amounts of CH_4 and CO_2 into syngas, a valuable mixture of carbon monoxide and hydrogen. With an H_2/CO ratio close to 1, DRM is an ideal process for the production of synthetic liquid hydrocarbons via the Fischer-Tropsch reaction. Despite its advantages, DRM technology struggles to achieve industrial maturity. High activation temperatures (above 700°C) and the endothermic nature of the process result in low energy efficiency. Furthermore, the high operating temperatures contribute to catalyst deactivation due to sintering and/or carbon deposition.

A parallel strategy for reducing CO_2 emissions in the energy sector through the use of renewable energy sources is also not without challenges. These sources (e.g., wind turbines, photovoltaics) are dependent on atmospheric conditions and operate intermittently. Improving the efficiency of renewable energy sources is possible through the use of high-performance energy storage systems, which allow for the accumulation of excess energy produced during peak weather conditions and its utilization during periods of increased demand.

One of the proposed approaches for managing surplus energy is its utilization in the production of valuable chemicals, such as through an endothermic reaction. One such process is the dry reforming of methane (DRM), which enables the production of syngas with an H_2:CO ratio of 1:1, aligning with the carbon capture and utilization (CCU) strategy. Additionally, the application of activation energy-reducing techniques, such as non-thermal plasma (NTP), can enhance the efficiency of the reaction. Plasma can respond to variations in available energy since it can be rapidly switched on and off. NTP operates outside thermal equilibrium, meaning that the kinetic energy of electrons can be significantly higher than that of heavier particles. This enables thermodynamically unfavorable reactions, such as DRM, while maintaining the gas temperature close to ambient conditions. Experimental studies on DRM under plasma conditions have demonstrated higher energy efficiency compared to thermal processes; however, they are characterized by lower conversion rates and reduced selectivity toward syngas.

The combination of plasma and catalysis exhibits synergistic effects that help overcome the limitations of both techniques. However, a fundamental understanding of the underlying processes and the interactions between plasma and the catalyst is still lacking. Most studies utilize dielectric barrier discharge (DBD) plasma since it allows the catalyst to be placed directly within the plasma reaction zone. Nevertheless, more efficient plasma sources, such as gliding arc discharge, microwave discharges, and nanosecond repetitive

pulsed discharges (NRP), need to be explored. The coupling of these plasma sources with a catalyst presents a complex challenge and constitutes an entirely new research area.

This study investigates the effect of NRP discharge in a DRM reaction system using supported nickel-based catalysts. The selected nickel catalysts were previously tested in high-temperature catalytic reactions and demonstrated the highest activity and selectivity [1]. The plasma discharge, previously characterized in DRM studies by Scapinello and Montesano, is a pin-to-pin discharge operating at atmospheric pressure. NRP plasma has gained increasing attention as one of the most energy-efficient methods for promoting chemical reactions, leveraging high electron densities and high electron energies achievable in this process.

The mechanism of NRP discharge involves the repetition of very short high-voltage pulses at kHz frequencies between two electrodes. The pulse duration typically ranges from 4 to 10 ns, with voltage amplitudes on the order of tens of kV and an electrode gap of several millimeters. As a result, the gas temperature can easily exceed 4000 K, making catalyst application feasible only in a post-plasma catalytic mode. The objective of this study was to develop a series of supported nickel catalysts, evaluate their performance in NRP plasma-activated DRM, and analyze the efficiency of the process under these conditions. Two types of catalysts were synthesized: nickel catalysts based on hydrotalcite (NiHT) and alumina (Ni/Al_2O_3), with nickel loadings ranging from 5% to 40% by weight. The active material (Ni) was introduced via co-precipitation (for NiHT) and incipient wetness impregnation or adsorption (for Ni/Al_2O_3). To investigate the influence of foam composition, two support materials were compared: $Y_2O_3-ZrO_2$ and α-Al_2O_3. Additionally, α-Al_2O_3 foam was functionalized by impregnation with γ-Al_2O_3 and 15% by weight of Ni/γ-Al_2O_3 to assess the contribution of the catalyst on the foam surface. The obtained catalytic materials were characterized using XRD, FTIR, CO_2-TPD, low-temperature nitrogen adsorption, and H_2-TPR. DRM experiments were conducted under atmospheric pressure at a CH_4:CO_2 ratio of 1:1. Performance parameters were evaluated as a function of the specific energy input (SEI).

The results indicated that the placement of the catalytic bed too far from the plasma source (in a post-plasma position) did not lead to improved activity. The distance of the catalyst from the active plasma zone significantly limited the interaction between plasma-activated reactants and the catalyst surface. Thermal activation was not feasible since the catalytic bed remained below 100°C. These findings suggest that a serial arrangement of the catalyst with the plasma reactor is insufficient, and various configurations should be explored to enhance catalyst-plasma interactions. The study of discharge limitations was conducted to address issues observed when positioning the catalyst in the post-plasma region. To this end, catalysts supported on monolithic foam carriers in a coaxial geometry were investigated. This configuration was designed to position the catalyst closer to the plasma discharge, enhancing the interaction between plasma-activated reactants and the catalyst surface. The structure of the ceramic monolithic foam was obtained via polyurethane foam replication, enabling the production of a material with controlled porosity and geometry. The foam formed a hollow cylinder surrounding the discharge in a coaxial configuration. The proximity of the foam to the active plasma zone facilitated exposure to reactants and indirect heating by plasma. It was hypothesized that this dual activation mechanism, combining thermal and plasma effects, would enhance catalytic performance.

A critical aspect of the experimental design was the ability to regulate the foam temperature while maintaining a constant SEI. This was achieved by proportionally adjusting the discharge power and reactant

flow rate. The external temperature of the foam surface was measured using a calibrated IR thermal camera, allowing for correlation with conversion and selectivity results.

Experimental results demonstrated that the presence of foam improved DRM performance compared to plasma alone. Both $Y_2O_3-ZrO_2$ and α-Al_2O_3 supports exhibited a linear increase in CO_2 and CH_4 conversion with rising temperature, surpassing the performance of plasma-only conditions. However, the foam composition was not a differentiating factor. The presence of foams also affected product selectivity, reducing CO production and shifting toward acetylene formation as a byproduct instead of ethane and ethene. Notably, these effects were observed even in the case of uncoated foam structures, suggesting that the foam itself plays a key role in modifying the plasma-catalytic process. These findings indicate that foam application influences the reaction through:

- temperature moderation,
- altered gas flow dynamics,
- enhanced surface interactions.

Further research on discharge limitations was extended to address the constraints of monolithic catalysts in favor of powdered catalysts. A novel "quartz wool nest" structure was developed to integrate powdered catalysts with plasma discharge in a coaxial geometry. This configuration was designed to leverage the high surface area and versatile compositional possibilities offered by powdered catalysts. Experimental results demonstrated that the presence of the "quartz wool nest" structure, regardless of catalyst loading, nearly doubled the CO_2 and CH_4 conversion rate compared to plasma alone. Future research should focus on optimizing catalyst composition and elucidating the complex interaction between plasma physics and surface chemistry in this novel configuration.

Streszczenie

W ostatnich latach obserwuje się ciągły wzrost emisji dwutlenku węgla (CO_2) zarówno z sektora energetycznego, jak i przemysłu cementowego oraz metalurgicznego. O ile emisje z energetyki mogą być zredukowane, o tyle problem emisji z przemysłu cementowego i metalurgicznego pozostaje nierozwiązany. Reakcja suchego reformingu metanu (DRM, ang. Dry Reforming of Methane) przekształca równomolowe ilości CH_4 i CO_2 w gaz syntezowy – wartościową mieszaninę tlenku węgla i wodoru. Przy stosunku H_2/CO bliskim 1, DRM jest idealnym procesem do produkcji syntetycznych węglowodorów ciekłych poprzez reakcję Fischera-Tropscha. Mimo swoich zalet, technologia DRM z trudem osiąga dojrzałość przemysłową. Wysokie temperatury aktywacji (powyżej 700°C) i endotermiczny charakter procesu skutkują niską wydajnością energetyczną. Ponadto, wysokie temperatury pracy przyczyniają się do dezaktywacji katalizatora w wyniku jego spiekania i/lub koksowania.

Równolegle stosowana strategia obniżenia emisji CO_2 w energetyce poprzez wykorzystanie źródeł odnawialnych również nie jest doskonała. Źródła te (wiatraki, fotowoltaika itp.) są zależne od warunków atmosferycznych i charakteryzują się niestabilną pracą. Poprawa efektywności odnawialnych źródeł energii jest możliwa poprzez zastosowanie wydajnych magazynów energii, które umożliwią gromadzenie nadmiaru energii produkowanej w szczytowych okresach pogodowych i jej wykorzystanie w momentach wzmożonego zapotrzebowania.

Jednym z pomysłów na zagospodarowanie nadmiaru energii jest jej wykorzystanie do produkcji wartościowych chemikaliów, np. w reakcji endotermicznej. Do takich procesów należy reakcja suchego reformingu metanu (DRM). Takie podejście pozwala na uzyskanie wartościowego produktu, jakim jest gaz syntezowy o stosunku H_2:CO = 1:1, co wpisuje się w strategię CCU (Carbon Capture and Utilization). Dodatkowo, zastosowanie technik obniżających energię aktywacji, takich jak plazma niskotemperaturowa (NTP, ang. Non-Thermal Plasma), może zwiększyć efektywność reakcji. Plazma może reagować na zmienność dostępnej energii, ponieważ może być szybko włączana i wyłączana. NTP działa poza równowagą termiczną, co oznacza, że energia kinetyczna elektronów może być znacznie wyższa niż energia cięższych cząstek. Dzięki temu możliwe są reakcje termodynamicznie niekorzystne, takie jak DRM, przy jednoczesnym utrzymaniu temperatury gazu na poziomie zbliżonym do temperatury pokojowej. Eksperymenty nad DRM w warunkach plazmowych wykazują wyższą wydajność energetyczną w porównaniu z procesami termicznymi, jednakże charakteryzują się niższą konwersją i niższą selektywnością w kierunku gazu syntezowego Połączenie plazmy i katalizy wykazuje efekty synergiczne, które pozwalają przezwyciężyć niedoskonałości obu technik. Jednak nadal brakuje fundamentalnego zrozumienia zachodzących procesów oraz wzajemnych interakcji między plazmą a katalizatorem.

Większość badań prowadzona jest z wykorzystaniem plazmy wyładowania barierowego (DBD, ang. Dielectric Barrier Discharge), ponieważ umożliwia ona umieszczenie katalizatora bezpośrednio wewnątrz obszaru reakcji plazmowej. Niemniej jednak, konieczne jest zbadanie bardziej wydajnych źródeł plazmy, takich jak łuk ślizgowy, mikrofalowe wyładowania oraz nanosekundowe wyładowania impulsowe (NRP, ang. Nanosecond Repetitive Pulsed Discharges). Sprzężenie tych źródeł z katalizatorem jest złożonym zagadnieniem i stanowi całkowicie nowe wyzwanie badawcze. W niniejszej pracy zbadano wpływ zastosowania wyładowania NRP w układzie reakcji DRM z użyciem nośnikowych katalizatorów niklowych. Do testów wybrano katalizatory niklowe, wcześniej przebadane w wysokotemperaturowej reakcji katalitycznej, które wykazywały najwyższą aktywność i selektywność [Dębek et al.].

Wyładowanie plazmowe, wcześniej scharakteryzowane w kontekście reakcji DRM w pracach Scapinello i Montesano, jest wyładowaniem typu pin-to-pin działającym przy ciśnieniu atmosferycznym. Plazma wyładowania NRP zyskuje coraz większe zainteresowanie jako jedna z najbardziej energooszczędnych metod inicjowania reakcji chemicznych, wykorzystując wysokie gęstości oraz energie elektronów osiągalne w tym procesie. Mechanizm działania NRP polega na powtarzaniu, z częstotliwościami rzędu kHz, bardzo krótkich impulsów wysokiego napięcia ustanawianych między dwiema elektrodami. Czas trwania impulsu wynosi zazwyczaj od 4 do 10 ns, przy amplitudzie napięcia rzędu kilkudziesięciu kV i odległości między elektrodami wynoszącej kilka milimetrów. W rezultacie temperatura gazu może łatwo wzrosnąć powyżej 4000 K, co sprawia, że zastosowanie katalizatorów jest możliwe jedynie w trybie katalizy post-plazmowej.

Celem pracy było opracowanie serii nośnikowych katalizatorów niklowych, ich przetestowanie w reakcji suchego reformingu metanu aktywowanej plazmą NRP oraz analiza efektywności tak prowadzonego procesu. Zsyntetyzowano dwa rodzaje katalizatorów: katalizatory niklowe na bazie hydrotalkitu (NiHT) oraz na bazie tlenku glinu (Ni/Al_2O_3), z zawartością niklu w zakresie od 5% do 40% mas. Materiał aktywny (Ni) wprowadzono metodą współstrącania (dla NiHT) oraz impregnacji pierwszej wilgotności lub adsorpcji (dla Ni/Al_2O_3). Aby zbadać wpływ składu pianki, porównano dwa materiały nośne: $Y_2O_3-ZrO_2$ oraz α-Al_2O_3. Dodatkowo, pianka α-Al_2O_3 została funkcjonalizowana poprzez impregnację γ-Al_2O_3 oraz 15% mas. Ni/γ-Al_2O_3, aby zbadać wpływ katalizatora na powierzchni pianki. Tak otrzymane materiały katalityczne scharakteryzowano metodami XRD, FTIR, CO_2-TPD, niskotemperaturowej sorpcji azotu oraz H_2-TPR.

Eksperymenty DRM przeprowadzono przy ciśnieniu atmosferycznym oraz stosunku CH_4:CO_2 równym 1:1. Parametry wydajności badano w funkcji jednostkowego zużycia energii (specific energy input, SEI). Otrzymane wyniki wykazały, że zastosowanie złoża katalitycznego umieszczonego zbyt daleko od źródła plazmy (w pozycji post-plazmowej) nie prowadzi do poprawy aktywności. Odległość katalizatora od aktywnego obszaru plazmy znacząco ograniczała interakcje między reagentami aktywowanymi przez plazmę a powierzchnią katalizatora.

Aktywacja termiczna nie była możliwa, ponieważ temperatura złoża katalitycznego pozostawała poniżej 100°C. Wyniki te sugerują, że szeregowe umieszczenie katalizatora względem reaktora plazmowego nie jest wystarczające i konieczne jest zbadanie różnych konfiguracji, w których katalizator może wchodzić w bliższą interakcję z plazmą. Badanie ograniczenia wyładowania przeprowadzono w celu rozwiązania problemów zaobserwowanych przy umieszczeniu katalizatora w pozycji post-plazmowej. W tym celu zbadano

katalizatory osadzone na nośnikach z pianki monolitycznej w geometrii współosiowej. Konfiguracja ta została zaprojektowana tak, aby umieścić katalizator bliżej wyładowania plazmowego, co miało na celu zwiększenie interakcji między reagentami aktywowanymi przez plazmę a powierzchnią katalizatora. Strukturę ceramicznej pianki monolitycznej otrzymano metodą replikacji pianki poliuretanowej, która pozwoliła na uzyskanie materiału o wybranej porowatości i geometrii. Pianka miała formę pustego cylindra otaczającego wyładowanie w konfiguracji współosiowej. Bliskość pianki do aktywnego obszaru plazmy ułatwiała ekspozycję katalizatora na reagenty oraz umożliwiała jego pośrednie ogrzewanie przez plazmę. Zakładano, że ten podwójny mechanizm aktywacji, łączący efekty termiczne i plazmowe, zwiększy wydajność katalityczną.

Krytycznym aspektem projektu eksperymentalnego była możliwość moderowania temperatury pianki przy jednoczesnym zachowaniu stałej wartości SEI. Osiągnięto to poprzez proporcjonalne dostosowanie mocy wyładowania oraz przepływu reagentów. Do pomiaru temperatury zewnętrznej powierzchni pianki użyto skalibrowanej termokamery IR, co umożliwiło korelację wyników pomiarów temperatury z konwersją oraz selektywnością reakcji. Wyniki eksperymentalne wykazały, że obecność pianki poprawiła wydajność DRM w porównaniu z samą plazmą. Zarówno nośniki $Y_2O_3-ZrO_2$, jak i α-Al_2O_3 wykazywały liniowy wzrost konwersji CO_2 i CH_4 wraz ze wzrostem temperatury, przewyższając warunki samej plazmy. Jednakże skład pianki nie był czynnikiem różnicującym. Obecność pianek wpłynęła także na selektywność produktów, powodując spadek produkcji CO oraz przesunięcie w kierunku powstawania acetylenu jako produktu ubocznego, zamiast etanu i etenu. Co istotne, efekty te zaobserwowano nawet w przypadku niepowlekanych struktur piankowych, co sugeruje, że sama pianka odgrywa kluczową rolę w modyfikowaniu procesu plazmo-katalitycznego. Wyniki te wskazują, że zastosowanie pianki wpływa na reakcję poprzez:

- moderowanie temperatury,
- zmianę dynamiki przepływu gazu,
- wzmocnienie oddziaływań powierzchniowych.

W dalszej części badań ograniczenie wyładowania rozszerzono, koncentrując się na rozwiązaniu ograniczeń katalizatorów monolitycznych poprzez zastosowanie katalizatorów proszkowych. W tym celu opracowano nową strukturę „gniazda z waty kwarcowej", umożliwiającą integrację katalizatorów proszkowych z wyładowaniem plazmowym w geometrii współosiowej. Konfiguracja ta została zaprojektowana w celu wykorzystania wysokiej powierzchni właściwej oraz wszechstronnych możliwości doboru składu oferowanych przez katalizatory proszkowe.

Wyniki eksperymentalne wykazały, że obecność struktury „gniazda z waty kwarcowej", niezależnie od załadunku katalizatora, niemal podwoiła szybkość konwersji CO_2 i CH_4 w porównaniu z samą plazmą. Głównym produktem reakcji we wszystkich konfiguracjach pozostawał gaz syntezowy (H_2 i CO), bez znaczących zmian w selektywności. Ilość węglowodorów C_2-C_3 została zmniejszona na rzecz zwiększonej produkcji wody. Obecność katalizatora Ni zmniejszyła selektywność w kierunku acetylenu, prawdopodobnie z powodu osadzania się węgla. Zwiększona aktywność związana ze strukturą „gniazda" może wynikać z podwyższonej temperatury w ograniczonej objętości, wzmocnionych oddziaływań powierzchniowych i/lub zmienionej dynamiki przepływu reagentów. Struktura ta stanowi obiecujący krok naprzód w projektowaniu

reaktorów plazmo-katalitycznych, ponieważ oferuje elastyczną platformę do testowania różnych składów katalizatorów oraz poprawy wydajności wyładowania NRP.

Przyszłe badania powinny skupić się na optymalizacji składu katalizatora oraz wyjaśnieniu złożonej interakcji między fizyką plazmy a chemią powierzchni w tej nowatorskiej konfiguracji.

Contents

Summary

The structure of the thesis is organised as follows:

- Chapter 1 introduces the problem of CO_2 emissions and climate change, discussing the strategies that are currently in use for its utilization. Among these strategies we present the dry reforming of methane (DRM) reaction, object of this thesis.
- Chapter 2 presents the topic of plasma-catalysis, explaining why it is a promising technique for the efficient CO_2 conversion. A short review of the literature on plasma-catalytic coupling for the DRM reaction is given.
- Chapter 3 presents this thesis work, explaining the motivations and the aim of the research.
- Chapter 4 is a compendium of the methods used in this work. The catalyst characterisation techniques are introduced, together with the plasma-catalytic experimental setup and the plasma diagnostics. The analytical methods are also explained.
- Chapter 5 describes the synthesis of the hydrotalcite-derived Ni-Mg-Al mixed oxides powder catalysts and the powder Ni/Al_2O_3 catalysts. The catalysts are characterised with multiple techniques and are used in the downstream configuration for the DRM reaction with the NRP discharge. Conversion and selectivity results are reported as a function of the energy input.
- Chapter 6 explores the synthesis, functionalisation, optimisation and use of monolith foam catalysts. Two types of foam supports were studied for comparison: α-Al_2O_3 and yttria-stabilised zirconia (YSZ) $Y_2O_3-ZrO_2$, which were synthesised as a replica of polyurethane foams. Then, the α-Al_2O_3 foam was functionalised with the impregnation of a Ni/γ-Al_2O_3 catalyst. Both supports and the impregnated catalyst foam were studied in the plasma-catalytic coupling. The DRM performance parameters were here evaluated as a function of the temperature reached by the foam by indirect heating.
- Chapter 7 is the study of a new structure for the coupling of powder catalysts in a co-axial way, similar to that of the monolith foams. The design process is explained, and the powder Ni/Al_2O_3 catalysts performance is evaluated in the DRM plasma-catalytic coupling.
- Chapter 8 closes the thesis with concluding remarks and future perspectives of this application.

Chapter 1

Introduction

1.1 The Environmental Challenge of Climate Change

Climate change remains one of the most pressing global challenges of our time. The Intergovernmental Panel on Climate Change (IPCC) has emphasised that human activities have unequivocally caused global warming, with observed increases in greenhouse gas (GHG) concentrations since 1750 far exceeding natural variations over multiple millennia [2]. The primary driver of this phenomenon is the increasing concentration of GHGs in the atmosphere. Carbon dioxide (CO_2) is the most significant contributor, accounting for approximately 75% of global GHG emissions in 2022.

According to recent data, annual global CO_2 emissions reached 37.4 billion tonnes in 2023 [3], rebounding from a temporary dip in 2020 due to the COVID-19 pandemic. The measured global monthly mean of CO_2 concentration as of May 2024 is 423.4 ppm [4]. This figure represents a new record high, surpassing pre-pandemic levels and underscoring the urgent need for effective mitigation strategies. CO_2 is released primarily through the burning of fossil fuels (coal, oil, and natural gas) for energy production, the industry and transportation sectors, accounting for about 73% of global emissions. Industrial processes, such as cement production, contribute approximately 5.2%, while land-use changes and deforestation add another 18.4% [5]. CO_2 persists in the atmosphere for centuries, with an estimated atmospheric lifetime of 300 to 1000 years.

Methane, another potent greenhouse gas, has also seen significant global level increase, despite the negative trend in Europe and the US. Global methane emissions reached 10.49 billion tonnes in 2022, with human activities contributing about 60% of this total [6]. Figure 1.1 shows the distribution of methane emission sources in the year 2023, highlighting those that come from human activities. The largest contribution among human-related activities comes from agriculture (142 Mt), immediately followed by the energy sector ($\sim$ 130 Mt). Here, methane emissions are generated from oil production activities (50 Mt), followed by coal extraction (40 Mt), the natural gas supply chain and by the incomplete combustion of bioenergy (10 Mt). A wasteful practice worth mentioning is the use of gas flaring, consisting in the combustion of associated petroleum gas that comes with oil production. Flaring causes emissions of CO2, methane and black soot in the atmosphere, and its effects have a profound negative impact on the environment and on human and animal health. Methane's impact as a GHG can be determined using two parameters: the amount of time

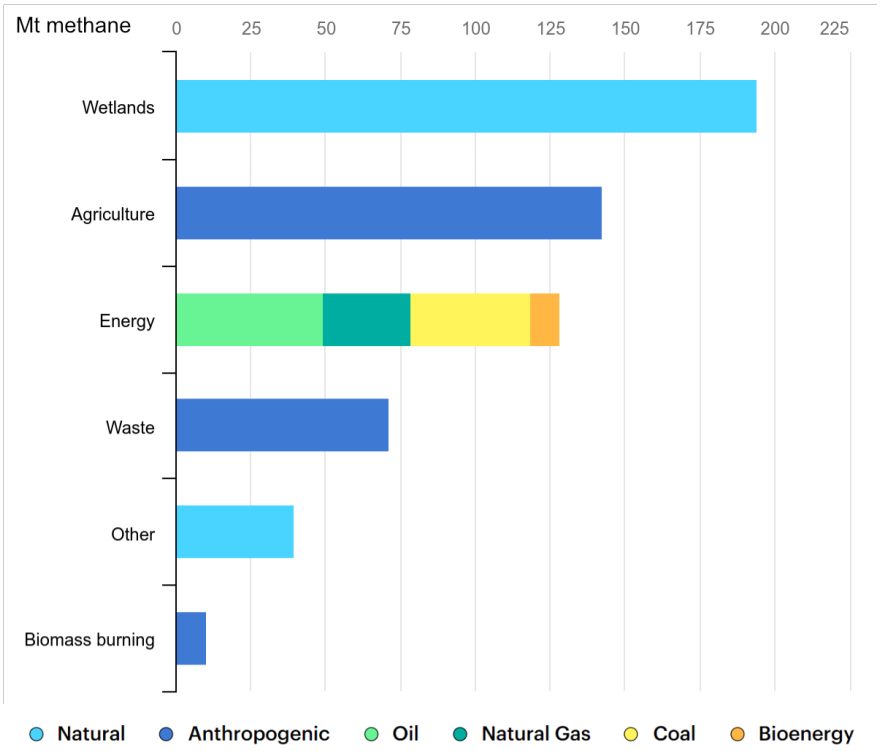

Figure 1.1. IEA (2024), Sources of methane emissions, 2023, IEA, Paris https://www.iea.org/data-and-statistics/charts/sources-of-methane-emissions-2023-2, Licence: CC BY 4.0

it remains in the atmosphere and its capacity to absorb energy. Methane has a much shorter lifespan in the atmosphere compared to carbon dioxide: an average of 12 years, after which it breaks down into less potent GHGs. For comparison, CO_2 can remain in the atmosphere for over a century. Nevertheless, methane's energy absorption capacity is significantly higher, leading to a global warming potential (GWP) of 82-87 times that of CO_2 over a 20-year period, or about 30 times over a 100-year period [6]. As a result, reduction of methane emissions can be one of the most effective ways to slow the rate of climate change and to meet the requirement to stay below the limit of 1.5 degrees compared to pre-industrial levels.

The impacts of these elevated GHG levels are far-reaching. They include rising global temperatures, more frequent extreme weather events, sea level rise, and ocean acidification. These changes pose significant threats to ecosystems, human and animal health, food security, and economic stability worldwide.

To address this challenge, there is an urgent need for innovative technologies that can mitigate GHG emissions. One promising approach is the development of methods to recycle or convert CO_2 and methane into valuable products. This strategy not only reduces atmospheric GHG levels but also creates economic opportunities by turning waste products into useful materials.

1.2 Carbon Capture, Utilisation and Storage (CCUS) Strategies

The urgency of reducing CO_2 emissions in the shortest term to avoid reaching 2°increase of the global average temperature and the projected scenarios that see us still depending primarily on fossil fuels until at least 2050 make it imperative to diversify the actions to tackle CO_2 emissions. Mitigation solutions have

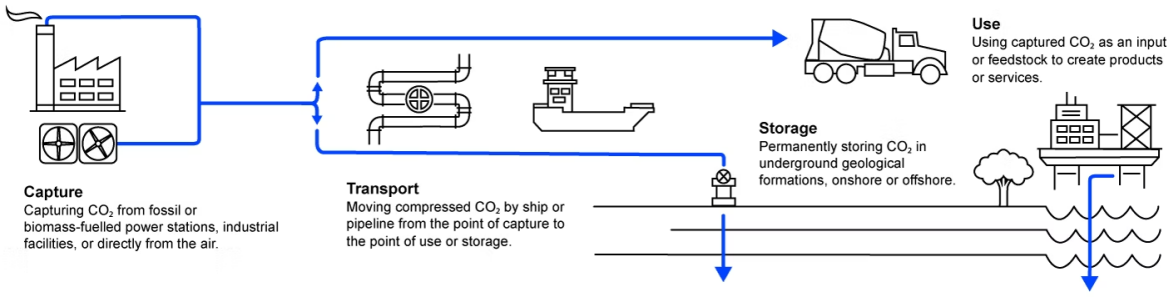

Figure 1.2. Schematic representing the main steps of the Carbon capture, utilisation and storage (CCUS) process. Source: IEA iea.org. Licence: CC BY 4.0.

gained a central role in this strategy, without which we would not be able to reach the target of limiting GHG concentrations. In this context, Carbon capture, utilisation and storage (CCUS) refers to a number of technologies and processes designed to sequestrate CO_2 from its emission sources or directly from the atmosphere, so that it is either reused or it is permanently stored (figure 1.2).

The vast majority of CO_2 emissions comes from large stationary sources, primarily power production plants and industrial processes, such as the manufacturing and construction industries. It is estimated that in 2005 these sources accounted for 60% of total CO_2 emission sources [7]. These are distinguished from small stationary sources, such as small boilers in residential locations or mobile sources, such as those of the transport sector. Carbon capture, utilisation and storage (CCUS) technologies are more likely to be implemented in the first category, where large volumes of gas exhaust can be utilised.

To better understand where CCUS technologies can be implemented, we take a look at the distribution of electricity production sources worldwide and in the European Union (EU) countries. The distribution in the year 2022 is shown in figure 1.3 (own developement, based on data from [8]). In the graphs, electricity production from renewable sources (including nuclear energy production) is enclosed in a box for emphasis. While the world average relies on renewables for less than 40%, the EU has a share of 61%, with nuclear (22%) and wind (15%) being the major contributors. As for fossil sources, coal remains the dominant fuel worldwide, accounting for almost 36% of electricity generated, and the second fossil fuel in EU, with a share of 16%. Natural gas contributes for 22.5% worldwide and 19% in the EU, while oil for less than 3% worldwide and 3.8% in the EU.

Among CCUS technologies we can distinguish between the ones that focus on its storage (CCS) and the ones that focus on its utilisation (CCU). Both technologies rely on a first stage of CO_2 separation from the waste gas, which is what will be discussed in the next section.

1.2.1 CO_2 capture technologies

The CO_2 capture stage is a critical component of both CCS and CCU technologies, constituting 70-80% of the total cost [9]. It involves separating CO_2 from other gases in industrial processes or power generation. There are several methods for CO_2 capture, each with its own advantages and challenges.

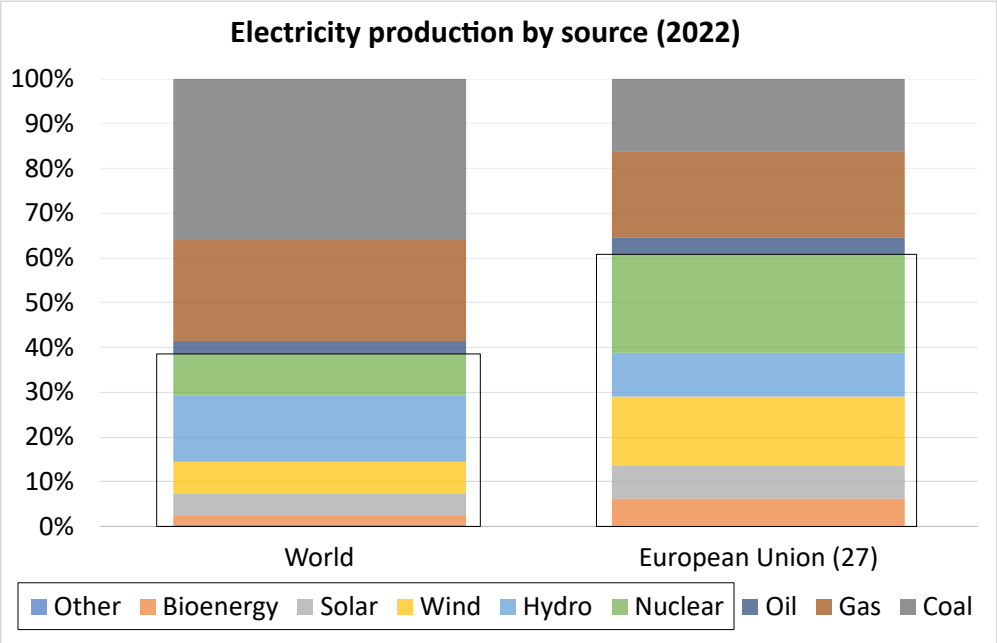

Figure 1.3. Electricity production by source in 2022 worldwide (left) and in EU (right). Data source: Ember (2024) – with major processing by Our World in Data. "Electricity generation from bioenergy – Ember and Energy Institute". Ember, "Yearly Electricity Data".

Post-combustion capture removes CO_2 from flue gases after combustion of fossil fuels or biomass. It's the most mature technology to date, with a TRL of 9[1] and can be integrated in existing plants [10]. The most common technique uses chemical absorption with amine solvents. However, it faces challenges of high energy consumption for solvent regeneration and solvent degradation [11].

Pre-combustion capture is meant to decarbonise the fuel before combustion. After impurities are removed, hydrocarbons are either combined with oxygen for gasification reaction (equation (1.1)), or they are combined with steam for a reforming reaction (equation (1.2)). These reactions both convert the fuel into a mixture of hydrogen and CO2, which goes under the name of synthesis gas (syngas).

$$C_nH_m + \frac{n}{2}O_2 \rightarrow \frac{m}{2}H_2 + nCO \tag{1.1}$$

$$C_nH_m + nH_2O \rightarrow \frac{n+m}{2}H_2 + nCO \tag{1.2}$$

The syngas produced is transferred to another reactor to undergo Water-Gas Shift Reaction (WGSR) (equation (1.3)), which eventually produces CO_2 and hydrogen.

$$CO + H_2O \rightarrow CO_2 + H_2 \tag{1.3}$$

[1]Technology Readiness Level (TRL) is a method to estimate the maturity of a technology, developed by NASA in the 1970s. The technology is classified on a scale from 1 to 9, where 1 is equivalent to the R&D stage and 9 means the system is mature and is proven in an operational environment.

The CO_2 is then separated, leaving hydrogen to be used as a carbon-free fuel. This method is typically used in integrated gasification combined cycle (IGCC) power plants. It offers higher CO_2 concentration streams, potentially reducing capture costs, but requires significant modifications to existing plants [12].

Oxy-fuel combustion is an early-stage process that involves burning fuel in pure oxygen rather than air, resulting in a flue gas composed mainly of CO_2 and water vapour (equation (1.4)). While it produces a high-purity CO_2 stream, the process of separating oxygen from air is energy-intensive and the large oxygen consumption makes it costly.

$$C_xH_y + (x + \frac{y}{4})O_2 \rightarrow xCO_2 + \frac{y}{2}H_2O \tag{1.4}$$

Chemical looping combustion (CLC) can be considered a form of advanced oxy-fuel combustion and a pre-combustion technique at the same time. It uses a metal oxide as an oxygen carrier to transfer oxygen from the combustion air to the fuel, avoiding direct contact between them. The process involves two interconnected reactors: in the fuel reactor, the metal oxide is reduced by reacting with the fuel, producing CO_2 and water; in the air reactor, the reduced metal is re-oxidized by air. This cycle results in a high-purity stream of CO_2 that can be easily separated by condensing the water vapour.

$$\begin{gathered} Me_yO_{x-1} + \frac{1}{2}O_2 \rightleftharpoons Me_yO_x + Air \\ (2n+m)Me_yO_x + C_nH_{2m} \rightleftharpoons (2n+m)Me_yO_{x-1} +, H_2O + nCO_2 \end{gathered} \tag{1.5}$$

CLC has the potential to significantly reduce the energy and cost penalties associated with CO_2 capture in conventional combustion systems, but is still in the development stage and faces challenges related to oxygen carrier performance, reactor design, and scale-up [9].

Direct air capture (DAC) is an emerging technology that captures CO_2 directly from the atmosphere. While it offers flexibility in location, the low concentration of CO_2 in air (about 0.04%) makes the process energy-intensive and currently expensive [9].

Each of these methods has specific technical challenges, including energy efficiency, cost, and scalability. Ongoing research aims to improve existing technologies and develop new approaches to make CO_2 capture more efficient and cost-effective.

The choice of capture technology is often influenced by the CO_2 partial pressure in the waste gas stream. For instance, chemical absorption is typically used for low partial pressure streams, while physical absorption or membrane separation may be more suitable for higher partial pressure streams. Generally, the lower the CO_2 partial pressure in a gas stream, the more stringent and the conditions required for the separation process. The efficiency and cost-effectiveness of CO_2 capture processes are also heavily impacted by CO_2 partial pressure. This relationship is significant because it directly impacts the thermodynamic driving force for separation and the energy requirements of the capture process.

1.2.2 Carbon Storage

Carbon Capture and Storage (CCS) is defined as a technological process involving the collection and concentration of the CO_2 produced in industrial and energy related sources, transportation to a suitable storage site and storage for a long period of time and away from the atmosphere [13].

CCS is typically implemented in three main stages:

1. Capture: CO_2 is separated from other gases produced at large industrial process facilities or power plants, as described in the previous section (see section 1.2.1).

2. Transport: The captured CO_2 is compressed and transported via pipelines, ships, road or rail tankers to a storage site.

3. Storage: CO_2 is injected into deep underground geological formations for long-term storage. Common storage options include depleted oil and gas reservoirs, deep saline aquifers and unmineable coal seams.

The choice of storage site depends on various factors including geology, storage capacity, and proximity to CO_2 sources [10]. CCS implementation faces several challenges, including high costs, energy penalties, and public perception issues. However, it is considered a crucial technology for achieving significant CO_2 emission reductions, particularly in hard-to-abate sectors [12]. Ongoing research focuses on improving capture technologies, reducing costs, and ensuring the long-term security of CO_2 storage. The successful implementation of CCS will likely require supportive policy frameworks and economic incentives.

1.2.3 Carbon Utilisation

Carbon Capture and Utilisation (CCU) is a subset of CCUS technologies that focuses on the capture of CO_2 from industrial sources or the atmosphere and its subsequent conversion into valuable products or services.

Implementation of CCU typically involves three steps: capture, purification and compression for transportation or for immediate use and finally utilisation. CO_2 capture technologies have been discussed in section 1.2.1 of this thesis. Utilisation processes can be of different nature and can be classified as follows:

- *Chemical conversion*. CO_2 is used as a feedstock for producing value-added chemicals. These processes will be discussed in more detail in section 1.3. The most widespread methods for CO_2 recycling are the synthesis of urea for fertilizers production, production of methanol or other alcohols, CO_2 hydrogenation to methane, production of syngas via the dry reforming of methane reaction and the synthesis of polymers and plastics.

- *Biological conversion*. It involves using microorganisms or enzymes to convert CO_2 into organic compounds. Among these techniques we find algae cultivation for biofuels and biochemicals production [14] and microbial electrocatalysis for production of organic acids [15].

- *Mineralisation*. CO_2 is combined with metal oxides to form stable carbonate minerals, such as in accelerated weathering of rocks [16] or the production of construction materials [17].

- *Enhanced commodity production*. CO_2 is used to enhance the production of existing commodities, such as enhanced oil recovery (EOR) [18] and enhanced geothermal systems (EGS) [19].

- *Direct use*. CO_2 is used without conversion in applications such as carbonation in the food and beverage industry, or in greenhouses for enhancing plant growth.

CCU has potential benefits in creating economic value from CO_2 emissions and reducing the need for fossil-based raw materials. However, the scale of CO_2 utilisation is generally much smaller than the potential for geological storage in CCS [2].

It's worth noting that the environmental benefits of CCU depend on the energy intensity of the utilisation process and the lifetime of the products created. Therefore, life cycle assessments are crucial in evaluating the overall impact of CCU technologies.

1.3 CO_2 Conversion Reactions

Chemical conversion of CO_2 is a key area in carbon dioxide utilisation research due to its potential to create valuable products while mitigating CO_2 emissions. This process involves using CO_2 as a feedstock in chemical reactions to produce a variety of compounds. The main challenge in this field is represented by the energy efficiency of the process. Indeed, CO_2 is a very stable molecule constituted by a symmetrical double bond of the carbon atom with the two oxygen atoms. As a consequence, activating or breaking down CO_2 is a thermodynamically unfavourable process, where a large amount of energy is required. Catalysts are widely employed in these reactions to lower the activation energy barrier and improve reaction kinetics. Heterogeneous catalysts, in particular, offer advantages of easy separation and reusability, making them attractive for large-scale CO_2 conversion processes [20]. A brief overview of the main CO_2 conversion reactions is given in this section, with particular focus on the dry reforming of methane reaction.

1.3.1 Hydrogenation of CO_2

The majority of the chemical conversion processes for CO_2 utilisation belong to the group of CO_2 hydrogenation reactions [21], which involve the reaction of CO_2 with hydrogen to produce fuels or chemicals. In the former category we find CO_2 hydrogenation for the synthesis of methanol, dimethyl ether (DME) or hydrocarbons. Products belonging to the latter categories are instead methanol and formic acid.

The **methanation** of CO_2 consists in the catalytic hydrogenation of CO_2 to obtain methane and water. It is also known as *Sabatier reaction*.

$$CO_2 + 4\,H_2 \longrightarrow CH_4 + 2\,H_2O \qquad \Delta H_{298K} = -252.9 kJ/mol \tag{1.6}$$

This reaction is thermodinamically favourable at low reaction temperatures, but needs a catalyst to overcome its kinetic limitations and to achieve high selectivity. Ni-based catalysts are the most widely used [22, 23, 24], due to their low cost, availability and good catalytic performance. Among noble metals, Ru catalysts show high activity [25], but Rh [26] and Pd [27] are also found. The support material of the catalyst also plays a crucial role in its activity. Porous materials such as Al_2O_3, SiO_2, CeO_2 and zeolites are the preferred choices [28].

The **synthesis of methanol** by CO_2 hydrogenation equation (1.7) is another prominent example. Methanol is a versatile chemical with applications in fuel transportation and distribution when in the liquid state [29] and as a precursor for important chemicals, such as formaldehyde, acetic acd, methyl tertiary-butyl ether and dymethyl ether [30].

$$CO_2 + 3\,H_2 \rightleftharpoons CH_3OH + H_2O \qquad \Delta H_{298K} = -49.5 kJ/mol \tag{1.7}$$

Both homogeneous and heterogeneous catalysts are employed for this process. The most common heterogeneous catalysts are Cu/ZnO_2/Al_2O_3 based [31, 32]. However, CO_2 conversion still remains below 20% and co-production of water is an issue for catalyst sintering and deactivation.

The **Reverse Water-Gas Shift (RWGS)** reaction (eq. 1.8) is the inverse of the WGSR (eq. 1.3) and it provides a pathway to convert CO_2 into syngas. It can also be combined with other reactions such as the Fischer-Tropsch, to produce liquid fuels from CO2.

$$CO_2 + H_2 \rightarrow CO + H_2O \qquad \Delta H = 42.1 kJ mol^{-1} \tag{1.8}$$

This reaction is moderately endothermic, so it is favored at higher temperatures, but it is equilibrium limited, so catalysts are needed to improve its reaction rate and selectivity. Heterogeneous catalysts are widely used. Noble metals like Pt and Pd demonstrate high activity, but transition metals like Cu, Fe and Ni are also widely studied because of their cost-effectiveness [33, 34]. Common supports are metal oxides such as Al_2O_3, CeO_2 [35] and TiO_2, with reducible oxides like CeO_2 enhancing activity due to oxygen vacancies. Promoters are often added to improve CO_2 adsorption and selectivity. One of the main issuea remaina catalyst deactivation due to syntering and coking, particularly in Ni-based catalysts.

1.3.2 Urea synthesis

Urea is an essential fertiliser, widely employed in agriculture because of its high nitrogen content. Urea production currently constitutes the largest industrial use of CO2. The industrial process called *Bosch-Meiser* process, involves two consecutive reactions: the *Bazarov reaction* that converts CO_2 and ammonia (NH_3) into ammonium carbamate (eq.1.9) and a following reaction that dehydrates it and forms urea (eq. 1.10).

$$CO_2 + 2\,NH_3 \rightarrow NH_2COONH_4 \qquad \Delta H = -117 kJ/mol \text{ at 110 atm and 160°C} \tag{1.9}$$

$$NH_2COONH_4 \rightarrow NH_2CONH_2 + H_2O \qquad \Delta H = 15.5 kJ/mol \text{ at 160-180°C} \tag{1.10}$$

While the Bazarov reaction is fast and exothermic and it is usually performed at high temperature and pressure, the second reaction is slow and endothermic and needs a catalyst to increase the reaction rate. Multifunctional catalysts have been under developement stage to improve the rate-limiting step, which is the formation of the second C-N bond in urea, while breaking the C-O bond in carbamate [36]. Substances like water and ammonia can be exploited as homogeneous catalysts, and also soluble metal complexes. Cu(II) and Zn(II)-based catalysts are the most promising ones among the heterogeneous ones [37].

1.3.3 Dry Reforming of Methane

The Dry Reforming of Methane (DRM) reaction is a process that converts one mole of carbon dioxide and one mole of methane (CH4) into synthesis gas (eq. 1.11). The reaction is particularly appealing because it converts the two major greenhouse gases in a value-added gas mixture that can be further employed as a

feedstock for the production of important liquid fuels and chemicals. Through the Fischer-Tropsch process, in fact, syngas can be converted in turn into hydrocarbons and oxygenates such as methanol, acetone, but also paraffins and oleofins [38]. In particular, the syngas H_2/CO ratio of 1

$$CO_2 + CH_4 \rightarrow {}_2CO + 2\,H_2 \qquad \Delta H_{298K} = 247 kJ/mol \tag{1.11}$$

This reaction is highly endothermic, requiring significant energy input to dissociate the highly stable molecules. The temperatures that guarantee these conditions are above 600°C and the presence of a catalyst is fundamental to achieve reasonable reaction rates and selectivity. Indeed, several other reactions may occur in the same temperature range, diminishing DRM efficiency. Among them we can find the RWGS (eq.1.8), which is responsible for lowering the H_2/CO syngas ratio, and carbon-forming reactions, such as the Boudouard reaction (eq. 1.12), CO and CO_2 reduction (eq. 1.13 and 1.14) and CH_4 decomposition (eq. 1.15), that are responsible for catalyst coking and deactivation [39].

$$2\,CO \rightleftharpoons C + CO_2 \qquad \Delta H_{298K} = -171 kJ/mol \tag{1.12}$$

$$CO + H_2 \rightleftharpoons C + H_2O \qquad \Delta H_{298K} = -131 kJ/mol \tag{1.13}$$

$$CO_2 + 2\,H_2 \rightleftharpoons C + 2\,H_2O \qquad \Delta H_{298K} = -90 kJ/mol \tag{1.14}$$

$$CH_4 \rightleftharpoons C + 2\,H_2 \qquad \Delta H_{298K} = 75 kJ/mol \tag{1.15}$$

Nikoo et al. [40] analysed the thermodynamic equilibrium of this multi-reaction system, from which an Arrhenius plot of the equilibrium constant K as a function of the reaction temperature is given (figure 1.4). The equilibrium constant K is a function of the Gibbs free energy change of reaction as in equation (1.16).

$$K = e^{-\frac{\Delta G_r^0}{RT}} \tag{1.16}$$

Thermodynamic analyses of the DRM reaction extensively studied the optimal operating conditions for DRM [40, 41, 42, 43], concurring that significant CH_4 and CO_2 conversions with H_2/CO ratios approaching unity can be achieved at temperatures above 700°C and at atmospheric pressure (figure 1.5). These conditions favour the endothermic DRM reaction while minimising undesirable side reactions. Nonetheless, lower pressures are usually more beneficial, as reactants conversion is increased and carbon formation suppressed. Another route for carbon minimisation is operating with excess CO_2 in the feed gas to shift the equilibrium of carbon-forming reactions [44].

Many review articles have been written on the matter of catalyst choice for thermal DRM [46, 47, 48, 49]. The discussion revolves around balancing activity, selectivity, stability and cost-effectiveness. A fundamental issue that is also addressed is the resistance of the catalyst to coking and to the sintering of its active phase at high reaction temperatures. Both phenomena are the primary causes of catalyst deactivation.

For the choice of the active phase, noble metals such as Pt, Rh and Ru are reported to have a superior capacity to cleave the C-H bond, demonstrated excellent performances and resistance to carbon deposition [50, 51]. However, their high cost and limited availability have driven research towards more economical alternatives. Ni-based catalysts have emerged as the most promising non-noble metal option due to their relatively low cost and high activity. Nevertheless, Ni catalysts face challenges with deactivation due to

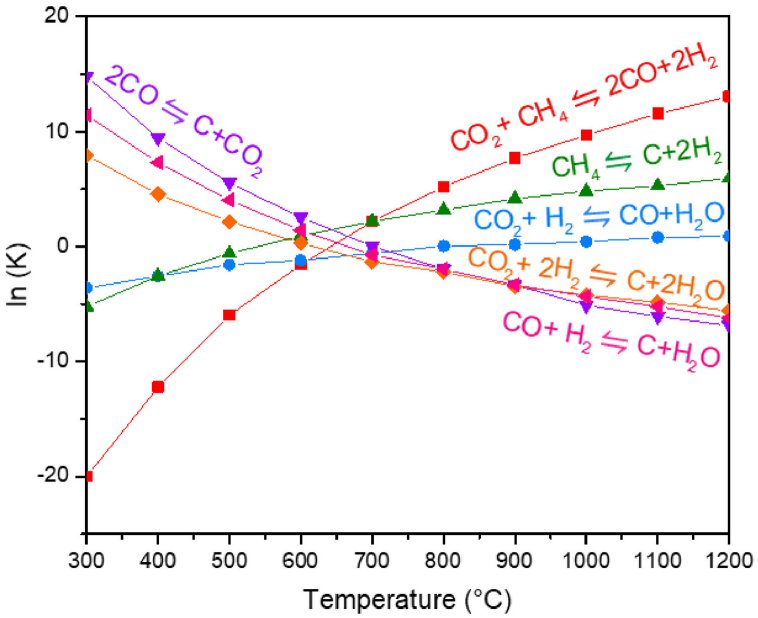

Figure 1.4. Arrhenius plot of the equilibrium constant K as a function of the reaction temperature for DRM and the concurrent reactions. (Source:[39], adapted from [40]).

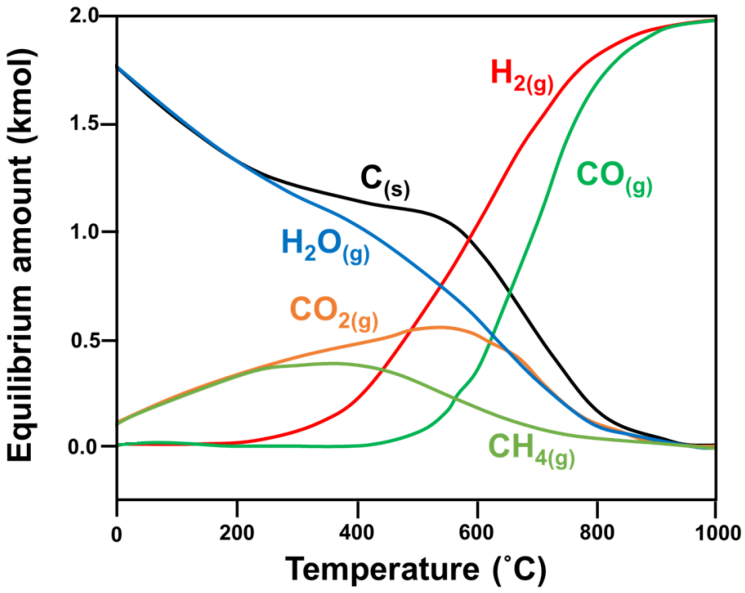

Figure 1.5. Thermodynamic equilibrium plot for DRM. (Source:[45]).

sintering and carbon formation at high temperatures. To address these issues, researchers have explored various strategies to enhance Ni catalyst stability [52].

One approach involves the careful selection of support materials. As Ni plays a key role in the dissociation of H_2 molecules, one of the criteria for choosing the catalyst support is its capacity to adsorb large amounts of CO_2 and to activate it. Another important criterion is the capacity of the support to disperse the active phase and have a strong metal-support interaction. While γ-Al_2O_3 remains the most popular support thanks to high surface area, high dispersion of Ni particles, high thermal stability and low cost, its acid-base properties are not ideal for CO_2 adsorption [49]. On this matter, it is worth mentioning the use of hydrotalcites and hydrotalcite-derived mixed oxides, which present both acidic and basic sites and were widely studied by Dębek et al. [1], where the importance of the preparation method is also underlined. Other oxides as MgO, SiO_2, CeO_2, Cao and La_2O_3 are also employed.

Another strategy to improve the Ni catalyst performance is the addition of promoters. Promoters such as Ce, La or alkali metals have proven to enhance catalyst basicity and oxygen mobility, thereby mitigating carbon deposition [53, 54].

Finally, recent studies have focused on advanced catalyst designs, including core-shell structures and single-atom catalysts. These approaches aim to maximise metal utilisation and stability by controlling particle size and metal-support interactions at the nanoscale [55, 56]. However, the scalability and long-term stability of these novel designs remain areas of ongoing research.

Despite significant advances, the development of a catalyst that combines high activity, long-term stability, and cost-effectiveness for industrial-scale DRM remains a challenge. This has led to growing interest in alternative approaches, such as plasma-catalysis, which may offer new pathways to overcome the limitations of traditional thermal catalysis.

Chapter 2

Plasma-Catalysis: A Synergistic Approach

2.1 Non Thermal Plasmas

Dissociation of molecules through electrical discharges is a well known process that is recently playing a central role in the development of power-to-fuel systems, in the framework of CCU. The attraction of these systems lies in the constitution of a sustainable cycle, where electricity coming from intermittent renewable sources can be stored in the form of chemical energy. The most efficient and mature dissociation process is water electrolysis, but plasma-chemical conversion is recently opening new fascinating routes for efficient molecular dissociation, especially in the field of CO_2 dissociation and green chemistry.

Plasmas, also referred to as the fourth state of matter, are partially or strongly ionised gases composed by a mixture of electrons, ions, neutral atoms and molecules [57]. When all these species are in thermodynamic equilibrium with each other, we refer to a *hot* or *thermal* plasma. Thermal plasmas are characterized by a relatively high ionization degree and high temperatures, typically >10^4 Kelvin.

Non-thermal plasmas (NTPs) are obtained by the application of an electromagnetic field to a neutral gas. They are characterised by a low ionization degree (10^{-4}-10^{-6}) [58] and by a strong thermodynamic non-equilibrium condition, that leads to the definition of different temperatures for the electrons (T_e) and the heavier particles (T_h). T_e is typically in the range of (10^4-10^5) K and it is much higher than the temperature of the heavy particles, which may be close to room temperature ($T_e >> T_h$). This feature is achieved by supplying electrical energy to the gas, which will be more likely employed to suddenly heat the electrons, thanks to their light mass. For this reason, cold plasmas are also known as *gas discharge plasmas*. The strong thermal disequilibrium between the different degrees of freedom of the species produces a highly reactive environment in which the collisions between electrons and neutral species results in the efficient production of reactive species, including ions, radicals, and excited molecules. These, in turn, can initiate and propagate chemical reactions that are otherwise thermodynamically unfavourable under ambient conditions. Thus, NTPs have emerged as a promising and highly efficient technology to promote chemical reactions under mild conditions.

The generation of non-thermal plasmas can be achieved through various discharge configurations [59]:

- Dielectric Barrier Discharge (DBD) plasmas exploit a dielectric material between electrodes to prevent arc formation and maintain non-equilibrium conditions. These systems operate at atmospheric pressure and are widely used for their simplicity, versatility and scalability properties.

- Gliding arc discharges (GA) employ a diverging electrode geometry where the plasma forms at the narrowest gap and extends along the electrode gap length. This configuration combines the advantages of both thermal and non-thermal plasmas.

- Microwave (MW) plasmas represent another significant category, where electromagnetic radiation at GHz frequencies couples directly with electrons. This coupling mechanism results in highly energetic electrons while maintaining relatively cool heavy species. The efficiency of energy transfer in these systems can reach remarkable values, particularly for molecular dissociation processes.

- The nanosecond repetitively pulsed (NRP) discharge has gained particular attention in recent years due to its unique properties and potential advantages for chemical processing.

2.1.1 Nanosecond Repetitively Pulsed Discharge Plasma

NRP discharges are characterised by the application of high-voltage pulses with rise time and duration in the nanosecond range, typically repeated at frequencies in the kHz range. This pulsed nature allows for the efficient production of high-energy electrons and reactive species, while maintaining a relatively low average gas temperature. The short pulse duration limits the development of thermalization processes that would increase the gas temperature, ensuring the plasma remains in a non-equilibrium state. Another advantage brought by the ns-duration pulsed pattern is that the power developed by the discharge is in the order of the MW, while the energy remains relatively low (mJ) [60].

One of the key advantages of NRP discharges is their ability to generate a very high plasma density, and so a high concentration of reactive species, with a relatively low power consumption. This is achieved through the short pulse durations, which prevent thermalization of the gas [61]. Unlike (sub)microsecond pulsed discharges that are initiated by Townsend discharges, NRP discharges ignite instantaneously and don't need the involvement of secondary electrons [59]. This results in a glow-like discharge mode, even under high electric field conditions, rather than the filamentary mode often observed in other types of discharges [62].

Compared to continuous wave discharges, a superior control is given over the electron energy distribution. In fact, it becomes possible to direct more energy toward selected dissociation channels by adjusting the pulse length, according to Iza et al. [63]. Another crucial parameter is the pulse repetition frequency. It has the effect of accumulating metastable species that are important to sustain the discharge, and it should be high enough to prevent recombination of the active species produced in the discharge [64]. The importance of the pulse sequence has been studied by Montesano et al. in relation to CO_2 dissociation [60, 65] and the DRM reaction [66].

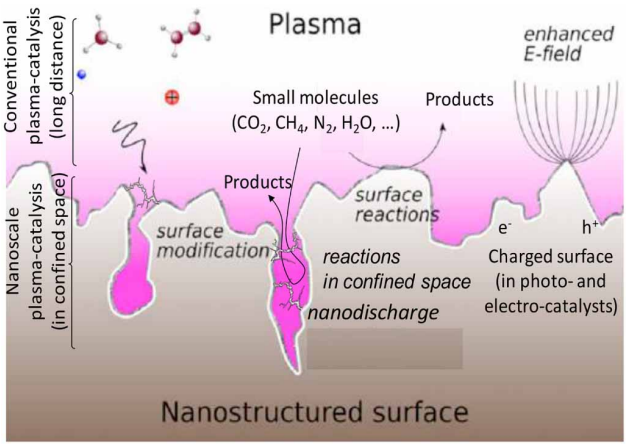

Figure 2.1. Examples of plasma-catalytic synergy effects. (Souce:[69])

2.2 Plasma-Catalysis

Plasma-catalysis is an emerging field that combines the advantages of non-thermal plasma activation with heterogeneous catalysis. This hybrid approach aims to achieve synergistic effects that can enhance reaction rates, selectivity, and energy efficiency beyond what is possible with either plasma or catalysis alone [67, 68]. The synergy arises from a combination of complex interactions between the plasma and the catalyst, which today are still not fully understood. Some examples are shown in figure 2.1. The plasma can modify catalyst properties by creating oxygen vacancies, altering oxidation states, or improving dispersion of active sites. Conversely, the catalyst can influence plasma characteristics, enhancing electric field strength and altering discharge behaviour. These mutual effects can lower activation barriers or increase the lifetime of reactive species. The combination of plasma-generated species and catalytic sites can also enable reaction routes that are not accessible in standard thermal catalysis.

The non-equilibrium nature of plasma can activate reactant molecules through various pathways not accessible in conventional thermal catalysis, while the presence of a catalyst can enhance selectivity and efficiency [68, 59]. However, the successful implementation of plasma-catalytic systems heavily depends on the coupling configuration between the plasma and catalyst.

The successful implementation of plasma-catalytic systems presents significant engineering challenges due to the complex interplay of multiple phenomena occurring simultaneously. When plasma and catalyst are combined, various processes take place across different length- and time-scales: plasma-phase chemistry, surface reactions, heat and mass transfer, and modifications of both the plasma discharge characteristics and the catalyst properties [70, 67]. The presence of the catalyst can alter the plasma discharge mode and electric field distribution, while plasma exposure can dynamically modify catalyst properties such as oxidation state, surface chemistry, and morphology. These mutual interactions make it particularly challenging to identify universal design principles for plasma-catalytic systems. Furthermore, traditional catalytic parameters and metrics considered fundamental in thermal catalysis - such as intrinsic reaction rates and active site density - lose their conventional meaning in plasma-catalysis, as these properties become dynamically modified under plasma exposure [71]. Understanding and controlling these interactions becomes crucial for developing effective plasma-catalytic processes.

2.3 Plasma-catalysis for CO_2 recycling

Plasma catalysis for CO_2 recycling has become a hot topic within the last decade, as evidenced by the increasing number of peer reviewed publications in this field [71, 59, 69, 72].

2.3.1 CO_2 conversion

On the matter of CO_2 dissociation with plasma much progress has already been made in the comprehension of the mechanisms at play. CO_2 dissociation in plasma happens mainly through three routes: direct electron impact, electron impact on vibrationally excited levels, or the so-called vibrational ladder climbing (figure 2.2), which is the most energy efficient channel [57]. While in NRP discharges there is strong excitation of the molecular vibrational states, there is debate on whether this path is the dominant one [73]. Martini and coworkers [74] performed a study on the time evolution of CO_2 dissociation in a NRP discharge event focusing on its dissociation kinetics. The kinetics of the process was investigated through a time-resolved Laser Induced Fluorescence (LIF) diagnostics, operated in Collisional Energy Transfer (CET-LIF) mode. The authors found that the CO_2 dissociation degree measured 5 µs after the breakdown was more than three times larger than the one measured in the effluent gas at the exit of the reactor, i.e. about 100 µs later. In addition, a temperature of 2500 K is reported in the immediate post-pulse, that decreases to about 1500 K when the second measure is performed. These results highlight the need to find a way to fixate the high dissociation rate reached by the plasma in the first microseconds, before recombination can happen. To our knowledge, there is no report of plasma-catalytic CO_2 splitting with a NRP discharge.

If we extend the domain to consider CO_2 conversion in all possible plasma-catalytic reactions, we are able to gather a picture of which catalyst combinations were studied the most. Being DBD the most used reactor type for plasma-catalysis, a discrete body of data already exists on plasma-catalytic performances with this plasma source. Therefore, a first idea of the catalyst performance in this specific context can be given. In figure 2.3 we show a plot extracted from [71] referred to DBD published data where the distribution of CO_2 conversion rate and energy efficiency of CO_2 conversion are reported for different catalytic support materials. The top half distribution (in blue) refers to the effect of the support material alone, while the bottom half represents the combined effect of the support with an active phase. In this case, CeO_2-supported catalysts are the ones that register highest efficiency and high CO_2 conversions. Al_2O_3-based catalysts perform similarly with or without an active phase, and their conversion mean is close to 20%. Zeolites and SiO_2-supported extend through a large range of possible CO_2 conversions, reaching maximum efficiencies of 20%.

2.3.2 DRM

When methane is added to the equation and the DRM reaction is conducted in plasma, the reaction dynamics and mechanisms become much more articulated. Compared to the thermal reaction, the non-equilibrium nature of plasma introduces new reaction pathways and alters the kinetics of existing ones. CO_2 and CH_4 can be directly activated by electron impact, which plays a crucial role in initiating the reforming process [76]. The formation of reactive species such as CO_2^+, CH_3, and H radicals opens the possibility to produce not only syngas, but also hydrocarbons such as acetylene (C_2H_2), ethylene (C_2H_4) and ethane (C_2H_6) and

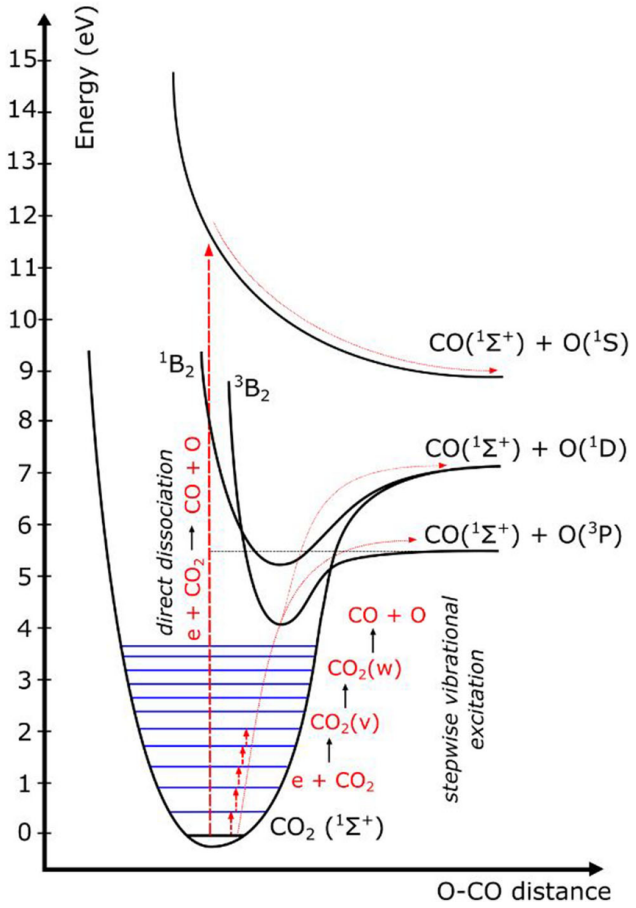

Figure 2.2. Vibrational ladder climbing mechanism for CO_2 dissociation. Source:[75]

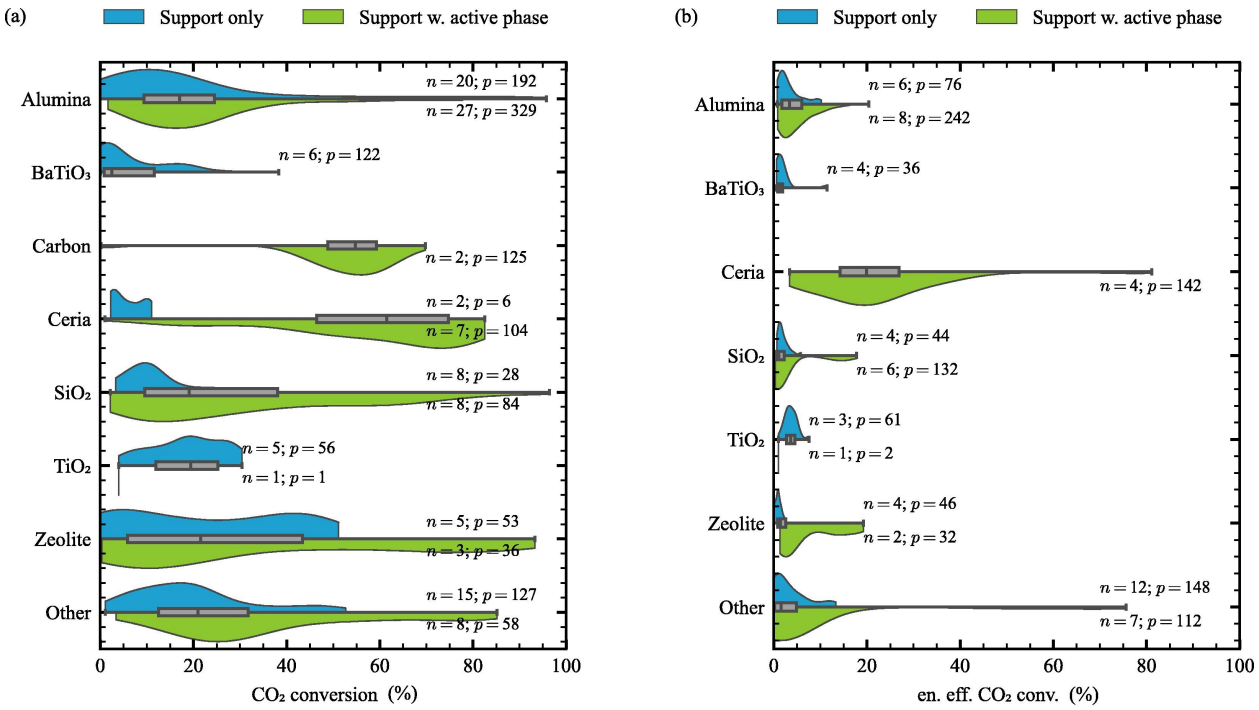

Figure 2.3. Comparison of CO_2 conversion (a) and energy efficiency of CO_2 conversion (b) reported for DBD plasma-catalytic setups for different supports. Top half (blue) represents supports and bottom half (green) the effect of support with an active phase. Box plots show quartiles of the total group per support category, with individual kernel density estimates per scenario indicating the distribution of data for each scenario (using a bandwidth factor of 0.4 to highlight multi-modality in the data). Annotations show the number of publications (denoted by n), and individual data points (denoted by p) that comprise the distributions. Source:[71].

alcohols like methanol (CH_3OH). The thermodynamic constraints of thermal DRM such as the limit of H2/CO ratio, typically close to 1, are also overcome in the plasma reaction. Here, the coupling with a catalyst becomes also a tool to direct the selectivity towards desired products and tune the syngas ratio.

2.4 State of the art in the plasma-catalytic DRM

In this section we aim to analyse more closely some plasma-catalytic coupling aspects in the DRM reaction, drawing insights from a comprehensive analysis of recent literature and including data extracted from the PIONEER database on plasma-catalytic CO_2 conversion (PDB) [71]. The total number of individual experimental publications examined is 42, from which 214 unique combinations of *plasma* + *catalyst* + *experimental conditions* can be extracted. The metrics that we present in the following sections are calculated on the frequency of these unique configurations, and not on the number of (x,y) performance tuples measured for each condition.

The analysis focuses on key operational and design parameters that are consistently reported across studies and have demonstrated significant impact on DRM performance. Plasma source types, plasma-catalytic coupling configurations and catalyst composition (active phase, support material, promoters) are discussed, together with their influence on performance metrics as CO_2 and CH_4 conversion as a function of the specific energy input (SEI). Parameters with insufficient coverage or inconsistent reporting methods across studies were excluded to ensure statistical relevance. This selective approach allowed to draw general conclusions while acknowledging the limitations of considering the complete picture.

Table 2.1. Overview of plasma-catalytic studies for dry reforming of methane. Data extracted from the PIONEER DataBase (PDB) of plasma-catalysis for CO_2 recycling [71].

No	Composition	Coupling type	Source type	Gases	Gas ratio (%)	SEI (J/L)	Author year	Ref.
1	$NiO-/Al_2O_3$	other	GDA	CO_2/CH_4	50/50	3600	Allah2015	[77]
2	Ni-/	other	GDA	CO_2/CH_4	50/50	3600	Allah2015	[77]
3	$NiO-/Al_2O_3$	other	GDA	CO_2/CH_4	50/50	2850	Allah2015	[77]
4	$Ni-/Al_2O_3$	PB	corona	CO_2/CH_4 /Ar	26.7/13.3 /60	2400	Aziznia2012	[78]
5	$-/Al_2O_3$	PB	corona	CO_2/CH_4 /Ar	26.7/13.3 /60	2400	Aziznia2012	[78]
6	$-/Al_2O_3$	FB	DBD	CO_2/CH_4 /He	17/8 /75	6000	Bouchoul2021	[79]
7	$Ni-La_2O_3/Al_2O_3$	PB	DBD	CO_2/CH_4 /Ar	37.5/37.5 /25	3360-17040	Diao2023	[80]
8	$Ni-/Al_2O_3$	PB	DBD	CO_2/CH_4 /Ar	37.5/37.5 /25	3900-9960	Diao2023	[80]
9	$Ni-La_2O_3/Al_2O_3$	PB	DBD	CO_2/CH_4 /Ar	37.5/37.5 /25	4980-13260	Diao2023	[80]
10	-/Ni	PB	NRP	CO_2/CH_4	50/50	40000	Dou2022	[81]
11	Co-Al/Ni	PB	NRP	CO_2/CH_4	50/50	40000	Dou2022	[81]

Continued on next page

Table 2.1 continued from previous page

No	Composition	Coupling type	Source type	Gases	Gas ratio (%)	SEI (J/L)	Author year	Ref.
12	CoMg-Al/Ni	PB	NRP	CO_2/CH_4	50/50	40000	Dou2022	[81]
13	NiMg-Al/Ni	PB	NRP	CO_2/CH_4	50/50	40000	Dou2022	[81]
14	-/zeolite NaX	other	DBD	CO_2/CH_4	50/50	80000-280000	Eliasson2000	[82]
15	-/SiO_2	PB	DBD	CO_2/CH_4	50/50	0-48000	Gallon2011	[83]
16	-/Al_2O_3	PB	DBD	CO_2/CH_4	50/50	0-48000	Gallon2011	[83]
17	-/zeolite 3A	PB	DBD	CO_2/CH_4	50/50	0-48000	Gallon2011	[83]
18	Ni-/La_2O_3 + MgAl2O4	PB	DBD	CO_2/CH_4	50/50	NaN	Khoja2020	[84]
19	Pd-/Al_2O_3	FB	RF	CO_2/CH_4 /He	2/3 /95	NaN	Kroker2012	[85]
20	Cu-/Al_2O_3	FB	RF	CO_2/CH_4 /He	2/3 /95	NaN	Kroker2012	[85]
21	Ni-/Al_2O_3	PB	corona	CO_2/CH_4	66.7/33.3	18000-42000	Li2006	[86]
22	-/zeolite HZSM5	PB	corona	CO_2/CH_4	66.7/33.3	18000-42000	Li2006	[86]
23	Ni-/BN	PB	DBD	CO_2/CH_4 /Ar	33.33/33.33 /33.33	NaN	Li2023	[87]
24	-/Al_2O_3	PB	other	CO_2/CH_4 /N_2	30/20/50	2773	Long2008	[88]
25	Ni-/Al_2O_3	PB	other	CO_2/CH_4 /N_2	30/20/50	2773	Long2008	[88]
26	Cu-/Al_2O_3	PB	RF	CO_2/CH_4 /H_2O/Ar	28.5/14.5 /28.5/28.5	NaN	Nguyen2022	[89]
27	-/ $BaFe_{0.5}Nb_{0.5}O_3$	PB	DBD	CO_2/CH_4	50/50	NaN	Pan2014	[90]
28	La_2O_3-/Al_2O_3	PB	DBD	CO_2/CH_4 /He	1.2/16.8 /82	33750-39750	Pham2011	[91]
29	-/glass	PB	DBD	CO_2/CH_4	50/50	1500-4875	Ray2017	[92]
30	Ni-Mn/Al_2O_3	PB	DBD	CO_2/CH_4	50/50	600-4200	Ray2018	[93]
31	Ni-/Al_2O_3	PB	DBD	CO_2/CH_4	50/50	1400-4400	Ray2018	[93]
32	-/Al_2O_3	PB	DBD	CO_2/CH_4	50/50	260000	Song2004	[94]
33	Ni-/Al_2O_3	PB	DBD	CO_2/CH_4	50/50	260000	Song2004	[94]
34	Ni-/Al_2O_3	PB	DBD	CO_2/CH_4	50/50	84000-120000	Tu2011	[95]
35	Ni-/Al_2O_3	PB	DBD	CO_2/CH_4	50/50	60000	Tu2012	[96]
36	-/SiO_2	PB	DBD	CO_2/CH_4	50/50	60000	Tu2012	[96]
37	Ni-/Al_2O_3	PB	DBD	CO_2/CH_4	50/50	60000	Tu2012	[96]
38	Ni-/Al_2O_3	PB	DBD	CO_2/CH_4 /Ar	8.15/8.15 /83.7	NaN	Wang2009	[97]
39	-/Al_2O_3	PB	DBD	CO_2/CH_4	50/50	15000	Wang2017	[98]
40	Ni-/C	PB	DBD	CO_2/CH_4	50/50	54000	Wang2019	[99]
41	Ni-CeO_2/C	PB	DBD	CO_2/CH_4	50/50	48000	Wang2020	[100]
42	Ni-/Al_2O_3	PB	DBD	CO_2/CH_4	50/50	9000	Zeng2015	[101]

Continued on next page

Table 2.1 continued from previous page

No	Composition	Coupling type	Source type	Gases	Gas ratio (%)	SEI (J/L)	Author year	Ref.
43	Co-/Al_2O_3	PB	DBD	CO_2/CH_4	50/50	9000	Zeng2015	[101]
44	Cu-/Al_2O_3	PB	DBD	CO_2/CH_4	50/50	9000	Zeng2015	[101]
45	Mn-/Al_2O_3	PB	DBD	CO_2/CH_4	50/50	9000	Zeng2015	[101]
46	Ni/Al_2O_3	PB	DBD	CO_2/CH_4	50/50	72000-240000	Zheng2015	[102]
47	$LaNiO_3$-/Al_2O_3	PB	DBD	CO_2/CH_4	50/50	72000-240000	Zheng2015	[102]
48	Ni-/La_2O_3	PB	DBD	CO_2/CH_4	50/50	72000-240000	Zheng2015	[102]
49	$LaNiO_3$-/	PB	DBD	CO_2/CH_4	50/50	72000-240000	Zheng2015	[102]

Table 2.1 provides a comprehensive overview of plasma-catalytic studies for the DRM reaction from the literature. We chose here to report the catalyst composition (scheme is: Active Phase-Promoter/Support), coupling type (PB=Packed Bed, FB= Fluidised Bed), plasma source type, gas feed composition and SEI range.

2.4.1 Plasma-catalytic coupling

The design of plasma-catalytic reactors for DRM requires careful consideration of both the plasma generation method and the catalyst integration strategy. The analysis of the current state of the art reveals clear patterns in reactor configurations and their impact on performance.

In-Plasma vs Post-Plasma Catalysis

The integration of plasma and catalysis can be categorized into two approaches [103]:

1. *in-plasma catalysis* (IPC), where the catalyst is placed directly in the discharge zone, and
2. *post-plasma catalysis* (PPC), where it is placed downstream of the plasma region.

The different spatial arrangement not only influences the physical interaction between plasma species and catalyst surface, but also determines the dominant mechanisms of plasma-catalyst synergy [59].

In the IPC, also known as single-stage configuration, a direct contact enables complex synergistic effects that can modify the physical and chemical properties of the system. Both short-lived and long-lived plasma species reach the catalyst surface to participate in surface reactions and the plasma can modify catalyst properties through mechanisms such as surface charging, localized heating and the creation of active sites. The catalyst can in turn influence plasma characteristics by altering the electric field distribution, the discharge type, and providing surfaces for discharge formation. Chung et al. [103] reported an increase in the surface area and decrease in the grain size of a ferroelectric catalyst post reaction, attributed to electron bombardment during the discharge. In addition, XPS peak shifts were observed, associated with surface charge accumulation.

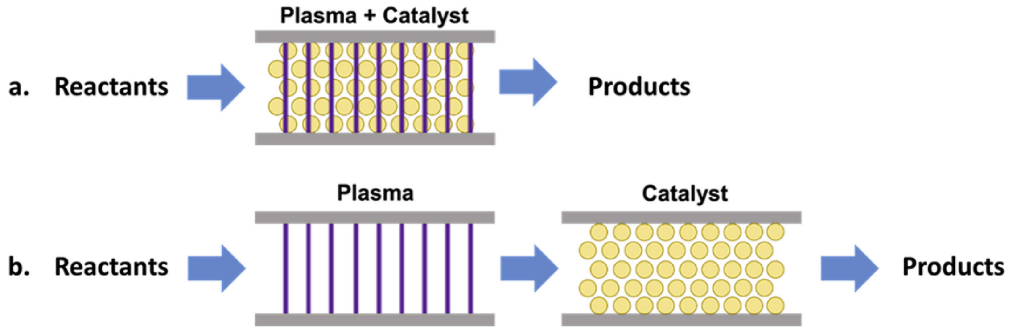

Figure 2.4. Simplified schematic of the two possible coupling configurations between a plasma and a catalyst. a) in-plasma catalysis (IPC): The catalyst is inserted in the plasma discharge zone and the two are in direct contact with one another. b) Post-plasma Catalysis (PPC): the catalyst is put downstream of the discharge zone. The two have an indirect interaction. (Source: [72]).

The PPC, or two-stage configuration, positions the catalyst downstream of the plasma discharge. In this arrangement, only stable or long-lived plasma-generated species interact with the catalyst surface. While this configuration may sacrifice many of the direct plasma-catalyst synergies, it allows external control over catalyst temperature and can protect susceptible catalyst materials from degenerative plasma exposure. A step further was taken by Xu et al. [104], who developed a post-plasma catalytic bed for a gliding arc plasmatron (GAP) that showed an excellent performance in the DRM reaction, without the use of external insulation or heating. The system was tested with a Ni-based mixed oxide catalyst and showed reactant conversions and syngas selectivities comparable with the thermal catalytic reaction at 800 °C, but with a reduced energy cost of 4.3 kJ/L.

The IPC is by far the most diffuse configuration, due to its potential for stronger plasma-catalyst interactions and the practical convenience of implementation, particularly in DBD reactors. This is mirrored in the studies examined, where PPC is only employed in approx. 9% of the selected studies, mostly when the discharge prevents direct contact with the materials. This is the case for gliding arc (GDA) discharges [67, 71] and cold plasma jets [105], where the catalyst is placed in early post-discharge position. A temperature-controlled catalytic reactor in series with a spark discharge is reported by Li et al. [106], whereas Song et al. use a single DBD reactor, where the catalyst is placed at the bottom of the discharge zone [94].

Packed Bed, Fluidized Bed, Monolithic Coupling

Another classification worth considering is how the catalyst is included in the plasma-catalytic system. Three main reactor configurations emerge from the DRM literature: packed bed (PB), fluidized bed (FB), and monolithic (M) arrangements. Fig. 2.5 shows the normalized frequencies of the configurations reported in the examined literature for the DRM reaction, where the type of plasma source used is also represented.

Packed bed (PB) is the dominant coupling strategy, accounting for over 80% of reported systems. In this configuration, catalyst particles or pellets are fixed within the discharge zone, either filling the gap between electrodes in DBD systems or surrounding the discharge in other plasma sources. The presence of catalyst particles significantly influences electric field distribution through enhanced fields at particle contact points due to dielectric polarization. The way a packed bed reactor is packed significantly impacts the type of

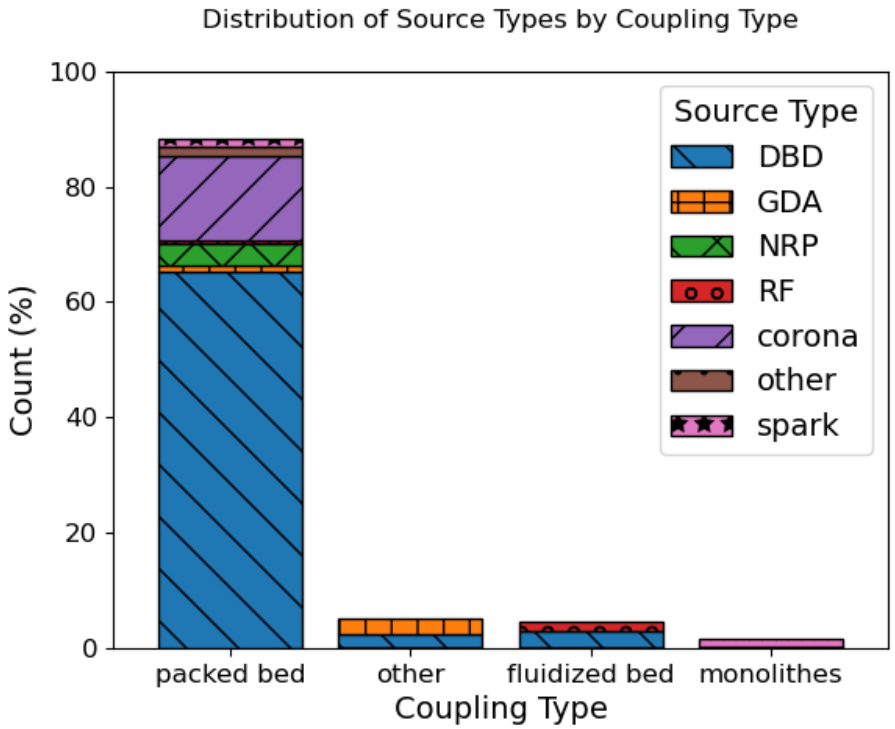

Figure 2.5. Distribution of plasma source types for distinct plasma-catalytic coupling configurations. For each entry, unique combinations of *catalyst* + *plasma* + *experimental conditions* have been considered, so the same paper can contribute to multiple entries. Abbreviations are: Dielectric Barrier Discharge (DBD), Gliding Arc (GDA), Nanosecond Repetitively Pulsed (NRP), Radio Frequency (RF).

discharge it produces, and this in turn affects the efficiency of the dry reforming process. Fully packing the catalyst can suppress the formation of microdischarges, leading to lower conversions of CH_4 and CO_2 [107, 108]. Partially packing the catalysts, either radially or axially, can retain a strong filamentary discharge, which enhances the interaction between the plasma and the catalyst [109]. In addition, the introduction of a catalyst can change the characteristics of the microdischarges, leading to longer lifetimes and higher discharge currents, which may improve the activation of reactive species [107, 110].

Fluidized bed reactors (FB), representing approximately 8% of studied systems, create a dynamic mixing environment that enhances mass and heat transfer while providing better temperature control. This configuration proves particularly effective in preventing hot spot formation and maintaining catalyst activity. Kroker et al. [85] demonstrated these advantages in an RF plasma system, achieving stable operation at temperatures above 700°C with improved catalyst utilization and more uniform temperature distribution. Their work highlighted the potential of fluidized systems for large-scale applications where thermal management becomes critical. Chen and co-workers [111] compared the DRM performance of a fluidized bed and a packed bed DBD reactor. The superior reaction performance shown by the FB-DBD reactor was attributed to an enhanced coupling between the fluidized catalyst particles and the plasma-generated vibrationally-excited species.

Monolithic arrangements, also comprising about 8% of studies, employ structured catalyst supports such as foams or honeycomb structures. Jurkovic et al. [112] demonstrated their advantages using Al_2O_3 foam catalysts in a spark discharge system, achieving improved mass transfer while maintaining plasma stability. The key benefit of monolithic systems lies in their ability to provide lower pressure drop and more uniform flow patterns compared to packed beds, making them particularly suitable for high-throughput applications.

Each configuration presents distinct trade-offs between plasma-catalyst contact efficiency, mass/heat transfer, and operational complexity. While packed beds offer excellent plasma-catalyst contact area and good conversion rates at moderate temperatures, they remain limited by pressure drop and mass transfer constraints [92, 110]. Fluidized beds excel in temperature control and mass transfer but require more complex operation and higher gas flow rates to overcome the weight of the particles and produce their fluidization [111, 113]. Monolithic systems provide operational advantages through lower pressure drops and more uniform flow distribution, though potentially at the cost of reduced specific surface area. The predominance of packed bed configurations in current research stems largely from their simplicity and well-understood behavior. However, their inherent limitations suggest that alternative configurations merit further investigation, particularly for industrial-scale applications where pressure drop and heat management become critical factors [99, 114]. Future research directions should focus on quantifying these relationships across different plasma sources, catalyst composition and operating conditions.

2.4.2 Catalyst composition

The choice of catalyst materials in plasma-catalytic DRM reflects both traditional thermal catalysis and plasma-specific considerations. For this reason, analysing possible patterns and correlations between specific catalyst compositions and specific plasma sources is an interesting path to follow. However, as already evidenced in Fig. 2.5, an analysis of the available literature on plasma-catalytic DRM reveals that there still

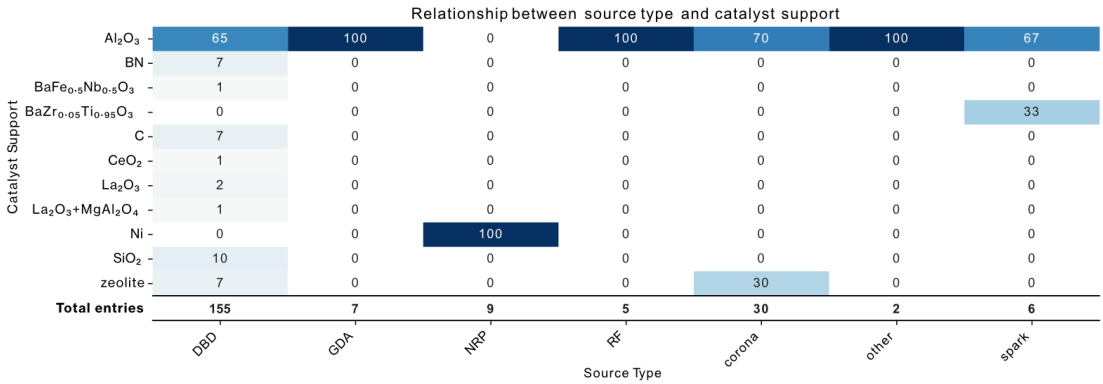

Figure 2.6. Heatmap comparing the most used catalytic supports with different plasma source types, in DRM plasma-catalysis.

is a significant imbalance between studies that employ DBD discharges and the ones with other plasma sources. The number of analysed configurations with the former is close to 180, while other plasma sources like corona, spark, gliding arc, radio frequency and nanosecond pulsed discharges are represented by only a handful of configurations each. This substantial disparity in available data makes it statistically challenging to draw meaningful correlations between catalyst compositions and plasma source types outside of DBD systems. Nevertheless, some valuable observations can be drawn and the gaps of research can be highlighted.

Support Material

As shown in Fig. 2.6, alumina (Al_2O_3) emerges as the predominant support material across all plasma sources except nanosecond repetitively pulsed discharges (NRP), and being the only support reported for gliding arc (GDA) [77], radiofrequency (RF) [85] and specific applications, like plasma jet [105]. This prevalence can be attributed to several factors, like its high surface area and thermal stability, its favourable dielectric properties for plasma formation, a well-understood surface chemistry and preparation methods, and its cost-effectiveness and commercial availability. For NRP discharges the only data reported come from the work of Dou et al. [81], where the discharge is a DBD atmospheric-pressure plasma in a nanosecond repetitively pulsed regime. The source categorization gave priority to the plasma regime, that characterizes better its properties and its behaviour. Here, the catalysts coupled are nickel foam-supported cobalt-based catalysts.

Zeolites represent the second most common support class in corona plasma applications [106, 94]. Their unique pore structure and tuneable acidity offer advantages for product selectivity control. However, their use is limited to low-temperature plasma sources (like corona or DBD), due to thermal stability concerns.

Finally, DBD sources present a uniform variety of supports studied, ranging from zeolites, to activate carbon, silica or more elaborated formulations. The versatility of DBD discharges and the ease of catalytic coupling are an advantage for systematic studies on catalyst composition: catalysts can be directly accommodated in the discharge gap [115] and the plasma can be operated at atmospheric pressure with a simple design that is suitable for upscaling [101].

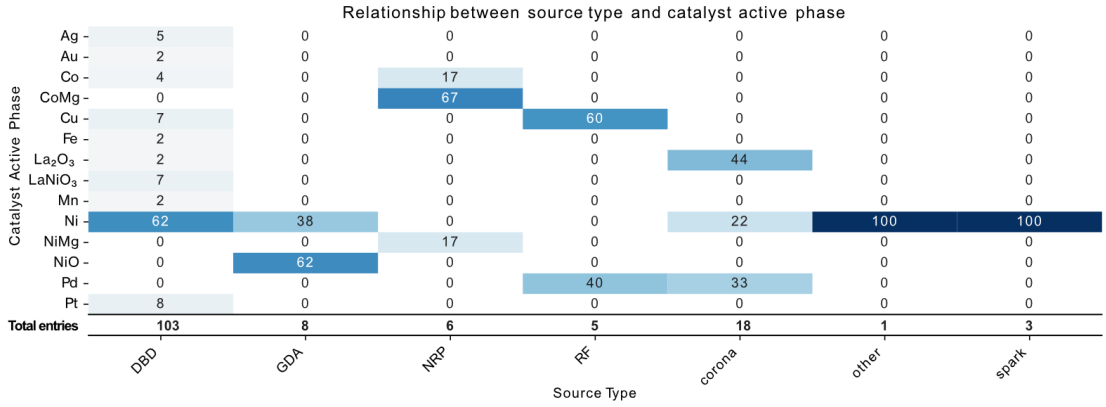

Figure 2.7. Heatmap comparing the most used catalytic active phases with different plasma source types, in DRM plasma-catalysis.

Active Phase

Active phases distribution compared to plasma sources is shown in Fig. 2.7. Nickel is the most commonly used active phase in plasma-catalytic DRM, appearing in 62% of the DBD studies. This preference stems from its availability, cost-effectiveness and demonstrated good activity both in thermal- and in plasma-catalytic applications [112]. However, Ni catalysts are prone to fast deactivation, due to sintering and coking [92]. In the case of GDA sources in PDB, both Ni and NiO oxide [77] have been tested.

Besides Ni, other supported metal catalysts include copper, cobalt and manganese. Cu exhibits good selectivity towards syngas and shows a high carbon balance in DRM [101]. Co has been tested by Dou et al. also in a bi-metallic CoMg catalyst [81], while Mn showed good conversion of reactants in comparison to the others in a DBD [109].

Noble metals like Pt, Pd, Ag and Au appear in γ-Al_2O_3-supported catalysts [107], [111, 112, 92] mainly in specialized DBD applications, particularly where enhanced stability or specific product selectivity is required.

Promoter

Fig. 2.8 shows the distribution of promoters alongside the number of configurations where they were reported in PDB for each plasma source. As evidenced, the presence of promoters in catalyst compositions for plasma-catalytic DRM is still underrepresented. Only in DBD applications, the fraction of catalysts with a promoter is about 20-25% of the total. In general, most of the applications associate a promoter with a Ni-based catalyst, while some with noble metals [116, 117].

The most used promoters are lanthanum compounds (La, La2O3). They are reported to enhance Ni dispersion, improve CO_2 activation through $La_2O_2CO_3$ intermediate formation and enhance discharge properties increasing surface discharge [80]. Ultimately these properties result in improved coke resistance of the catalyst. Another popular promoter is ceria (CeO_2), which can increase CO_2 adsorption and activation, and enhance Ni nanoparticles reducibility [100].

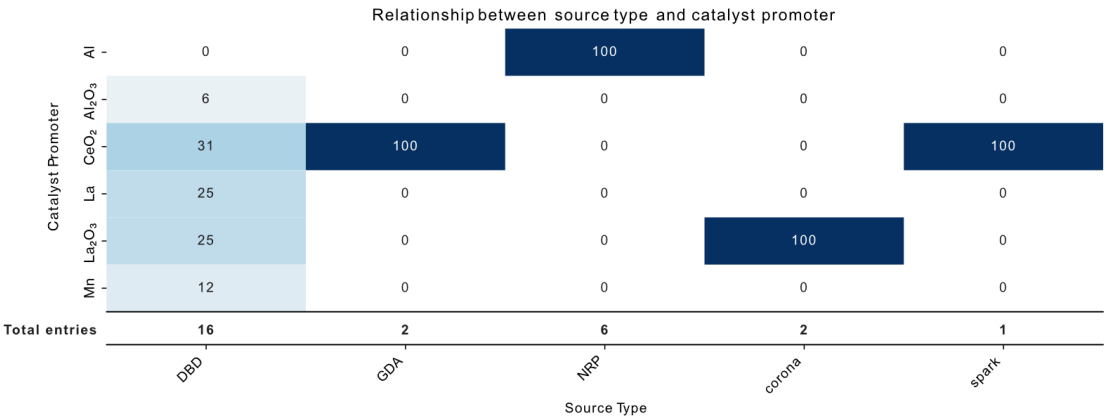

Figure 2.8. Heatmap comparing the most used catalytic promoters with different plasma source types, in DRM plasma-catalysis.

This distribution suggests that promoter selection is driven by both traditional catalyst stability considerations and plasma-specific requirements for enhanced electron mobility and oxygen storage capacity.

2.4.3 DRM performance comparison

We here show how the discussed configurations can impact the plasma-catalytic performance. For performance parameters we chose CO_2 and CH_4 conversion. We define the rate of conversion χ of reactant i (i = CO_2, CH_4) as the ratio between converted and provided moles (equation (2.1)). The conversions are reported in relation to the specific energy input (SEI), defined in J/L units as in equation (2.2).

$$\chi_i(\%) = \frac{n_i^{conv}}{n_i^{prov}} \tag{2.1}$$

$$SEI[J/L] = \frac{P[W]}{\phi[sccm]} \cdot 10^3\,[mL\,L^{-1}] \cdot 60\,[s\,min^{-1}] \tag{2.2}$$

Fig. 2.9 reports the measured CO_2 and CH_4 conversion rates as a function of SEI, coloured by plasma source type. As expected, there is a positive correlation between CO_2 and CH_4 conversion and SEI, as higher energy inputs imply higher dissociation rates. This relationship might not be linear, as the data are plotted in a semi-logarithmic scale. There is a predominance of data on DBD setups (blue), which are distributed across the whole SEI range. In general, lower SEIs correlate with lower conversions, and the maximum registered CO_2 conversion of about 82% is reached at a SEI less than 4 × 105 J/L in a packed bed DBD with a Ni/La_2O_3 + $MgAl_2O_4$ catalyst [84]. However, while higher SEI values may lead to increased conversion, they may not necessarily result in better energy efficiency.

Fig. 2.10 reports DRM reactants conversions, highlighting the role of the catalyst composition. The colour of the datapoints is indicative of the active phase, while the marker shape is related to the catalyst support composition. As it is visible from the blue datapoints, in some cases the role of the support alone was tested, to assess its individual influence. However, the supports performance data available in the database lack a counterpart with active phase, carried out under the same conditions.

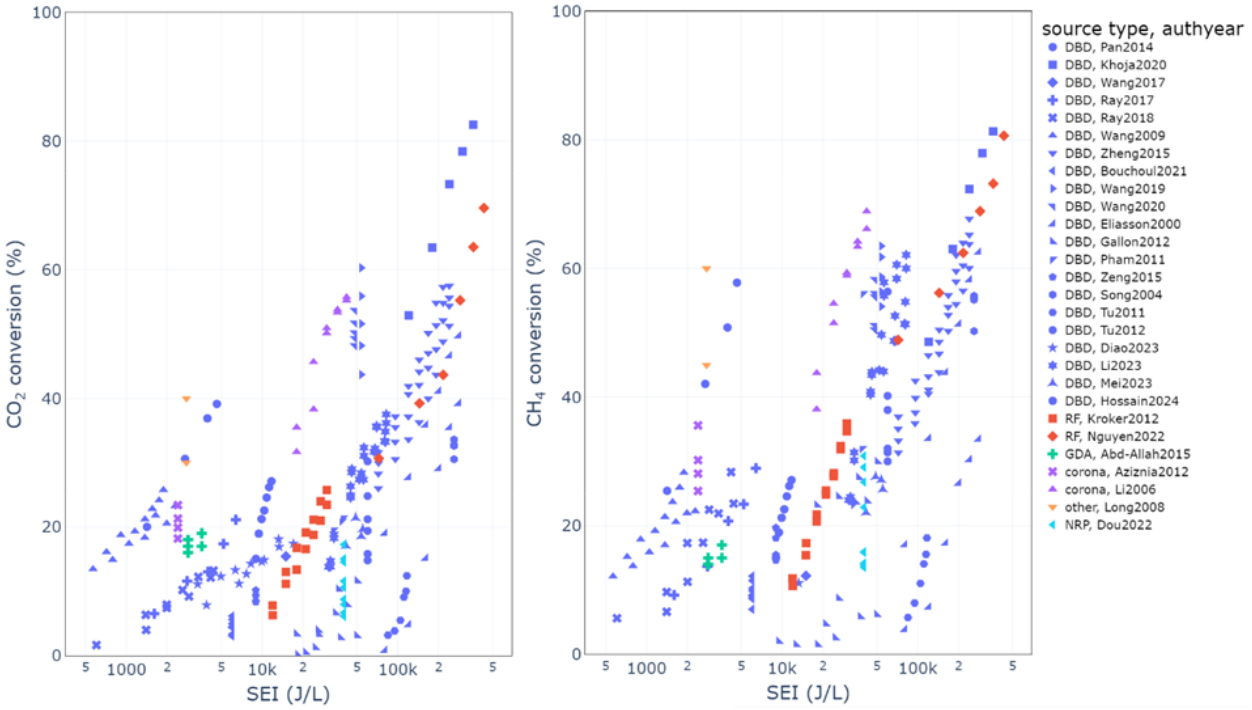

Figure 2.9. CO_2 and CH_4 conversion rates (%) reported as a function of the selective energy input (SEI, in J/L units). The colour of the markers refers to the plasma source used, while the shape identifies the publication by the tuple [author, year of publication]. The data are extracted from the smaller poll of publications that reported this measurement

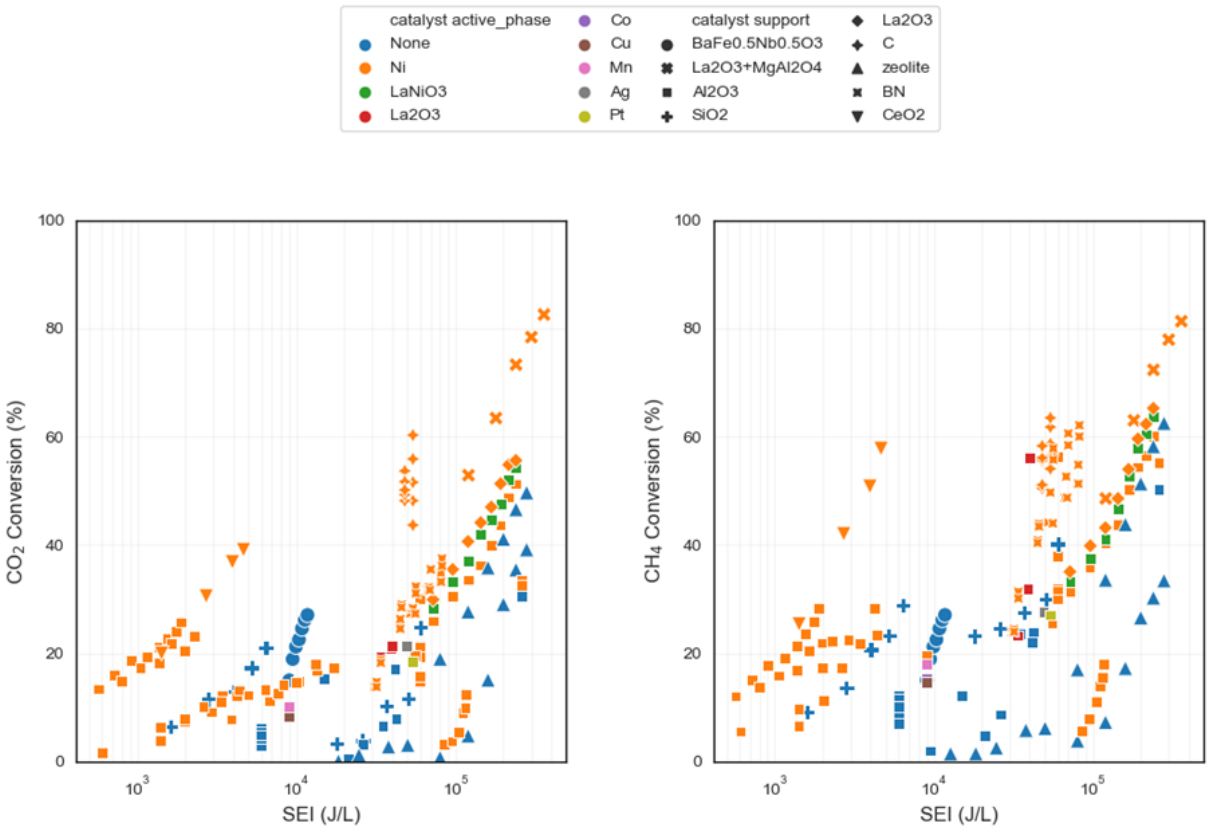

Figure 2.10. CO_2 and CH_4 conversion rates (%) reported as a function of the selective energy input (SEI, in J/L units). The colour of the markers refers to the active phase of the catalyst, while the shape identifies the catalyst support.

From this comparison, we observe that in general the catalysts perform similarly both for CO_2 and for CH_4 conversion.

Chapter 3

This PhD Thesis

3.1 The Framework

The excitement in the recent years around plasma-catalysis as a promising technology for GHG mitigation and carbon utilisation has also led to the blossoming of new, international and inter-disciplinary collaborations among the academia and other research institutions, meant to join forces and tackle the issue with diversified, but complimentary approaches. It is from one of these collaborations that the European Union's MSCA-ITN programme "PIONEER - Plasma catalysis for CO_2 recycling" was born, of which this thesis is a part of. The project has been conducted under a co-tutelle agreement between the Catalytic and Adsorption Processes in Energy and Environmental Protection group at the AGH University of Krakow, Department of Fuel Technology, under the supervision of Prof. Monika Motak, and the Atomic and Molecular Physics group at the University of Trento, Department of Physics, under the supervision of Prof. Paolo Tosi.

This work focused on the plasma-catalytic dry reforming of methane reaction (DRM) in a Nanosecond Repetitively Pulsed (NRP) discharge. The point of view from which this topic was explored was understanding how to achieve the plasma-catalytic synergy in a post-plasma catalysis configuration, by integrating heterogeneous catalysts in the NRP reactor.

3.2 Motivation of this Thesis

Nanosecond Repetitively Pulsed discharges, as was described along the introduction chapter 1, are a promising and efficient plasma source to promote chemical reactions, but have not been properly explored yet. This gap in the research may be explained in part by the technological requirements that are needed to implement a discharge with nanosecond-scale pulses duration and to accurately measure its signal, compared to a dielectric barrier discharge (DBD) system, which can be easily assembled in a laboratory and that requires an oscilloscope to be characterised. Another reason relevant to the plasma-catalysis community is the difficulty in integrating a catalyst with such discharge. The concentrated energy and high temperatures reached in the electron stream do not allow a direct interaction with a catalyst material, so a post-plasma catalysis configuration must be researched, forgoing some of the benefits of the plasma-catalytic synergy. Nevertheless, the energy efficiencies and the energy costs reached by this plasma source are unparalleled compared

with standard DBD implementations. Snoeckx and Bogaerts [59] reported NRP performances in the DBD reaction from the literature to be on the efficiency target for syngas production of 60%, corresponding to energy costs of 4.27 eV per converted molecule.

The NRP used in this study is a pin-to-pin discharge that has been previously characterised in the plasma-driven CO_2 dissociation reaction by the works of Martini [118], Ceppelli [119] and Montesano [65, 60], and in the plasma DRM reaction by Montesano [66].

As for the choice of the catalysts, after a thorough literature review, we decided to couple Ni-based catalysts and to choose as supports mixed Mg-Al oxides and Al_2O_3. Hydrotalcite-derived Mg-Al mixed oxides were extensively studied in the catalytic DRM reaction by the work of Dębek [1, 53, 44], and have been chosen because of their versatility, acid-base properties and high surface area. Ni/Al_2O_3 is instead a good benchmark catalyst that has proven to work well both in thermal and in plasma-catalysis, the performance of which can be easily compared with the available literature.

3.3 Aim and Scope of the PhD Dissertation

The primary aim of this doctoral dissertation was to investigate the effect of non-thermal plasma of the NRP type on the progress of the dry reforming of methane (DRM) reaction using supported nickel-based catalysts based on modified hydrotalcites, alumina oxides, and ceramic foams modified with alumina oxides.

The scope of the study included:

- Synthesis of nickel-based catalysts supported on hydrotalcite using the co-precipitation method or incipient wetness impregnation.
- Preparation of nickel-based catalysts supported on alumina using adsorption from solution or impregnation.
- Synthesis of ceramic foams composed of $Y_2O_3-ZrO_2$ and α-Al_2O_3, including their modification with alumina oxides.
- Physicochemical characterization of the obtained catalytic materials using:
  - X-ray diffraction (XRD),
  - Fourier transform infrared spectroscopy (FTIR),
  - Carbon dioxide temperature-programmed desorption (CO_2-TPD),
  - Low-temperature nitrogen sorption,
  - Hydrogen temperature-programmed reduction (H_2-TPR),
  - Scanning Electron Microscopy with Energy Dispersive Spectroscopy (SEM-EDS)
- Application of the obtained catalytic materials in the dry reforming of methane process assisted by NRP plasma.
- Evaluation of the catalytic activity and selectivity of the catalysts.

The aim of the conducted research was to address current challenges related to the production of alternative fuels and the chemical utilization of carbon dioxide, thereby supporting industrial decarbonization.

Chapter 4

Methods

4.1 Introduction

This chapter serves as a toolbox that contains all the techniques and methods employed in the present research work. The first part is dedicated to the catalyst synthesis and characterization methods. A brief and general overview of the techniques is given, followed by a thorough description of the parameters and procedures used. The second part of the chapter is dedicated to plasma-catalytic DRM reaction characterization. Because the configuration of the plasma-catalytic setup changed with different experiments, detailed setup schematics will be discussed each time in the dedicated chapters. Here, we focus on illustrating the general characteristics of the nanosecond plasma discharge, the common electrical diagnostic elements, and the analytical methods employed to determine the reaction performance.

4.2 Characterization of catalytic materials

4.2.1 Infrared Spectroscopy (DRIFTS)

Diffuse Reflectance Infrared Fourier Transform Spectroscopy (DRIFTS) is an analytical technique based on the principles of infrared spectroscopy, that investigates the surface properties of heterogeneous materials. Unlike traditional transmission infrared spectroscopy, which requires infrared light to be transmitted by a sample, DRIFTS captures the light reflected off the sample surface, making it especially useful for opaque or highly scattering materials.

In DRIFTS, an infrared beam is shone onto the sample at an oblique angle. Part of the incident light is absorbed by the sample and the rest is scattered in various directions. The scattered light, which carries information about the vibrational modes of the molecules in the sample, is collected and analyzed. The Fourier Transform (FT) of the recorded signal converts the time-domain data into a frequency-domain spectrum, from which quantitative and qualitative information about the sample's molecular composition and structure can be derived.

The DRIFTS spectra were collected with a Frontier Optica spectrometer from PerkinElmer at AGH University. For each sample, 64 transmission spectra were recorded in *scan accumulation* mode, with a resolution of 1 cm^{-1} and in the wavelength range of 4000 cm^{-1} to 400 cm^{-1}. The catalytic samples were

dispersed in a potassium bromide matrix (KBr) with a ratio of 1: 200 mg. The finely ground mix was pressed into a disc pellet that was used for transmission measurements. Although KBr is mostly transparent to infrared radiation, its contribution was measured with an empty KBr pellet and subtracted.

DRIFTS measurements were acquired on the fresh hydrotalcite-like samples to assess the composition of the interlayer ions.

4.2.2 X-Ray Diffraction (XRD)

X-ray diffraction (XRD) is a non-destructive analytical technique widely used to characterize the crystallographic structure and composition of materials. In powder XRD, a beam of X-rays is directed onto a finely powdered sample, where it interacts with the sample's crystal lattice to produce a diffraction pattern. This pattern is unique to the crystallographic structure of the material and can be used to identify the phases present in the sample, the sample purity and the crystallite size. The relationship between the diffracting planes and the radiation is given by Bragg's law (4.1).

$$\lambda = 2d_{hkl}sin\theta \tag{4.1}$$

where λ is the wavelength of the X-ray radiation, d_{hkl} is the crystal lattice spacing of the diffracting planes (hkl) and θ is the diffraction angle.

In the field of catalysis, powder XRD is crucial in the design, synthesis, and optimization of catalytic materials. The phase composition and the structural changes of the samples are first monitored step-by-step during the synthesis process. Then, another comparison is drawn before and after the catalytic reactions. This insight is crucial for elucidating the relationship between the structure of the catalyst and its activity, stability, and selectivity. Furthermore, powder XRD can monitor the sintering or phase transformation of catalytic nanoparticles under reaction conditions, providing valuable information for the development of more effective and durable catalytic systems.

XRD analysis has been the main investigation technique used in this work to characterise the catalysts in all stages of their preparation and after being spent in the plasma-catalysis experiments (*post mortem*). For the reasons illustrated above, it is an established analysis technique in the catalysis and plasma-catalysis communities, because of its capability to detect the changes in the crystalline structure after calcination, reduction, and reaction in the catalytic environment. The non-destructive nature of XRD analysis is noted, as is its minimal sample preparation requirements and possibility to perform it *ex-situ*. Finally, the presence of two XRD instruments at the collaborating institutions facilitated extensive utilisation of this technique. This accessibility enabled frequent and comprehensive analyses throughout the research programme.

The XRD instrument at AGH University is an Empyrean diffractometer from PANalytical, equipped with a CuKα radiation source ($\lambda = 0.154059$ nm). The diffractograms were recorded in 2ϑrange from 10° to 90°. The catalytic samples were characterized *ex-situ* and respectively after their synthesis, calcination, reduction and *post-mortem*, i.e. after the reaction in plasma. After being crushed in an agate mortar, the powders were compacted in a flat disc in the sample holder. This was also true for the monolith foam materials.

The Scherrer equation (4.2) was used to retrieve the average crystallite size of the metallic Ni^0 particles:

$$D_{hkl} = \frac{\kappa\lambda}{\beta_{hkl} cos\theta} \tag{4.2}$$

where $\kappa = 0.89$ is the shape factor, λ is the X-ray wavelength, β_{hkl} is the half-width of the reflection and θ is the Bragg diffraction angle.

4.2.3 X-Ray Photoelectron Spectroscopy (XPS)

X-ray photoelectron spectroscopy (XPS) is an analytical technique based on the photoelectric effect. When a monochromatic beam of high energy photons (X-rays) is shone on a material, the latter will emit electrons from the top 1-10 nm of its surface. The emitted electrons are also called photoelectrons. The kinetic energy E_k with which a photoelectron is ejected is the measurable quantity in the experiment and the associated binding energy E_b can be recovered from Einstein's law (equation (4.3))

$$E_b = h\nu - (E_k + \phi) \tag{4.3}$$

where $h\nu$ is the energy of the incident photon and ϕ is the work function of the material. The binding energy of the electron depends on the electronic level from which it is extracted, and so it carries information about the elements present on the surface of the species, since every element is associated with a characteristic set of binding energies. However, qualitative information can also be inferred on the atom's oxidation state and neighboring chemical environment, by the observation of relative changes in a peak's binding energy, relative to a reference compound. These changes are named *chemical shifts*.

A XPS spectrum is constituted by three main components:

- a background signal;
- photoelectric peaks;
- Auger peaks.

The characteristic stepped background of an XPS spectrum shows a step at every peak, with increasing intensity at increasing electronic kinetic energies (i.e. decreasing binding energy). These are the photoelectrons that underwent an inelastic scattering process on their way to exit the surface. Before peak data analysis, the background should be accounted for and subtracted. The most widely used model for fitting the XPS background is the Shirley background [120].

The XPS spectrum appears as a series of peaks representing the number of electrons detected at specific binding energies. Each element detected on the material contributes with its characteristic set of lines. The area of the peaks is directly proportional to the density of that element in the volume of detection. The photoelectron peaks are labelled after the electronic level from which the electron has been extracted, using the nomenclature rule nl_j, where n is the principal quantum number, l is the orbital momentum number, $j = l + s$ is the total momentum number and s is the spin angular momentum number $s = \pm\frac{1}{2}$. Whenever the condition $l > 0$ is verified for the orbital momentum number, the peak is split into a doublet, due to the quantum-mechanical principle of spin-orbit coupling. The phenomenon of peak splitting takes the name of spin-orbit splitting. The energy difference between the doublet peaks is constant and is roughly proportional

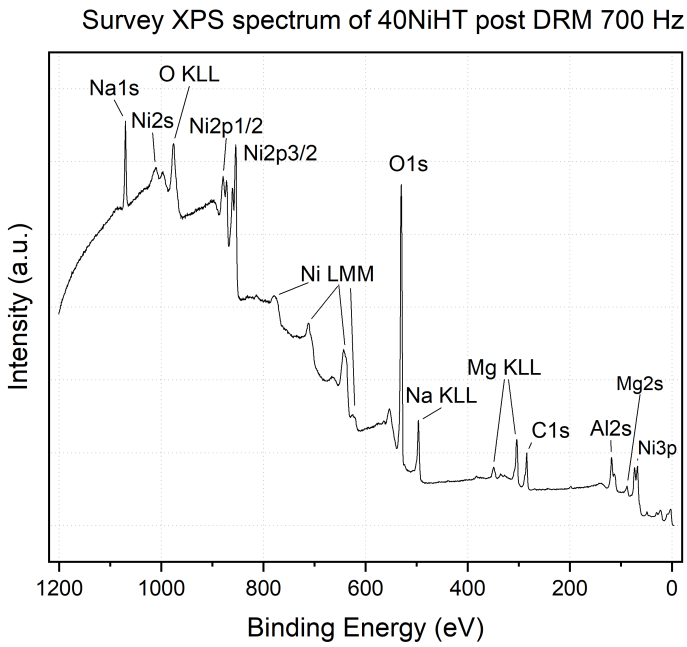

Figure 4.1. Survey XPS spectrum obtained from a 40 wt.% Ni/Al_2O_3 catalyst post DRM reaction with plasma. We can immediately notice the stepped background, with each step corresponding to a peak. Besides the photoelectric peaks, marked with the binome "*element symbol & orbital*", we can also notice some Auger peaks, of the type KLL and LMM.

to Z^5 of the element, where Z is the atomic number. It is important to know the energy value of spin-orbit splitting, which can be found in specific databases [121], as it is needed for the correct peaks fitting and identification, especially in case of chemical shifts larger than the spin-orbit splitting. The specific area ratio of the doublet peaks depends on the ratio between the degeneracy of the two states, where the degeneracy $(2j + 1)$ of the state *j* is defined as the number of possible orientations of the vector *j* in space, sharing the same spin-orbit coupling energy [122, 123].

The Auger effect is a process occurring as an inter-atomic response to the photoemission caused by high-energy photons or electrons. Following the emission of a photoelectron from a core level, the atom is left in an ionized, energetically unfavorable state with a vacancy formed in a low-lying orbital. A relaxation of this state is likely to occur with an electron from a higher orbital dropping down to fill the vacancy, thus releasing an excess energy, which in turn may provoke the emission of a secondary electron. The latter is called Auger electron, and its peculiarity is to possess a kinetic energy independent from the exciting radiation. Auger peaks have unique shapes and positions and are useful for both elemental identification and chemical state analyses. The notation used for the identification of Auger peaks considers all the levels involved in the process (e.g., from figure 4.1: LMM for Ni and KLL for O, Na and Mg).

The characterization of catalysts through the XPS technique has been known for quite some time, and both homogeneous and heterogeneous catalysts have benefited from it. Apart from the standard elemental analysis and oxidation state transformations, the technique still has a lot of potential to offer to material scientists. Either when employed in unconventional ways, like at low gas pressure [124] or in cryo-XPS

approach, or when combined with other analysis techniques, electronic, 2-dimensional, topological and structural information can be retrieved [122].

A correct interpretation of the peak deconvolution analysis must go together with a fundamental understanding of the technique and a correct manipulation of the data.

XPS spectra were recorded with a Kratos Analytical apparatus, under supervision of Dr. Nadhira Laidani. The spectra were analyzed via *RxpsG* software, developed at FBK Institute in Trento.[125]

4.2.4 Scanning Electron Microscopy and Energy-Dispersive X-ray Spectroscopy (SEM-EDS)

Scanning Electron Microscopy (SEM) is a high-resolution imaging technique, used to study the structure and morphology of materials at the micro- and nano-scale. A focused electron beam is scanned across the surface of the material sample, interacting with it and causing a flux of backscattered electrons, emitted photons and secondary electrons, carrying information about the material's structure and composition.

When integrated with Energy Dispersive X-ray Spectroscopy (EDS), SEM-EDS allows for an elemental and compositional mapping of the material. The characteristic X-rays produced from the interaction of the electron beam with the surface of the sample are collected and analyzed. This technique is applied both for qualitative and quantitative analysis, by studying, respectively, the wavelength and intensity of the X-rays.

The SEM-EDS was performed with the help of dr. Dorota Duraczynska at the Jerzy Haber Institute of Catalysis and Surface Chemistry, Polish Academy of Sciences in Krakow. Some SEM images taken on the monolith alumina catalysts were taken at the Industrial Engineering Department of the University of Trento, with the help of dr. Matteo Favaro.

4.2.5 Low-temperature N_2 adsorption

The surface area and pore properties of solid materials are crucial parameters in catalysis, as the surface is the medium through which all interactions with the external environment take place. While this is a trait in common with thermal catalysis, we also need to consider pore size as an important factor for plasma-surface interaction, as there is a correlation between the plasma Debye length and the possibility for a plasma streamer to propagate in a pore [126].

The surface area of the catalyst can be estimated using gas adsorption properties and the BET theory. BET theory takes its name from the authors Brunauer, Emmett and Teller, who extended the Langmuir model of monolayer gas molecule adsorption to multilayer adsorption, under the main assumption that the successive heats of adsorption for all layers except the first are equal to the heat of condensation of the adsorbate gas [127]. The BET equation (4.4) represents the multilayer adsorption isotherm, where P is the equilibrium pressure of the adsorbate at a given temperature, P_0 the saturation pressure, v (v_m) the volume occupied by the adsorbed gas molecules (in a monolayer) at a given relative pressure P/P_0 and C is a parameter related to the difference in the heats of adsorption.

$$\frac{P/P_0}{v[1-P/P_0]} = \frac{1}{v_m C} + \frac{C-1}{v_m C} P/P_0 \tag{4.4}$$

This equation can be represented in a linear form $y = A + Bx$, where $y = (P/P_0)/[v(1 - P/P_0)]$ and $x = P/P_0$, which holds in the interval $0.05 < x < 0.35$. The volume of the monolayer can then be recovered as the sum of the intercept and the slope of that line (4.5).

$$\frac{1}{v_m} = A + B \tag{4.5}$$

Once the monolayer is known, the BET surface area is obtained (4.6).

$$S_{BET} = \frac{v_m \cdot N_A \cdot \sigma_{N_2}}{V \cdot m} \tag{4.6}$$

where N_A is Avogadro's number, σ_{N_2} is nitrogen's absorption cross-section, V is the molar volume and m is the mass of the solid sample.

To obtain the isotherms for the BET surface area, samples are first degassed at 300°C overnight. The tube cells were then cooled under vacuum in a nitrogen thermal bath (-195°C). Gaseous nitrogen (the adsorbant) is then incrementally added in the probing tube in known amounts. At each step the quantity of adsorbed gas is determined once the pressure reaches equilibrium.

The isotherms of the powder catalysts were acquired with a Quantachrome Instruments Autosorb-1 analyzer at the Jerzy Haber Institute of Krakow. The monolith foams were instead characterized with a Micrometrics 3Flex analyser at AGH University. In the latter, specific cylindrical monolith foams of 0.8 cm ⌀x 2 cm were prepared, so that they could be inserted in the instrument tube cell. The mass of the samples used for the measurements was approximately 0.2 g.

The Barrett, Joyner and Halenda (BJH) theory [128] was used to analyse the adsorption and desorption isotherms, and thus determine the pore size distribution. The BJH method applies the Kelvin equation to relate the pore size to the relative pressure at which capillary condensation occurs within the pores. When the pressure increases, the gas will begin to condensate in the pores, starting from the smallest to the largest. Once the pressure is saturated, all pores are assumed filled with liquid, and the evaporation phase will be started, by gradually decreasing the pressure. The adsorption and desorption isotherms show an hysteresis cycle that is used to determine detailed information on the pore volume and size distribution, assuming cylindrical pore geometry.

4.2.6 Temperature Programmed Reduction (H_2-TPR)

Hydrogen Temperature Programmed Reduction (H_2-TPR) is an established analytical method in the characterization of catalytic materials, used to assess the reducibility of the active phase and to gain insight into the redox properties of the catalyst. The amount of hydrogen consumed by the sample is monitored while it is heated in a controlled, reducing H_2 atmosphere. As the temperature increases, reducible species within the catalyst progressively react, with the consumption of hydrogen being indicative of the reduction process. The temperature(s) at which the reduction occurs provides valuable information regarding the strength of the oxygen-metal interactions and the nature of the reducible oxides present.

H_2-TPR in catalysis helps in the identification of active phases and in the determination of the optimal reduction temperature for catalyst pre-treatment. Moreover, H_2-TPR can elucidate the presence of different oxidation states and their relative abundance, offering insights into the catalyst's behaviour under reaction

conditions. In the present work, H_2 was used to determine the ideal reduction temperature of the active nickel phase in both powder and foam catalysts and to observe the distribution of their oxidation states.

The analyses were conducted on all of the calcined catalysts at the Jerzy Haber Institute of Catalysis and Surface Chemistry, Polish Academy of Sciences in Krakow.

4.2.7 CO_2 Temperature Programmed Desorption (CO_2-TPD)

CO_2 Temperature Programmed Desorption (CO_2-TPD) is an analytical technique used to study the surface properties of catalysts, particularly their basic sites. In catalysis, particularly for reforming reactions, understanding the nature and strength of basic sites is crucial, as they influence catalytic activity and selectivity. Basic sites are the ones where CO_2 is adsorbed and they can oxidize carbon deposits formed during DRM reaction in the Bouduard reaction.

The basic theory behind CO_2-TPD involves adsorbing CO_2 on the surface of a catalyst at a low temperature and then gradually increasing the temperature to achieve its desorption. The desorption temperature is indicative of the strength of interaction between CO_2 and the catalyst surface. Generally, the sites are classified in three main categories:

- Weak Basic Sites: CO_2 desorbs at lower temperatures;
- Medium Basic Sites: CO_2 desorbs at intermediate temperatures;
- Basic Sites: CO_2 desorbs at higher temperatures.

The desorption profile, called TPD curve, helps in identifying the strength and distribution of these basic sites. Peaks in the desorption profile correspond to specific interactions between CO_2 and the basic sites on the catalyst.

The CO_2-TPD studies were performed in a fixed bed flow reactor with online detection using a mass spectrometer (QMS). Catalysts (0.05 mg) were reduced *in situ* prior to measurement in a 5% H_2/Ar mixture (flow rate of 30 mL/min) from RT to 750 ^oC with a heating rate of 10 ^oC/min. After cooling the reactor in He flow to room temperature, pulsed CO_2 adsorption (5% CO_2/Ar) was conducted from a 250 μL calibration loop until the surface was saturated. Desorption measurements were performed in He flow (flow rate of 30 mL/min) from RT to 750 ^oC with a heating rate of 10 ^oC/min. During TPD, the mass-to-charge ratio of CO_2 (m/z = 44) was monitored.

4.3 The General Reactor Design

While the specific reactor configurations studied for each plasma-catalytic integration will be treated in detail in their respective chapters, here a general overview of the basic setup and the common elements is necessary This way, it will be easier to understand the following sections that focus on reaction analysis and on the electrical characterization of the plasma discharge.

The general experimental setup is shown in figure 4.2. The discharge is operated at atmospheric pressure (980 mbar at the Department of Physics of Trento) in a pin-to-pin configuration. The reactant gases - CO_2

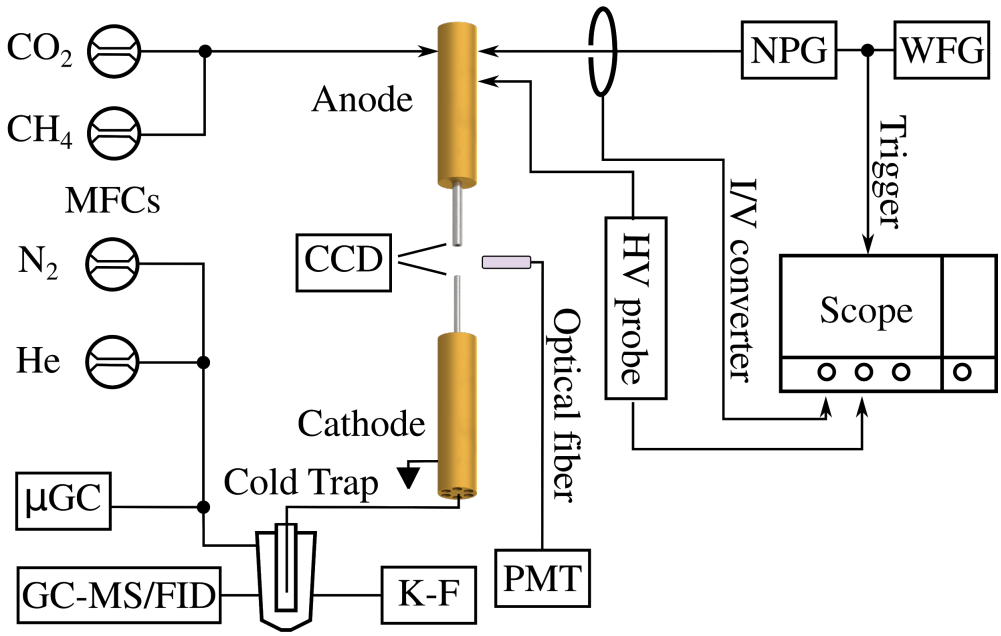

Figure 4.2. General experimental setup of the NRP plasma reactor for DRM reaction. MFCs: mass flow controllers; K-F: Karl-Fisher volumetric titrator; PMT: photomultiplier tube; HV probe: high voltage probe; NPG: nanosecond pulse generator; WFG: waveform generator.

and CH_4 in a 1:1 ratio - are fed to the discharge through the high voltage electrode (anode). The flows are regulated by two mass flow controllers (MKS Type 1179A General Purpose Mass-Flo® Controller). The effluent gas mixture exits the reactor from the ground electrode (cathode), after which it is filtered from possible dust and carbon particles through a paper filter (20 μm, Whatman 41) and a stainless steel particulate filter (0.5 μm pore size). After filtering, the high vapor pressure products of reaction (mainly water and C3-C4 hydrocarbons) are separated by condensation in a stainless steel cold finger immersed in a thermal bath of ethanol, which is kept at constant temperature ((-30 $\pm$ 5)°C) with a Peltier module that uses liquid nitrogen as cooling source. Past the cold trap, the gas mixture is diluted in N_2 and He is added as internal standard. A micro-Gas Chromatographer analyses the gas composition, preceded by a desiccant barrier of $CaCl_2$ beads for moisture absorption. The line is evacuated by a scroll pump (Edwards) at the end of the gas line.

Regarding the electrical configuration, the pulsing scheme is first selected with a waveform generator (32250A, Agilent Technologies), driving the nanosecond pulse generator (NPG-18/100k, MegaImpulse Ltd.). A 3 m PK 75-7-15 (MegaImpulse Ltd.) coaxial cable with 75 Ω impedance matched to the NPG carries the high voltage signal to the anode electrode, while the cathode is grounded. The applied voltage V(t) and current I(t) signals are collected at the anode electrode, respectively with a high-voltage probe (P6015A, Tektronix, BW = 75 MHz) and a high frequency I/V converter (High Frequency Current Transformer HFCT CT-C1.0-BNC, Magnelab, BW = (200 Hz - 500 MHz)). I(t) and V(t) signals were then read and acquired by a digital oscilloscope (HD09104 Teledyne Lecroy, BW = 1 GHz) with a sampling rate of 20 GS s^{-1}.

Customizable reactor design and careful material selection were essential requirements posed by the peculiarities of our NRP discharge. The signal's fast, high-voltage pulses required high-quality electrical

contacts, impedance matching, precise grounding, and robust electromagnetic shielding. Poor electrical contacts can cause the insurgence of parasitic capacitance and parasitic discharges, increase resistance, leading to localized heating and energy losses and posing safety hazards [129]. Impedance mismatch along the transmission line causes signal reflections at the conductors interface, ending up in power loss. Inadequate grounding can result in stray currents such as ground loops, leading to noise and interference, and potential damage to sensitive components. Poor shielding leads to significant electro magnetic interference (EMI), disrupting nearby electronics, and degrading reactor performance. These considerations reinforce the importance of robust design and engineering practices in ensuring reliable and efficient operation under demanding conditions.[130]

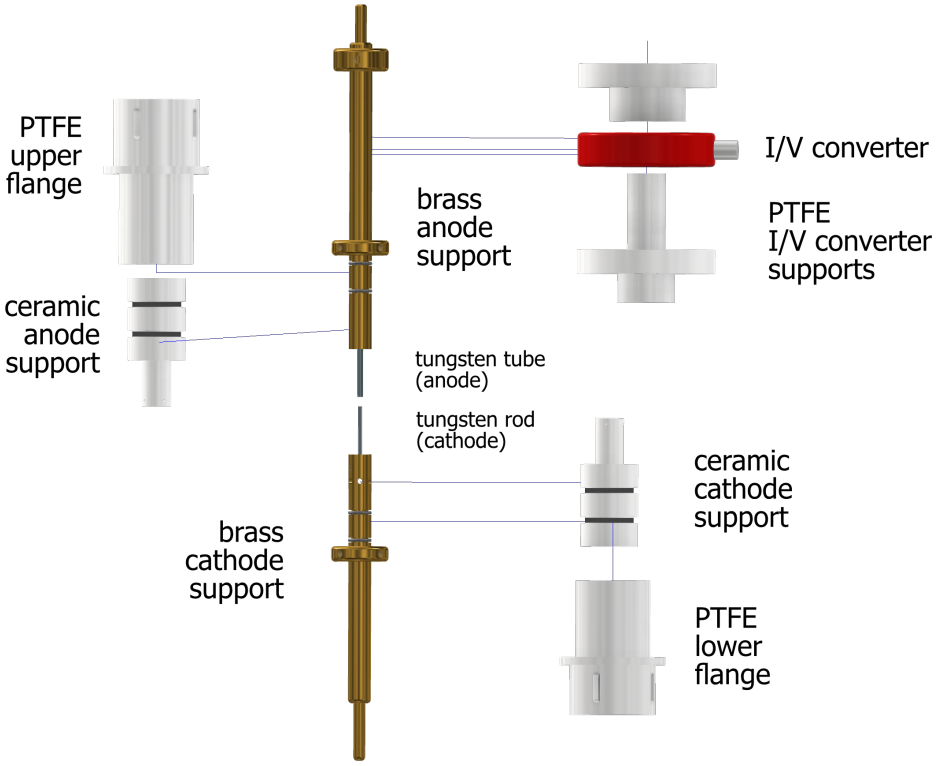

Figure 4.3. CAD schematic of the NRP discharge electrodes and their supports. Based on the CAD design, except for the tungsten electrodes, the reactor pieces were custom-made at the University of Trento. Image created using Autodesk Inventor Professional software.

The detailed CAD of the electrodes and their supports is shown in figure 4.3. Except for the tungsten electrodes, all the elements shown were custom designed and manufactured in Trento, tailored to meet the specific needs of the NRP discharge and of our experiment.

The anode electrode is a tungsten tube with an outer diameter of 3 mm and an inner diameter of 2 mm; the cathode electrode is a tungsten rod with a diameter of 2 mm. Tungsten (W) was chosen for its high resistance to erosion, caused by the localized NRP discharge.

Each tungsten element is embedded in a larger cylindrical brass support, serving different functions. Brass is a conducting and relatively soft material that ensures good electrical contacts and can be moulded easily. Thus, it helps to avoid the formation of unwanted parasitic discharges at the junction of the conduc-

tors, and it allowed the drilling of channels throughout the length of the cylindrical elements, meant for the inflow and outflow of gases to and from the reactor.

These brass supports were inserted into cylindrical coaxial MACOR® ceramic holders. This technical material was chosen because of a variety of properties that it offers [131]:

- Mechanical: easily machinable material with tight engineering tolerance, ensures micrometric precision in the interlocking of reactor elements;
- Physico-chemical: its surface is non-porous, so it avoids the formation of surface ricombination centers;
- Thermal: it is stable up to 1000°C and its thermal expansion coefficient is similar to most metals';
- Dielectric: it is an electrical insulator with high dielectric constant on a broad frequency spectrum and at high voltages.

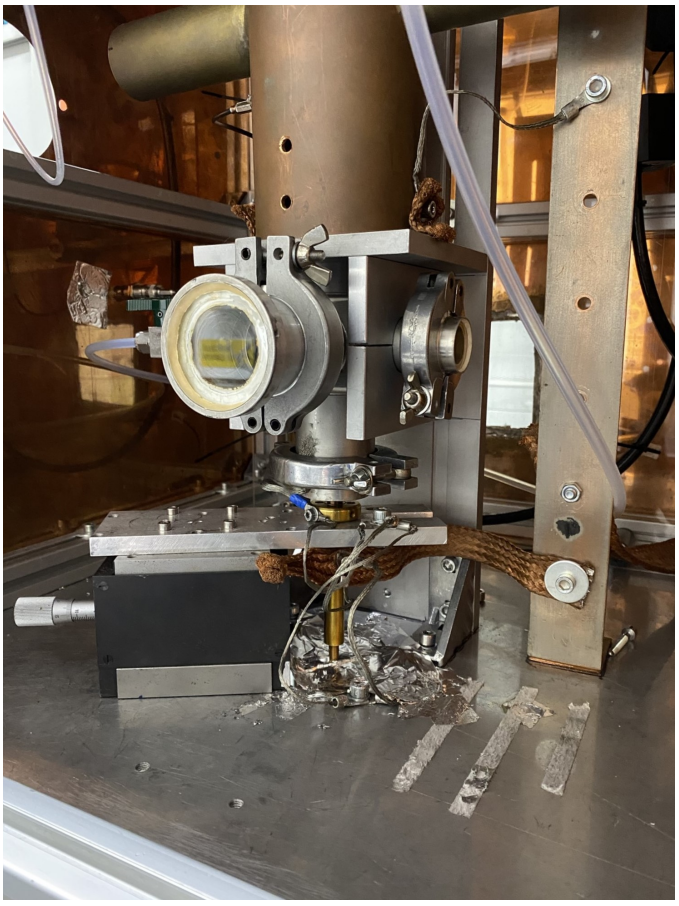

Figure 4.4. Picture of the reactor stainless steel cross chamber, accommodating the front window, lateral window (on the right), lateral access for gas pressure gauge (hidden on the left) and the electrodes flanges. The lower electrode (cathode) is grounded to the Faraday cage through a copper strip and it is supported by a vertical translation stage fork, used to adjust the inter-electrode gap. The upper electrode complex, that comprises the anode electrode, HV probe, HV supply cable and I/V converter, is hidden inside the brass Faraday cage *totem*.

Sealing of electrode support elements in the reactor was achieved by embedding the MACOR® elements in a Teflon flange each, which were inserted into the vertical arms of the stainless steel reactor chamber. The reactor chamber was a stainless steel 5-way ISO-KF flange cross element. Its five accesses accommodated the front window, lateral window, and lateral access for gas pressure gauge on the horizontal plane. The vertical arms hosted the anode and cathode electrode flanges. The cathode was supported by a vertical translation stage fork, used to adjust the inter-electrode gap.

EMI shielding and grounding were a very important part of reactor assembly, as mentioned above. Outside of the reactor chamber, the anode stage was shielded by a first inner brass Faraday cage ("the totem"), which enclosed the protruding anode electrode support, HV probe, HV supply cable and I/V converter. Then, a bigger Faraday cage accommodated the reactor chamber, the totem and most of the cathode stage, including the vertical translation stage, used to adjust the inter-electrode gap. All the cables were shielded with aluminium foil and ferrite beads. Electromagnetic noise was monitored during discharge operation with a portable field meter (PMM 8053, Narda) equipped with a EP-330 probe (BW 300 kHz-3 GHz).

4.4 Reaction Analysis

Reaction performance is evaluated in this thesis from an analytical approach, referring to the macroscopic parameters. Considering the plug-flow reactor model [132], this means to measure and compare the number of moles (or the molar flow rate) of each species at the entrance and exit of the reactor. In this framework, where the analytical instruments are put in line with the reactor, this concept translates into measuring said quantities when the plasma discharge is off and when it is on. We call the measure when the plasma is off a 'blank'. This section gives an overview on the analytical tools that were used (gas chromatography and the Karl Fischer technique). In the final section, we discuss the data analysis that led to the determination of the reaction performance parameters, such as reactant conversion and product selectivity.

4.4.1 Gas Chromatography

Gas chromatography (GC) is a technique used for the separation and analysis of compounds in mixed gas samples. A typical GC module consists of three main subsystems: an injection module, a separation module and a detection module. A known volume of gas analyte is injected into a long analysis column, which is internally coated with a stationary phase. The analyte is transported through the column by a carrier gas (usually a high purity inert gas such as helium, hydrogen, or argon), also known as the *mobile phase*. As the sample travels through the column, its components interact differently with the stationary phase, causing them to elute at different times. These differences allow for the separation of complex mixtures into individual components. The separated compounds finally go through the detection module, that translates some physical or chemical properties of the detected species into a measurable signal. Some notable examples of detectors and their main characteristics are summarized in table 4.1.

Table 4.1. Most common types of Gas chromatography detectors and their main characteristics.[133]

Detector		Description	Destructive	Linear dynamic range	Selectivity
TCD	Thermal Conductivity Detector	Measures changes in thermal conductivity of carrier gas due to vaporized analyte.	No	$> 10^5 (\pm 5\%)$	Permanent gases, light hydrocarbons, fatty acids
FID	Flame Ionization Detector	Measures ions from organic compound combustion in H_2/air flame.	Yes	$> 10^7 (\pm 10\%)$	Most organic compounds
MS	Mass Spectrometry	Measures mass-to-charge ratio of ionized compounds.	Yes		
NPD	Nitrogen-Phosphorus Detector	Detects N and P compounds ionized by heated metal bead.	Yes	$> 10^5 (\pm 5\%)$	N- and P-containing drugs, pollutants
ECD	Electron Capture Detector	Measures electron flow reduction when electronegative compounds capture electrons.	No	$> 10^5 (\pm 5\%)$	Halogens, nitrates, peroxides
FPD+	Flame Photometric Detector	Measures light emitted in S and P spectrum during H_2/air flame combustion.	Yes	$> 10^5 (\pm 5\%)$	S and P compounds

We call *retention time* the time interval between the injection and detection of a component. It can be influenced by different factors, such as the length and diameter of the column, the nature of the stationary phase (therefore its selectivity and efficiency toward a specific substance) and the conditions under which the chromatography is performed.

A chromatogram is a sequence of peaks at different retention times. The integral area of the peak is proportional to the analyte concentration detected, while the retention time of the peak is bound to the identity of the compound. A calibration standard with compounds at known concentrations is necessary to determine the retention time of the target species.

The analysis of the reactor effluent gases was mainly performed with an in-line micro gas chromatographer (3000 μGC, Agilent Technologies), equipped with a TCD detector and two columns:

- a Molsieve column (5A, 20 m + backflush) to detect the lighter species in the gas mixture, such as H_2, N_2 and CO;
- a Plot U column (Poraplot, 10 m) to detect CO_2, CH_4 and simple hydrocarbons such as C_2H_2, C_2H_4, C_2H_6 and C_3H_8.

Part of the measurements was also performed with another μGC model, which replaced the previous one: 990 μGC (Agilent Technologies), also equipped with Molsieve and Plot U columns.

The analysis routine of the μ GC consisted of eight equally spaced short analyzes, acquired when the steady-state condition was reached. The volume of the gas line and flows were also taken into account to calculate the time the gas takes to get from the reactor to the analyser.

In the chromatogram of the μGC, the integral area of the peak is proportional to the relative molar concentration of an analyte in the sampled volume, i.e. its molar fraction m_i. The target compound concentration can only be obtained after calibration with known analyte mixtures, so that the response factor f_i of each gas species can be determined. The molar fraction of compound X will be:

$$m_X = \frac{A_X}{f_X} \tag{4.7}$$

where A_X is the integral peak area for the species X. This linear correspondence between molar fraction and peak area is only valid in a limited region of the whole dynamic range of the μGC, because the response of the TCD detector at high concentrations tends to saturate. For this reason, a dilution of the gas mixture was required. The dilution of the analyte mixture was performed right at the entrance of the μGC using nitrogen, in proportion towards the process gas of circa 3:2. The response factors of the target compounds were determined through an external standard calibration procedure. Four different gas mixtures were prepared, simulating the range of interest of the analyte concentrations in the effluent gas mix. The compounds employed had N5 minimum purity (99,999% pure).

A GC-MS (Trace GC Ultra, Finningham) equipped with a FID detector was used to detect and analyse both C3-C4 hydrocarbons in the gas phase and liquid hydrocarbons. In particular, a Plot Q column (HP-PLOT Q, Agilent J& W) was equipped to analyse the gas phase and the polar liquid hydrocarbons, mainly methanol and carboxylic acids.

For the samples in the gas phase, propane (C_3H_8) co-eluted with propyne (C_3H_4) was used as internal standard. These compounds could in fact be detected by both the GC-FID and the μGC, making their molar fraction m_{IS} known. The FID response factors for C3-C4 hydrocarbons were calculated based on the concept of Effective Carbon Number (ECN) [134] (eq. 4.8).

$$F_X = \frac{M_X \cdot ECN_{IS}}{M_{IS} \cdot ECN_X} \tag{4.8}$$

where M_X represents the molecular weight of the X species, M_{IS} the molecular weight of the internal standard compound (here propane), ECN_X is the Effective Carbon Number of the X species, while ECN_{IS} is the Effective Carbon Number of the internal standard. The molar fraction m_X of the gaseous species X is then given by:

$$m_X = m_{IS} \cdot \frac{A_X}{A_{IS}} \cdot F_X \tag{4.9}$$

where A represents peak area and m_{IS} is the molar fraction of the propane standard. This method introduces an estimated uncertainty of 10% for C3-C4 hydrocarbons [135]. When calculating selectivity, which incorporates conversion data, the cumulative error may reach 40%.

To detect and qualitatively estimate the presence of nonpolar liquid hydrocarbons, a DB-5 column was equipped in the GC-MS.

4.4.2 Characterization of liquid products

The liquid products condensed in the cold trap, which included water and liquid hydrocarbons, were treated in two different ways.

For the detection of water and polar hydrocarbons, the condensed liquid was diluted in 10 mL of acetonitrile (CH_3CN), with 100 μL anisole (C_7H_8O) as internal standard. 1μL of solution was manually injected into the GC-MS (T_{inlet} = 270°C, T_{FID} = 300 °C).

FID response for methanol and C1-C4 carboxylic acids was obtained from the external standard calibration method, using standard solutions of reagent grade purity chemicals in acetonitrile. The molar fractions in the liquid are converted to gas-phase molar fractions by considering the sample volume, density, and discharge duration. Initially, the volume of each analyte is determined from its concentration in the liquid sample:

$$V_{X,l} = m_{X,l} \cdot V_{tot,l} \tag{4.10}$$

This volume is then used to calculate the number of moles n_X, taking into account the density and molar mass of the compound:

$$n_X = \frac{V_{X,l} \cdot \rho_{solvent}}{M_X} \tag{4.11}$$

where the numerator is the mass of X and the denominator is its molar mass. The mass of X is given by its volume in the liquid $V_{X,l}$ times the density of the liquid, that we can approximate with the density of the solvent $\rho_{solvent}$, since $V_{solvent} >> V_X$. Subsequently, molar flow rates are derived considering the duration of the discharge:

$$\dot{n_X} = \frac{n_X}{\Delta t_{plasma\,on}} \tag{4.12}$$

The molar flow rates are then converted to volumetric flow rates using the molar volume at standard temperature and pressure v_m:

$$\Phi_{X,g} = \dot{n_X} \cdot v_m \tag{4.13}$$

The final step involves estimating the molar fraction in the gas phase by comparing the calculated volumetric flow to the total output flow, whilst accounting for any expansion factor:

$$m_{X,g} = \frac{\Phi_{X,g}}{\Phi_{tot}^{out} \cdot \xi} \tag{4.14}$$

For the detection of nonpolar liquid hydrocarbons, the condensed liquid was diluted in 10 ml of hexane ($CH_3(CH_2)_4CH_3$), with 10 μL anisole as internal standard. Due to the qualitative purpose of these analyses, no FID calibration was performed. 1μL of solution was manually injected into the GC-MS (T_{inlet} = 270°C, T_{FID} = 300 °C).

Water was titrated via Karl-Fischer analysis, as will be explained in the following section. Polar and nonpolar liquid hydrocarbons were analysed in the GC-MS, as described in the previous section.

Karl-Fischer water titration

Karl Fischer (KF) water titration analysis is a precise and robust method to determine water content in samples [136]. It is based on the quantitative reaction of water with iodine and sulfur dioxide in the presence of a base (usually pyridine or imidazole) and an alcohol (typically methanol). The reaction that describes this process is the Bunsen reaction (4.15), where water and iodine are consumed with a molar ratio of 1:1.

$$2\,H_2O + SO_2 + I_2 \longrightarrow H_2SO_4 + 2\,HI \tag{4.15}$$

Together with the Bunsen reaction, a neutralization reaction (4.16) will also take place:

$$H_2SO_4 + 2\,RN \longrightarrow (RN)_2SO_4 \tag{4.16}$$

where RN is the base used.

Volumetric titration is recommended to determine the water content in samples between 0.1 and 100% [137]. In an electrochemical cell, a known mass of analyte is added, and the KF reagent is gradually introduced from a burette. While water is consumed in the reaction, a voltage is developed through a double platinum electrode immersed in the solution. Once all of the water in the sample is exhausted, an excess of iodine is found in the cell, and the voltage at the electrodes drops, signaling the end of the titration process. The known volume of reagent consumed at this point gives the water percentage weight fraction $w^{\%}_{H_2O}$. Under the assumption that in our sample $mass_{H_2O} << mass_{solvent}$, we consider $mass_{tot} \approx mass_{solvent}$.

Therefore:

$$mass_{tot} = V_{tot} \cdot \rho_{solvent} \tag{4.17}$$

where $\rho_{solvent}$ is, in our case, the density of acetonitrile ($\rho_{CH_3CN} = 0.786 mg/\mu L$). The mass of water in the sample can be retrieved as:

$$mass_{H_2O} = mass_{tot} \cdot w^{\%}_{H_2O} \tag{4.18}$$

from which the moles of water produced are given by:

$$n_{H_2O} = \frac{mass_{H_2O}}{M_{H_2O}} \tag{4.19}$$

where $M_{H_2O} = 18$ g/mol is the molar mass of water.

KF titration was performed with a Mettler Toledo V10S volumetric titrator. The titrating agent was Hydranal-Composite 5 by Honeywell. The solvent was Hydranal - Methanol Rapid by Honeywell.

4.4.3 Determination of Conversion and Selectivity

The following section is intended to give a comprehensive discussion on how reactant conversion and product selectivity were determined, starting from the quantities provided by the analytical instruments presented above. The aim is to provide practical tools to follow the data analysis process from the instrument's output to the numbers represented in the results section. Emphasis will be given to plasma-specific factors that need to be taken into account, such as gas expansion and the use of internal standards.

In plasma reactions the high-energy environment can lead to complex chemical transformations, including dissociation, recombination, and formation of new species. These processes often result in a change in

the total number of moles present in the system before and after the reaction. The mole expansion factor (ξ) quantifies this change and is typically expressed as the ratio of total moles of products to total moles of reactants 4.20. The mole expansion factor is crucial for accurate quantification of reactant conversion and product selectivity. Pinhão et al. [138] applied the study of ξ to plug-flow reactors and the DRM reaction, and demonstrated that neglecting ξ can introduce a significant systematic error.

$$\xi = \frac{n_{tot}^{out}}{n_{tot}^{in}} \tag{4.20}$$

In the frame of DRM reaction, there is an increase in the number of moles during the reaction, which makes $\xi > 1$.

To estimate the mole expansion factor, several methods can be employed. One recommended approach involves the use of an Internal Standard (IS), typically an inert gas such as helium, added in a known constant quantity between the reactor exhaust and the analyzer. Since a µGC samples fixed volumes of gas, the change in IS concentration provides a direct measure of the mole expansion.

$$\xi_{IS} = \frac{A_{IS}^{off}}{A_{IS}^{on}} \equiv \xi > 1 \tag{4.21}$$

where we adopted the convention A_{off} for the area measured when the discharge is off and A_{on} for the area measured when the discharge is on. Once determined, the mole expansion factor is incorporated into the conversion and selectivity calculations.

The molar fractions used in the mass balance, conversion and selectivity calculations were the mean of 6 molar fractions of equation (4.7), obtained under steady state conditions, and given with their standard deviation.

As a first step, we calculate the mass balance in time at the µGC (before water) toward carbon, hydrogen, and oxygen as:

$$B^C(\%) = 100 \cdot \frac{\xi\,(m_{CH_4}^{on} + m_{CO_2}^{on} + m_{CO}^{on} + \sum_y 2m_{C_2H_y}^{on} + 3m_{C_3H_8})}{m_{CH_4}^{off} + m_{CO_2}^{off}} \tag{4.22}$$

$$B^H(\%) = 100 \cdot \frac{\xi\,(2m_{H_2} + \sum_{y=2,4,6} y \cdot m_{C_XH_y} + 4m_{CH_4}^{on} + 8m_{C_3H_8})}{4m_{CH4}^{off}} \tag{4.23}$$

$$B^O(\%) = 100 \cdot \frac{\xi\,(2m_{CO_2}^{on} + m_{CO}^{on})}{2m_{CO_2}^{off}} \tag{4.24}$$

Reactant conversion was calculated as:

$$\begin{aligned} C_X(\%) &= 100 \cdot \frac{m_X^{off} - \xi \cdot m_X^{on}}{m_X^{off}} \\ &= 100 \cdot \frac{m_X^{conv}}{m_X^{off}} \end{aligned} \tag{4.25}$$

The species X can be in turn CH_4 or CO_2 and m_{off}, m_{on} is the molar fraction when discharge is off or on, respectively.

We calculate the gaseous products selectivities to carbon, hydrogen or oxygen as:

$$S^{C}_{CO}(\%) = 100 \cdot \frac{\xi \cdot m_{CO}}{m^{conv}_{CH_4} + m^{conv}_{CO_2}} \tag{4.26}$$

$$S^{H}_{H_2}(\%) = 100 \cdot \frac{\xi \cdot 2\, m_{H_2}}{4\, m^{conv}_{CH_4}} \tag{4.27}$$

$$S^{O}_{CO}(\%) = 100 \cdot \frac{\xi \cdot m_{CO}}{2\, m^{conv}_{CO_2}} \tag{4.28}$$

$$S^{C}_{C_X H_y}(\%) = 100 \cdot \frac{\xi \cdot x\, m_{C_X H_y}}{m^{conv}_{CH_4} + m^{conv}_{CO_2}} \tag{4.29}$$

$$S^{H}_{C_X H_y}(\%) = 100 \cdot \frac{\xi \cdot y\, m_{C_X H_y}}{4\, m^{conv}_{CH_4}} \tag{4.30}$$

where always $m^{conv}_{X} = m^{off}_{X} - \xi \cdot m^{on}_{X}$.

Let us now discuss the selectivities of the liquid products. First, we should consider that the efficiency of the cold trap is not 100%. As a consequence, what we determine is a lower limit of formation of the liquid products. Up to now, we worked with the molar fractions referring to the total flux reaching the µGC, which takes into account the added dilution. However, when liquid products are taken into account, we must be careful and compare molar fractions referred to the same volumetric flows. For this reason, we might either re-scale the molar fractions of liquids with respect to the diluted gas mixture entering the µGC, or re-scale the molar fractions of the other species, with respect to the the flux at the exit of the reactor, which does not involve dilution. We chose to re-scale the molar fraction of the gaseous species X as described below:

$$m^{on/off,*}_{X} = m^{on/off}_{X} \frac{100}{(100 - m^{on/off}_{N_2})} \tag{4.31}$$

and the molar expansion factor is re-scaled as well:

$$\xi^{*} = \xi \frac{100 - m^{on}_{N_2}}{100 - m^{off}_{N_2}} \tag{4.32}$$

As for water selectivity calculations, we had retrieved the number of moles of water produced in the reaction n_{H_2O} with equation (4.19). The molar fraction $m_{\mathrm{H_2O}}$ of water is the ratio between the volumetric flow of water produced and the total volumetric flow exiting the reactor:

$$m_{\mathrm{H_2O}} = \frac{\Phi^{out}_{\mathrm{H_2O}}}{\Phi^{out}_{tot}} \tag{4.33}$$

where:

$$\Phi^{out}_{\mathrm{H_2O}} = \frac{V_{\mathrm{H_2O}}}{\Delta t_{plasma\,on}} = \frac{n_{\mathrm{H_2O}} \cdot v_m}{\Delta t_{plasma\,on}} \tag{4.34}$$

and

$$\Phi^{out}_{tot} = \Phi^{in}_{tot} \cdot \xi \tag{4.35}$$

where v_m is the molar volume, $\Delta t_{plasma\,on}$ is the time duration in which the plasma is on, and ξ is the mole expansion factor. [1]

From the re-scaled molar fractions and molar expansion factor, we can check again the implemented mass balances towards C, O and H and we can compute the selectivities for water towards O and H as:

$$S^{H}_{H_2O}(\%) = 100 \cdot \frac{\xi^* \cdot 2\, m^*_{H_2O}}{4\, m^{conv,*}_{CH_4}} \tag{4.36}$$

$$S^{O}_{H_2O}(\%) = 100 \cdot \frac{\xi^* \cdot m^*_{H_2O}}{2\, m^{conv,*}_{CO_2}} \tag{4.37}$$

Lastly, we check the consistency of the analytical methods calculating the carbon, hydrogen and oxygen lacks as in equations (4.38) to (4.40). The lack of a specific element is the amount of that element that has been converted in a reaction, but is not detected in the analyzed products.

$$L^C = \frac{m_{CH_{4,conv}} + m_{CO_{2,conv}} - (m^{on}_{CO} + x \cdot m^{on}_{C_xH_y})}{m_{CH_{4,conv}} + m_{CO_{2,conv}}} \tag{4.38}$$

$$L^H = \frac{4 \cdot m_{CH_{4,conv}} - (y \cdot m^{on}_{C_xH_y} + 2 \cdot m^{on}_{H_2O})}{4 \cdot m_{CH_{4,conv}}} \tag{4.39}$$

$$L^O = \frac{2 \cdot m_{CO_{2,conv}} - (m^{on}_{CO} + m^{on}_{H_2O})}{m_{CO_{2,conv}}} \tag{4.40}$$

4.5 Plasma diagnostics

This section discusses the characterization of the NRP discharge plasma used in this study. The discharge was characterized through electrical diagnostics. Voltage and current signals from the NRP discharge were measured and processed to determine key parameters such as pulse energy, power, and Specific Energy Input (SEI). Given the peculiarities of the NRP discharge, said tasks are not trivial and will be thoroughly discussed in this section.

NRP discharges produce nanosecond-scale high-voltage pulses at high repetition rates, typically in the kHz range, which allows for efficient plasma generation, while limiting gas heating. The pulses are characterized by fast rising times, in the order of nanoseconds, and a Full Width at Half Maximum (FWHM) around 10 ns. This means, as pointed out by Khomenko et al. [139], that signal wavelength becomes comparable with the physical size of the system, thus causing the *cables-electrodes-plasma* system to behave as a transmission line. As a consequence, impedance matching becomes essential. As anticipated in section 4.3, this is important to avoid power reflections at the interfaces and to achieve maximum energy transfer. Therefore, reactor configuration and the choice of the diagnostics tools and their location must be carefully considered and optimized.

The voltage across the discharge gap was measured using a high-voltage probe, while the discharge current was monitored with an I/V converter. These time-resolved voltage and current signals were captured on a high-bandwidth oscilloscope (all the details can be found in section 4.3).

[1] All the conversions between units of measurement and orders of magnitudes were taken into account in the calculations (e.g. $1\ sccm = 22.41\ L/mol \cdot 1000$ under STP conditions).

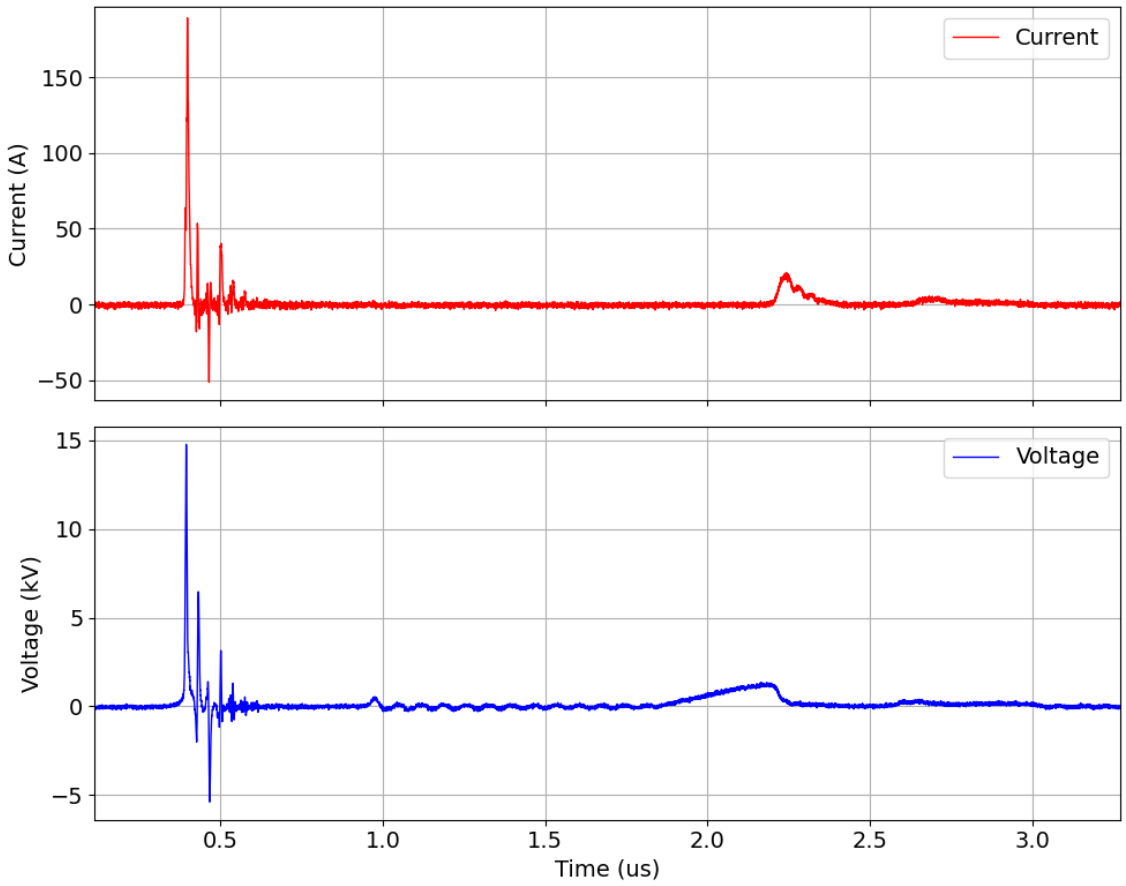

Figure 4.5. Example of V(t) (blue signal) and I(t) (red signal) signals of a single pulse of the NRP discharge. We can here see the macroscopic characteristics of the pulse shape. After $\sim$ 0.5 ns from the breakdown there is a re-trigger of the NRP generator. Another pulse is also produced by the generator after $\sim$ 1.7 µs from the first breakdown. Pulsing frequency: 1400 Hz, inter-electrode gap: 5 mm, gas mixture of CO_2 and CH_4 in a 1:1 ratio, Total flux: 300 sccm, SEI = $(2.4 \pm 0.1)(kJ/dm^{-3})$.

An example of current I(t) and voltage V(t) signals produced by the NRP discharge alone (no catalysts) are shown in figure 4.5 and figure 4.6 (close-up). The signals represent a single pulse in a continuous pulse mode at 1400 Hz frequency, with a flux of 300 sccm of CH_4:CO_2 in a 1:1 ratio. The inter-electrode gap was set to 5 mm and the SEI was calculated to be $(2.4 \pm 0.1)kJ/dm^3$.

The characteristics of these signals are in line with the average behavior of the discharge under the same steady-state conditions. We first see that the first pulse is followed by a series of secondary pulses of decreasing intensity. This is due to the pulse energy reflections that occur at the interface with the load due to impedance mismatch. These reflections occur approximately every 30 ns, which is the time it takes the signal to travel in the transmission cable twice. At each reflection cycle some energy is lost behind and the signal is damped. After approximately 0.4 µs from the breakdown a new series of small pulses can be seen in the voltage signal, which is ascribed to a re-trigger of the NPG. The second event after the breakdown, visible around 1.7 µs from the first pulse, is always produced by the NPG generator in use, and it also produced a secondary breakdown. The FWHM of the pulse is around 10 ns, the rise time less than 4 ns. The

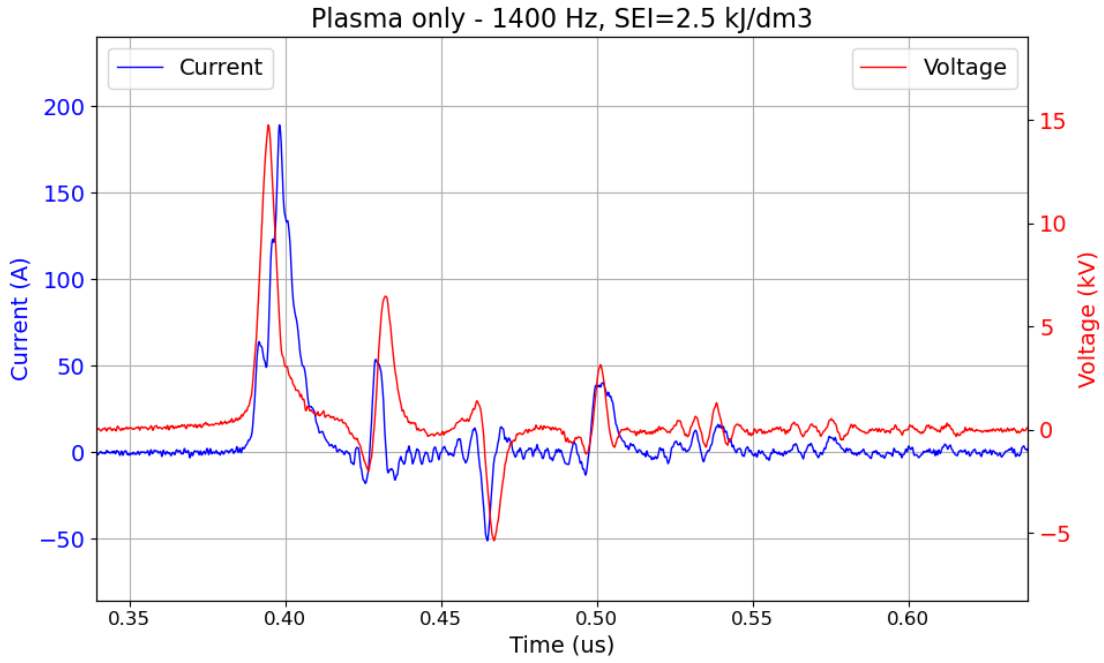

Figure 4.6. Close-up of the voltage and current signals shown in figure 4.5. We can appreciate a clearer view of the secondary pulses generated by reflections at the load, their time spacing, and their dumped behaviour. V(t) - blue signal and I(t) - red signal. Single pulse of the NRP discharge. Pulsing frequency: 1400 Hz, inter-electrode gap: 5 mm, gas mixture of CO_2 and CH_4 in a 1:1 ratio, Total flux: 300 sccm, SEI = $(2.4 \pm 0.1)(kJ/dm^{-3})$.

voltage amplitude was tuned down to be around 15 kV. However, the NRP generator is able to deliver up to 18 kV of maximum voltage on a matched load of 75 Ω, when tuned at maximum capacity.

The temporal evolution of the discharge was monitored through eight successive measurements of V(t) and I(t) signals throughout each experimental run. Each measure consisted in the acquisition of 30 [V(t),I(t)] signal pairs of the pulse. The acquisitions were controlled and automated through a LabView routine, that could read the oscilloscope in real time.

Post-processing of the waveforms involved calculating instantaneous power and integrating over time to obtain the energy per pulse (equation (4.41)).

$$E_p = \int_{\Delta t_p} V(t-\tau) \cdot I(t) dt \tag{4.41}$$

where Δt_p is the pulse time interval. The pulse energy E_p was evaluated for each pair of voltage and current signals to obtain its average value and the related standard deviation (equation (4.42)).

$$\langle E_p \rangle = \frac{1}{30} \sum_{i=1}^{30} \int_{\Delta t_p} V_i(t-\tau) \cdot I_i(t) dt \tag{4.42}$$

We need to point out here that voltage and current were affected by a spurious delay (τ), resulting from multiple factors: the compensation circuit of the high voltage probe, the spacing between the voltage and current probes, and the length of the cables. A calibration was done to account for τ in the calculations, which

has already been reported in the thesis of Montesano [140]. For the sake of completeness, the calculations are given in appendix A.

From the calculation of the average pulse energy, the average power dissipated by the discharge can be retrieved:

$$P\,[W] = \frac{E_p\,[mJ]}{\Delta t_p\,[\mu s]} \tag{4.43}$$

And finally it is used to determine the Specific Energy Input, as:

$$\begin{aligned} SEI\left[\frac{kJ}{dm^3}\right] &= \frac{P}{\Phi^{in}_{CH_4+CO_2}}\frac{[kW]}{[L/s]} \\ &= \frac{E_p \cdot f_p}{\Phi^{in}_{CH_4+CO_2}}\frac{[kJ \cdot Hz]}{[L/s]} \end{aligned} \tag{4.44}$$

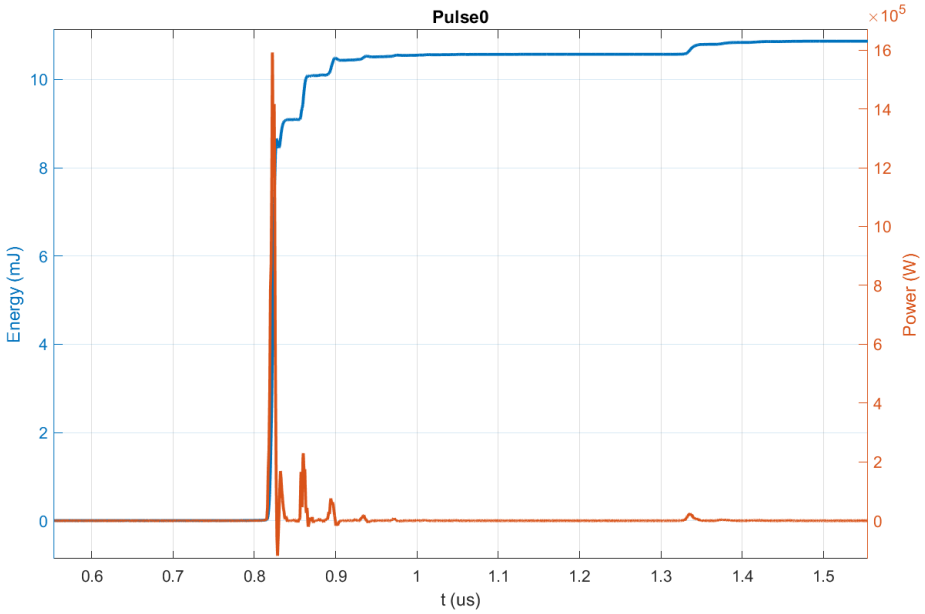

Figure 4.7. Instantaneous energy of the pulse $E_p(t)$ - blue signal - and power P(t) - red signal. Single pulse of the NRP discharge. Pulsing frequency: 450 Hz, inter-electrode gap: 5 mm, gas mixture of CO_2 and CH_4 in a 1:1 ratio, Total flux: 300 sccm.

Chapter 5

Catalyst coupling post-discharge

5.1 Introduction

This chapter examines the performance of Ni-based catalysts in dry reforming of methane (DRM) using a nanosecond pulsed discharge plasma reactor. Two types of catalysts are investigated: Ni-based hydrotalcite-derived catalysts (referred to as NiHT) and Ni/Al_2O_3 catalysts, with Ni loadings ranging from 5 wt% to 40 wt%. These materials were synthesised at AGH University in Krakow and tested in plasma-catalytic experiments at the University of Trento.

The selection of these catalysts was based on prior research of the scientific literature, as highlighted in chapter 1. Hydrotalcite-derived catalysts were chosen due to their favourable properties and demonstrated efficacy in thermal DRM reactions [1, 44]. Ni/Al_2O_3 catalysts were selected for their ease of synthesis, low cost, and well-documented performance in both thermal and plasma-catalysis [141, 142, 69], particularly in dielectric barrier discharge (DBD) plasma configurations.

The primary aim of this study was to assess whether incorporating these catalysts in a post-plasma configuration could enhance reactants conversion and modify product selectivities compared to plasma-only DRM. The key focus was on evaluating if the catalyst presence produced detectable effects on the reaction outcomes.

It is important to note that this research project, initiated in early 2020, faced significant disruptions due to the global COVID-19 pandemic and subsequent lockdowns. These unprecedented circumstances necessitated adaptations to the original research plan. Catalyst synthesis and characterisation, which began in early 2020, experienced prolonged periods of inactivity. Consequently, plasma-catalytic DRM tests started before a comprehensive understanding of all catalysts' properties could be established. This context clarifies why the *40NiHT* sample was selected for plasma-catalytic tests, despite not demonstrating the most promising profile among the synthesised catalysts.

The chapter provides an overview of the catalyst preparation methods (sections 5.2 and 5.3), characterisation techniques (section 5.4), experimental setup (section 5.5), and plasma-catalytic DRM data analysis (section 5.6). Multiple characterisation methods were employed, including X-ray diffraction (XRD), Fourier-transform infrared spectroscopy (FTIR), temperature programmed desorption of CO_2 (CO_2-TPD), N_2 adsorption for BET and BJH analyses, and hydrogen temperature programmed reduction (H_2-TPR).

XRD served as the primary investigative tool throughout the study, because of its availability in both research facilities, and its importance in the characterisation of heterogeneous catalysts.

The experimental setup for plasma-catalytic DRM is described, including the challenges encountered in designing an appropriate post-plasma catalyst configuration for the nanosecond pulsed discharge integration with powder catalysts. The chapter outlines the reaction conditions, analytical methods, and the approach used to calculate key performance metrics like conversion and selectivity.

5.2 Preparation of Ni/Mg/Al mixed oxides catalysts

5.2.1 Co-precipitation of hydrotalcite-derived catalysts

The synthesis of the hydrotalcite-derived catalysts was achieved through co-precipitation. Co-precipitation is a widely used technique for the preparation of heterogeneous powder catalysts, and is particularly suitable for hydrotalcite clays [143]. It involves the simultaneous precipitation of two or more components from a solution, resulting in a homogeneous mixture at the molecular level. The desired metal precursors are mixed from their aqueous solutions. A precipitating agent, typically a base such as sodium hydroxide or ammonium hydroxide, is added to induce the formation of insoluble metal hydroxides or carbonates. The pH, temperature, and concentration of the solutions are carefully monitored to ensure uniform precipitation. The resulting precipitate is filtered, washed to remove any residual ions, and then dried. Subsequently, the powder undergoes calcination at elevated temperatures to decompose the hydroxides or carbonates into metal oxides. This step also promotes the formation of the desired crystal structure and enhances the surface area of the catalyst [144].

Co-precipitation offers several advantages. It allows for precise control over the composition and stoichiometry of multi-component catalysts. The method also produces materials with high surface areas and good dispersion of active components, which are crucial for catalytic activity. However, the process can be sensitive to preparation conditions, potentially leading to variations in catalyst properties. Additionally, the method may not be suitable for all metal combinations due to differences in solubility and precipitation rates.

Hydrotalcite clays are typically prepared by co-precipitating divalent (M^{2+}) and trivalent (M^{3+}) metal cations in an alkaline medium. The general formula for hydrotalcites is:

$$[M^{2+}_{1-x}M^{3+}_{x}(OH)_2]^{x+}[A^{n-}]_{x/n} \cdot m\, H_2O$$

where M^{2+} is often Mg^{2+} and M^{3+} is often Al^{3+}, although other cations may be used.

This method allows for precise control over the M^{2+}/M^{3+} ratio, which significantly influences the properties of the resulting hydrotalcite. The co-precipitation technique ensures a homogeneous distribution of cations within the layered structure, crucial for the catalytic properties of these materials.

The following preparation procedure was applied three times with different molar fractions to obtain different Ni concentrations of 5, 10 and 40 wt.% of the final catalysts. A picture of the synthesis setup is shown in figure 5.1.

Figure 5.1. Co-precipitation setup for the synthesis of hydrotalcite-like catalysts with nichel. The solution is kept at a constant temperature of 50°C and stirred continuously with a magnetic stirrer. The precursor metals solution (green due to the nickel salt) and alkaline solution are poured dropwise and pH is monitored with a pH meter.

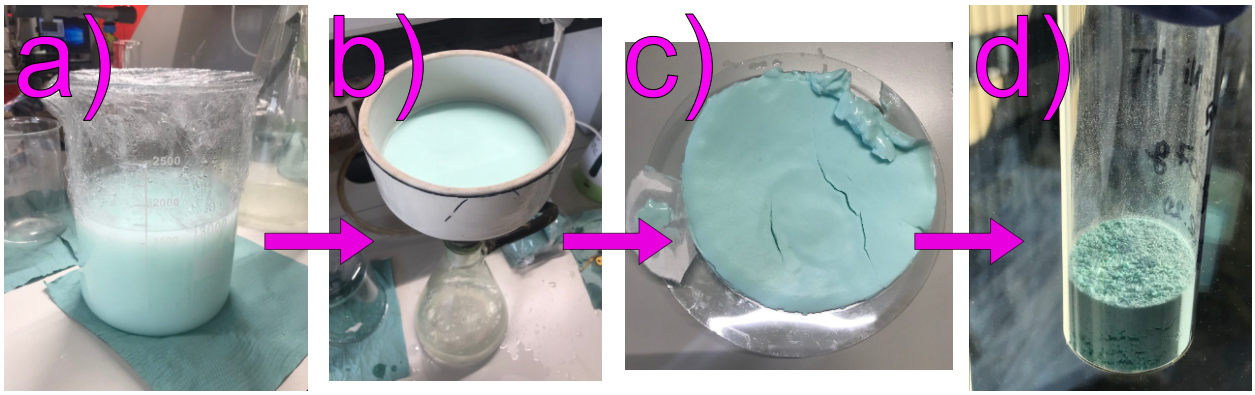

Figure 5.2. Co-precipitation stages for the synthesis of hydrotalcite-like catalysts with nichel. a) The aged co-precipitated solution. b) filtering under reduced pressure and washing. c) the resulting slurry before drying d) the grounded Ni/Mg/Al powder catalyst.

First, an aqueous solution of the metal precursors nickel nitrate ($Ni(NO_3)_2 \cdot 6\,H_2O$, Acros Organics, CAS: 13478-00-7), aluminum nitrate ($Al(NO_3)_3 \cdot 9\,H_2O$, Poch S.a., CAS: 7784-27-2) and magnesium nitrate ($Mg(NO_3)_2 \cdot 6\,H_2O$, Eurochem BGD Sp., CAS: 13446-18-9) was prepared. An alkaline 1M solution of the precipitating agent sodium hydroxide ($NaOH$, Poch S.a., CAS: 1310-73-2) was prepared separately. Then, a sodium carbonate solution (Na_2CO_3, Poch S.a., CAS: 497-19-8) was also prepared, which was heated at a constant temperature of (50 ± 2)°C and stirred vigorously on a magnetic stirrer.

The metal precursors and alkaline solutions were added dropwise to the sodium carbonate solution. The drop rates were adjusted manually, so that the global pH remained constant at (10.0 ± 0.5). The solution obtained was aged at 50°C for 1 hour, filtered under reduced pressure and washed thoroughly with deionized water to remove excess ions. The resulting slurry was dried overnight at 80°C. Finally, the dried hydrotalcite material was ground into a fine powder.

5.2.2 Calcination and activation

The hydrotalcite-like powders were calcined to yield homogeneous nano-sized mixed metal oxides with periclase-like structure. The samples were heated from ambient temperature to 550°C at 10°C / min with an air flow of 10 sccm. The temperature was kept at 550°C for 4 hours, followed by natural cooling to ambient conditions.

Before each reaction in Trento, the catalyst sample was activated by reduction in a tubular silica furnace (Nabertherm, RSH 50/300/13). After conditioning the furnace atmosphere for 1 h with 1L/min N_2 flow, a flow of 5% H_2 in Ar of 100 sccm was established. The temperature was raised from ambient conditions to 900°C after a heating ramp of 10°C/min and kept at 900°C for 1 h. The cool down was performed under the same H_2/Ar flow.

5.3 Preparation of Ni/Al_2O_3 catalysts

The Incipient Wetness Impregnation (IWI) method was employed to prepare three samples: 5, 10 and 40 wt% Ni/Al_2O_3.

For each nickel loading, 15 g of commercial γ-alumina powder (CAS 1344-28-1) were impregnated. The measured γ-Al_2O_3 sorption capacity was determined to be 0.8 $cm^3(H_2O)/g$. A solution was prepared for each nickel loading by dissolving nickel nitrate ($Ni(NO_3)_2 \cdot 6\,H_2O$, Acros Organics, CAS: 13478-00-7) in deionized water. The quantity of nickel nitrate in the solution was calculated to yield the desired loadings of 5, 10 and 40 wt%. The impregnation process involved pipetting 12 cm^3 of the prepared solution onto the alumina powder. Subsequently, the material was dried overnight in air at 80°C. The dried materials were calcined in air at 550°C for 4 h.

Two additional samples were prepared by the adsorption method: 5 and 10 wt% Ni/Al_2O_3. It is noted that the adsorption method's limitation precluded higher metal loadings. Commercial γ-alumina powder (CAS 1344-28-1) served as a substrate.

5.4 Catalyst characterization

5.4.1 FTIR

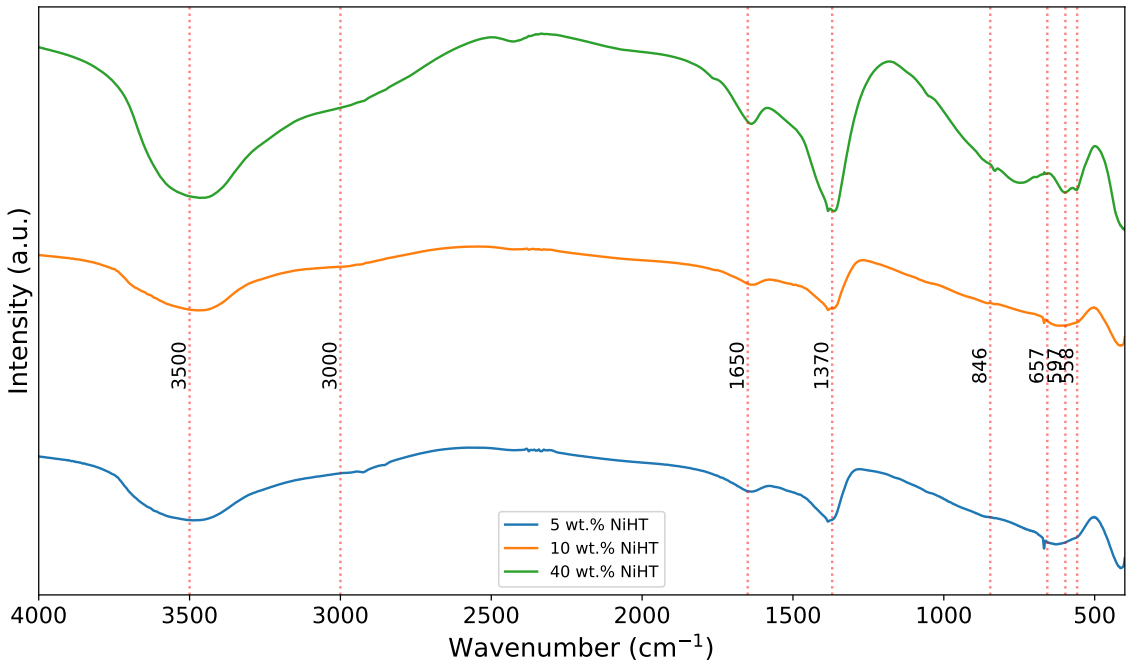

Figure 5.3. DRIFT spectra of the fresh Ni-hydrotalcite clays before calcination. The dotted vertical lines mark the adsorption IR bands associated with the material. From top to bottom are stacked the spectra of 40 wt.% Ni-HT, 10 wt.% Ni-HT and 5 wt.% Ni-HT.

Figure 5.3 shows the Diffuse Reflectance Infrared Fourier Transform spectra of freshly synthesised hydrotalcite-like catalysts with 5, 10 and 40 wt.% of Ni introduction in the brucite layers. The analysis was only conducted on these samples, prior to calcination, to confirm their correct synthesis and to verify the composition of the interlayer anions.

All spectra present a broad adsorption band around 3500 cm^{-1}, attributed to the stretching vibrations of the hydroxyl groups (OH) in the brucite-like layers. A shoulder at about 3000 cm^{-1} is representative of the CO_3^{2-} – H_2O hydrogen bond between water molecules and inter-layer carbonate anions [145]. Another H_2O bending vibration is present around 1650 cm^{-1}. This is visible in all spectra and is associated with the water content in the interlayer [143]. After that, we notice the adsorption peaks around 1370 cm^{-1}, which are attributed to the two symmetric stretch (ν_3) modes of the interlayer carbonate anion [143, 145].

In the low frequency region of the spectra (low wavenumbers) we follow the band assignment done by Kloprogge and Frost [145]. Here, the bands at 597 cm^{-1} are ascribed to hydroxyl translation modes, influenced by Ni in the hydrotalcite structure. The bands around 850 cm^{-1} and 660 cm^{-1} are attributed to the ν_4 and ν_2 modes of the interlayer carbonate anion.

5.4.2 N_2-adsorption

The low-temperature N_2 adsorption results are reported in table 5.1.

The Specific Surface Area (SSA) values, determined by the BET method, varied significantly across the samples. The Ni-HT calc series exhibited relatively low SSA values, ranging from 11 to 47 m^2/g, with SSA increasing as Ni content increased. In contrast, the Ni/Al_2O_3 series showed markedly higher SSA values, ranging from 84 to 115 m^2/g, indicating a more developed porous structure.

Pore volumes, as determined by both BJH and DFT methods, generally correlated with SSA values. The Ni-HT calc series showed lower pore volumes compared to the Ni/Al_2O_3 series, consistent with their lower SSA values. Interestingly, the pore volumes calculated by DFT were consistently lower than those obtained by BJH, suggesting some differences in pore structure assessment between these methods.

Micropore analysis revealed negligible microporosity in the Ni-HT calc series. In contrast, the Ni/Al_2O_3 series showed some degree of microporosity, particularly notable in the 10 Ni/Al_2O_3 ads calc sample, which exhibited a significant micropore surface area of 115.34 m^2/g.

Mean pore diameters varied across the samples, with the Ni-HT calc series showing generally larger pores (11.58-23.13 nm) compared to the Ni/Al_2O_3 series (6.78-10.34 nm). This difference suggests distinct pore structures between the two series, potentially influencing their catalytic properties.

These textural properties indicate that the preparation method and Ni content significantly influence the porous structure of the catalysts, which may, in turn, affect their catalytic performance.

Table 5.1. Physical properties of the prepared samples

Sample	SSA BET [m^2/g]	Pore Volume BJH [ml/g]	Pore Volume DFT [ml/g]	Pore Volume micropores [ml/g]	Surface Area micropores [m^2/g]	Mean pore diameter [Å]
5 wt.% Ni-HT calc	11.2	0.08	0.06	0	0	23.13
10 wt.% Ni-HT calc	22.6	0.13	0.10	0	0	19.57
40 wt.% Ni-HT calc	47.3	0.14	0.13	0	0	11.58
5 wt.% Ni/Al_2O_3 ads calc	105	0.27	0.24	0	0	9.93
5 wt.% Ni/Al_2O_3 iwi calc	94	0.25	0.21	0.0013	3.20	10.22

Continued on next page

Table 5.1 continued from previous page

Sample	SSA BET [m^2/g]	Pore Volume BJH [ml/g]	Pore Volume DFT [ml/g]	Pore Volume micropores [ml/g]	Surface Area micropores [m^2/g]	Mean pore diameter [nm]
10 wt.% Ni/Al_2O_3 ads calc	115	0.24	0.27	0.041	115.34	6.78
10 wt.% Ni/Al_2O_3 iwi calc	84	0.23	0.19	0.0009	2.40	10.34
40 wt.% Ni/Al_2O_3 ads calc	87	0.22	0.19	0.0017	3.80	9.75

5.4.3 CO_2-TPD

The recorded CO_2-TPD profiles of the powder catalysts are included in Fig. 5.4, and the quantitative results are shown in table 5.2. After deconvolution of the peaks in the TPD profiles, the position of the component peak maxima and their surface areas were used to determine the concentration of alkaline centers. These were conventionally divided into three main categories, based on the strenght of the alkaline adsorption bond, following Zhong et al. [146]:

- weak (50 - 150 °C),
- medium (150 - 240 °C),
- strong (>240 °C).

The total basicity of the surface of the samples was also determined.

Table 5.2. Quantitative analysis of surface alkaline centers and their distribution. The percentage of specific basic centers relative to total basicity are given in parentheses.

Catalysts	Weak base centers ($\mu mol/g_{cat}$)	Medium base centers ($\mu mol/g_{cat}$)	Strong base centers ($\mu mol/g_{cat}$)	Tot_{ads}	Basicity ($\mu mol/g_{cat}$)
5 wt.% NiHT calc	18.3 (33.3)	17.5 (31.9)	19.1 (34.8)	1.08	54.9

Continued on next page

Table 5.2 continued from previous page

Catalysts	Weak base centers (μmol/g_{cat})	Medium base centers (μmol/g_{cat})	Strong base centers (μmol/g_{cat})	Tot_{ads}	Basicity (μmol/g_{cat})
10 wt.% NiHT calc	25.4 (24.2)	42.6 (37.6)	43.3 (38.2)	1.02	111.3
40 wt.% NiHT calc	13.7 (10.6)	33.2 (25.6)	82.9 (63.8)	0.98	129.8
5 wt.% Ni/Al_2O_3 ads calc	40.0 (74.9)	-	13.4 (25.1)	1.09	53.4
10 wt.% Ni/Al_2O_3 ads calc	37.9 (64.0)	12.9 (21.8)	8.4 (14.2)	1.03	59.2
40 wt.% Ni/Al_2O_3 ads calc	19.8 (40.2)	15.1 (30.7)	14.3 (29.1)	1.04	49.2
5 wt.% Ni/Al_2O_3 iwi calc	24.4 (40.3)	19.5 (32.2)	16.7 (27.5)	1.08	60.6
10 wt.% Ni/Al_2O_3 iwi calc	26.0 (45.4)	21.7 (37.9)	9.6 (16.7)	1.07	57.3

In hydrotalcite-derived calcined samples, the total basicity per unit mass increased with Ni content. The weak base centers percentage relative to total basicity increased in inverse proportion to the Ni content, starting from 11% of the 40NiHT sample to a maximum of 33% of the 5NiHT sample. Medium base centers registered the largest percentage presence in the 10NiHT sample (38%). Strong base centers constituted a consistent presence in all the hydrotalcite-derived samples, but they registered a cospicuous presence in the 40NiHT sample, with 64% of basic sites.

As for Ni/Al_2O_3 samples, the ones obtained through adsorption method and calcined exhibited higher total basicity in the 10 wt.% Ni/Al_2O_3 sample. Weak basic sites made up the largest fraction among the three categories of basic sites, comprised in a range between 75% and 40%, decreasing with Ni content. Medium sites percentage increased with Ni content, whereas strong sites percentage was lowest in the 10 wt.% Ni/Al_2O_3 sample and highest in the 40 wt.% Ni/Al_2O_3 sample.

The calcined Ni/Al_2O_3 materials obtained through incipient wetness impregnation had comparable values of total basicity and of their distribution among the three categories.

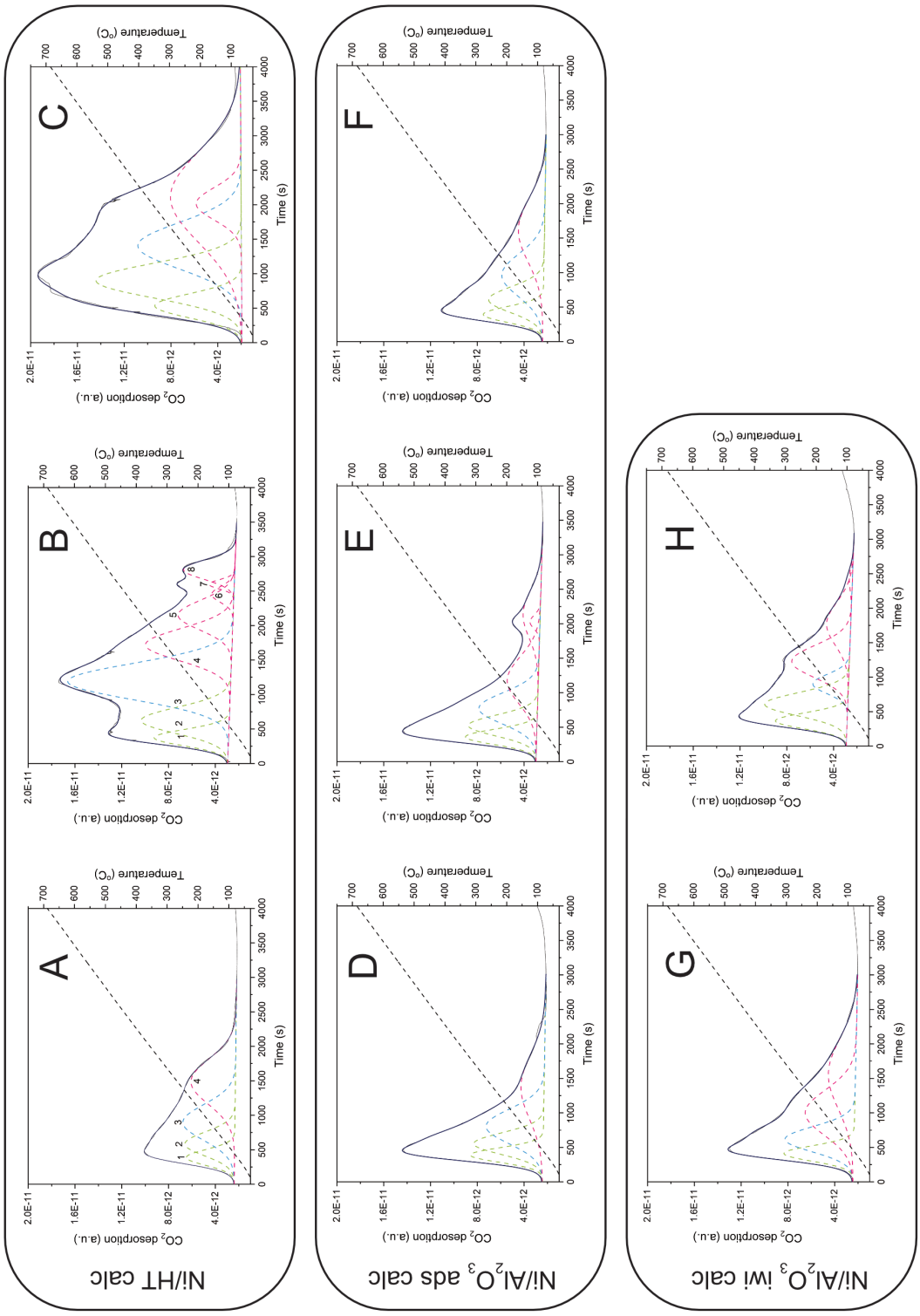

Figure 5.4. CO_2-TPD profiles of the powder catalysts. CO_2 desorption is shown as a function of time and temperature. The peaks corresponding to weak sites are green, the medium site ones blue, and the strong ones are pink. A - 5 wt.% Ni/HT calc, B - 10 wt.% Ni/HT calc, C - 40 wt.% Ni/HT calc, D - 5 wt.% Ni/Al_2O_3 ads calc, E - 10 wt.% Ni/Al_2O_3 ads calc, F - 40 wt.% Ni/Al_2O_3 ads calc, G - 5 wt.% Ni/Al_2O_3 iwi calc, H - 10 wt.% Ni/Al_2O_3 iwi calc.

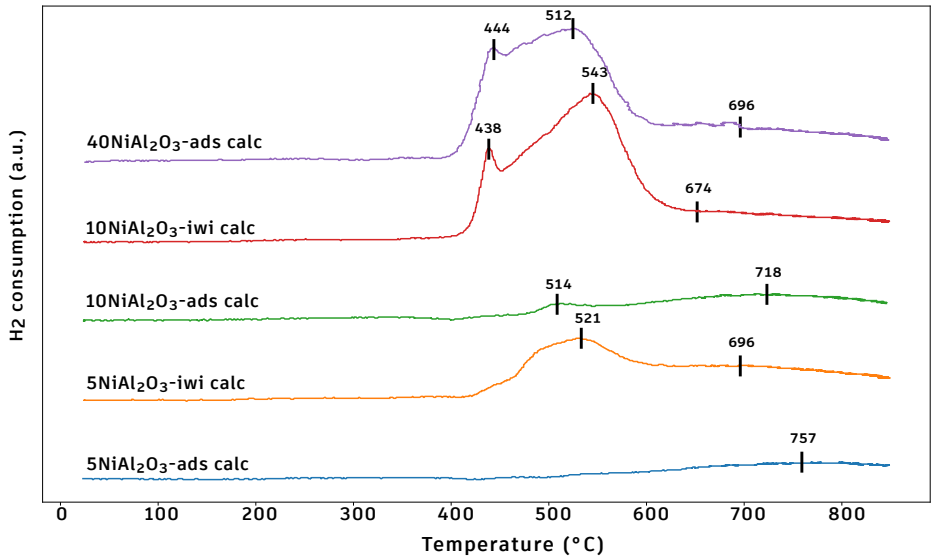

Figure 5.5. H_2-TPD profiles of calcined Ni/Al_2O_3 catalysts.

5.4.4 H_2-TPR

Temperature programmed reduction in H_2 curves are shown in figure 5.5 for calcined Ni/Al_2O_3 samples obtained by Incipient Wetness Impregnation (IWI) and adsorption preparation techniques. A first distinction is noted between samples with the same Ni loading, but obtained with different techniques. In fact, the IWI ones show a more intense signal compared to the catalysts prepared by adsorption for the same Ni loading.The samples ranging from 5 wt.% to 10 wt.% Ni all show a broad H_2 adsorption peak centered around 700-760°C, attributed to $NiAl_2O_4$ reduction. This peak shifts toward lower temperature with increasing Ni loading. Together with it, these catalysts also show a narrower peak around 515-520 °C, which becomes more intense with Ni loading in the adsorption-prepared catalysts and is very clear in the 5 $NiAl_2O_3$-iwi_calc sample. This peak is usually attributed to the reduction of NiO particles that have a higher interaction with the support [147]. Finally, catalysts 10 $NiAl_2O_3$-iwi_calc and 40 $NiAl_2O_3$-ads_calc show a similar reduction curve, where the main H_2 adsorption is located around two peaks about 440 and 530°C, where NiO is reduced. The lower temperature peak is associated with dispersed NiO particles that interact weakly with the support , while the higher temperature peak is attributed to NiO particles with moderately strong interaction with the support [148].

The reduction profiles for Ni/Mg/Al mixed oxides are shown in figure 5.6. A broad asymmetric peak in the range of relatively high temperatures (>640 °C)is present in all the samples, with the center of the peak shifting from a maximum of 800°C (5NiHT calc sample) to lower temperatures at increasing Ni loading. This peak indicates reduced Ni strongly interacting with the support, which is associated to the formation of a NiO-MgO solid solution in hydrotalcite-derived Ni/Mg/Al mixed oxides [1]. The shifting towards lower temperatures is explained by the greater availability of Ni-O-Ni oxides compared to Ni-O-Mg oxides, where Ni^{2+} cannot be reduced [44]. In the 40NiHT sample another isolated and intense peak at 420°C is observed. This peak is attributed to the reduction of surface NiO, that may point out the presence of free bulk NiO species[1].

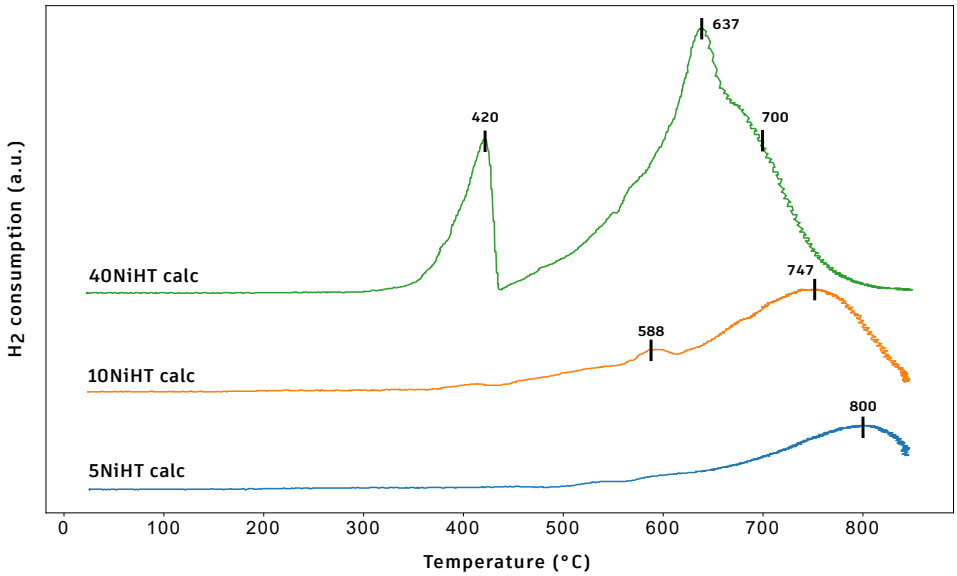

Figure 5.6. H_2-TPD profiles of calcined Ni/Mg/Al mixed oxides catalysts.

5.4.5 XRD

The XRD diffractograms of the fresh Ni-hydrotalcites are shown in figure 5.7. The X-rays reflections are present at $2\vartheta \simeq 11.5$, 23.5, and 35°. They are associated with the diffraction pattern of a hexagonal lattice with 3R*m* rhomboedral symmetry, typical of layered structure of magnesium aluminium hydroxide hydrate (hydrotalcites) (ICOD 00-014-0191). The reflections are associated with lattice planes (003), (006), (009), (110) and (113) [149, 143]. No additional phases relative to Ni were observed, indicating the successful incorporation of nickel cations into the brucite-like layers.

The XRD patterns of calcined hydrotalcite-derived catalysts are shown in figure 5.8. They exhibited two main reflections at $2\vartheta \simeq 36$, 43,5 and 63°, which are assigned to the (111), (200) and (220) reflections of the periclase-like structure of MgO in mixed oxides (ICOD 00-045-0946) and to NiO [149]. The other notable reflections are located at $2\vartheta \simeq 75$ and 79 °and are attributed only to NiO in the periclase-like structure. Their intensities increase with Ni loading in the synthesised materials. They show good Ni integration and the successful thermal decomposition of the hydrotalcite precursors into the mixed oxides periclase structure. Reflections attributed to the spinel phase $NiAl_2O_4$, which is an inactive phase in DRM, were not found.

For the diffractometric analysis of reduced samples, we focus here on the main sample that was tested in the plasma-catalytic dry reforming experiments, and we report its post-mortem results in the dedicated section (5.7).

Because reduction of the catalyst had to be performed *ex-situ* from the reactor, a study was conducted to monitor its re-oxidation upon air exposure. Consecutive XRD diffraction patterns were acquired on the same 40 wt.% Ni-HT sample after its calcination and reduction every 6 hours, reaching a maximum of 18 hours. The study is shown in figure 5.9. The catalyst showed an optimal resistance to re-oxidation up until the time limit imposed, as all the diffractograms show the same features in terms of diffraction patterns, peak widths and intensities.

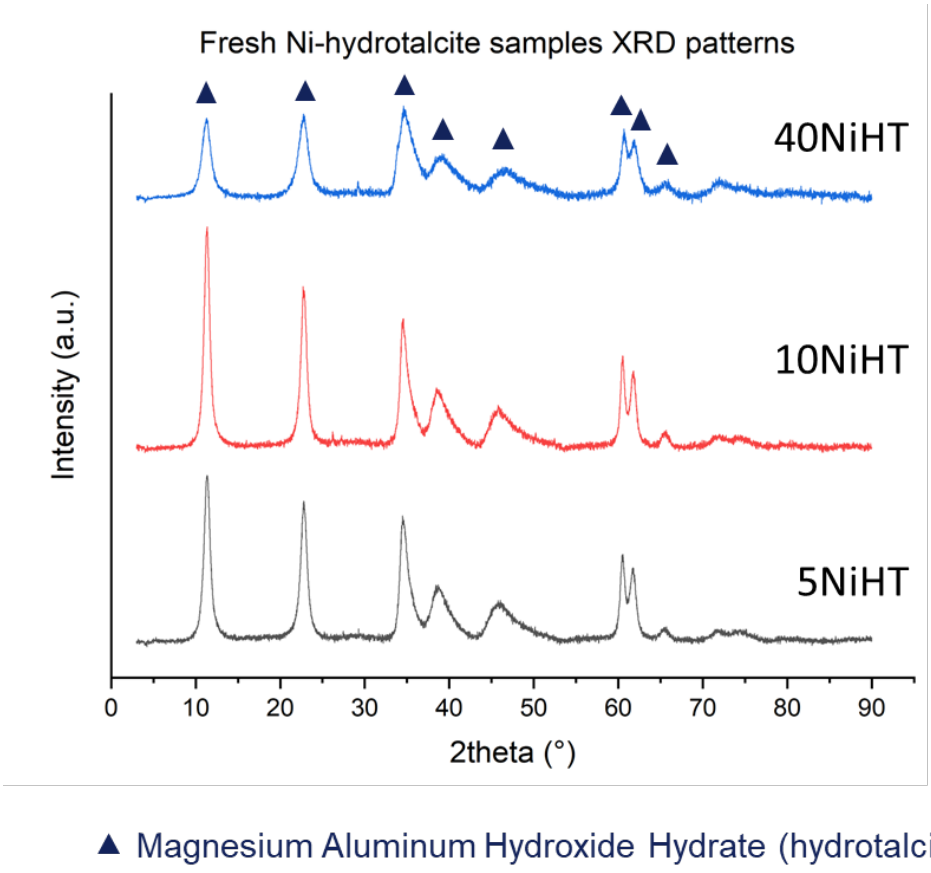

Figure 5.7. XRD diffractograms of the Ni-based hydrotalcite-derived catalysts before calcination.

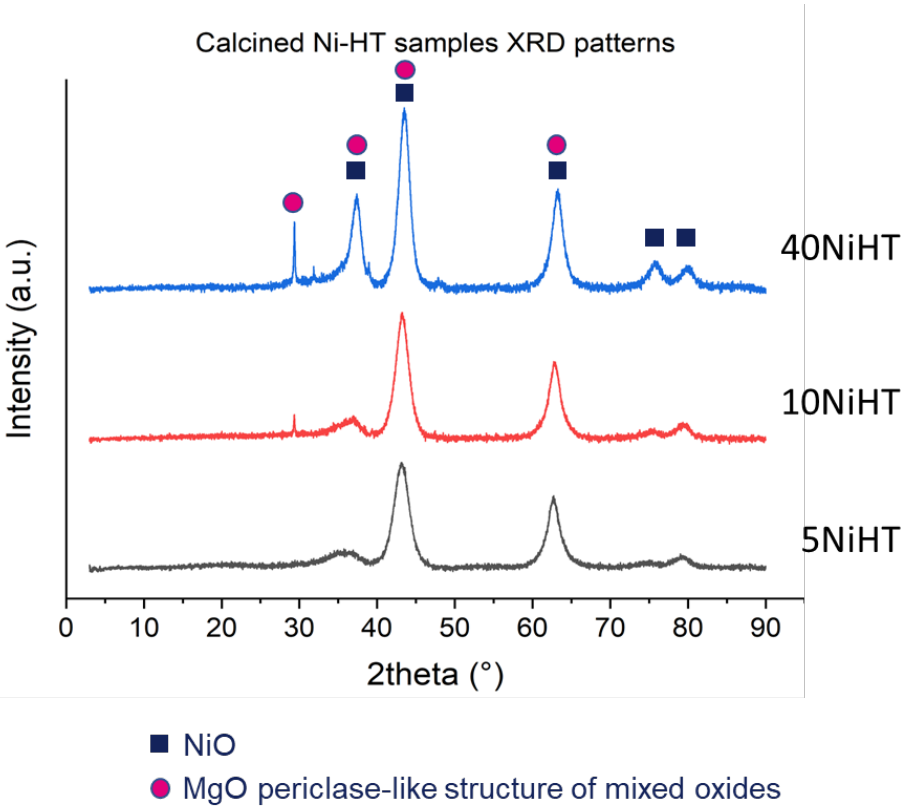

Figure 5.8. XRD diffractograms of the Ni/Mg/Al mixed oxides after calcination.

The reduced catalyst showed reflections at $2\vartheta \simeq 44$, 51 and 76°, which are characteristic for a cubic metallic nickel structure (ICOD 01-087-0712). However, the Ni^0 crystallite size could not be estimated using Ni^0 reflections and Scherrer equation. On the one hand, the low amount of material used required a manual re-alignment of the positions of the reflections, losing information on possible line shifts. On the other hand, a study on the instrumental line-broadening and instrument calibration has yet to be done. The reflections characteristic of the periclase-like structure of mixed oxides (2ϑ equal to ca. 43 and 63°) are also present.

5.5 Plasma experimental setup

Post-plasma catalysis with a nanosecond pulsed discharge has proven to be a challenge from a reactor design point of view. In classic catalysis, the plug-flow reactor is usually a quartz tube, in which the powder catalyst can be inserted and held in place by two layers of quartz wool. When plasma-catalysis is involved, the most widespread configuration is DBD, where the powder or pellets are packed into the discharge region and delimited by quartz wool [109]. Here, as the catalyst cannot be inserted in direct contact with the NRP discharge, multiple solutions have been adopted and tested. While the results presented in this chapter focus on one particular configuration, we believe it may be helpful to provide a brief overview of the other configurations adopted at the end of this section.

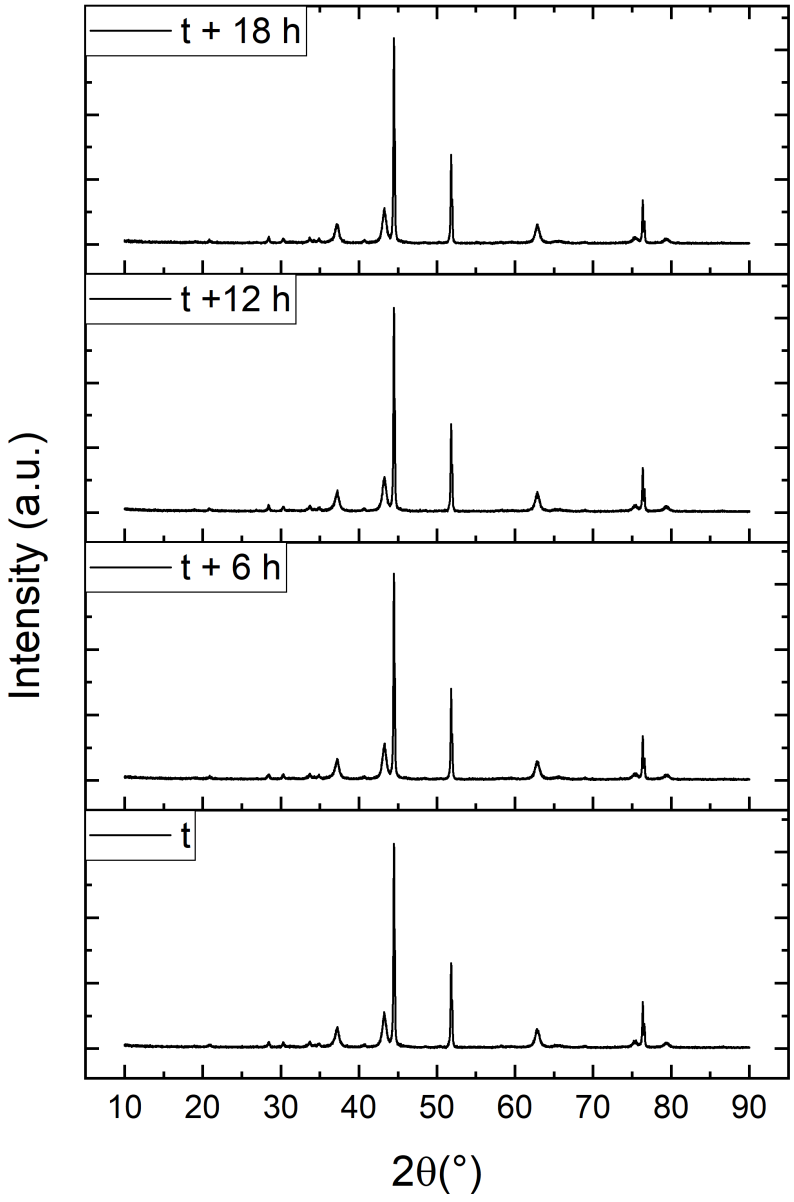

Figure 5.9. Study on re-oxidation of the 40NiHT reduced catalyst in time. XRD diffractograms for the same sample are acquired after its reduction every 6 hours, for a maximum of 18 hours.

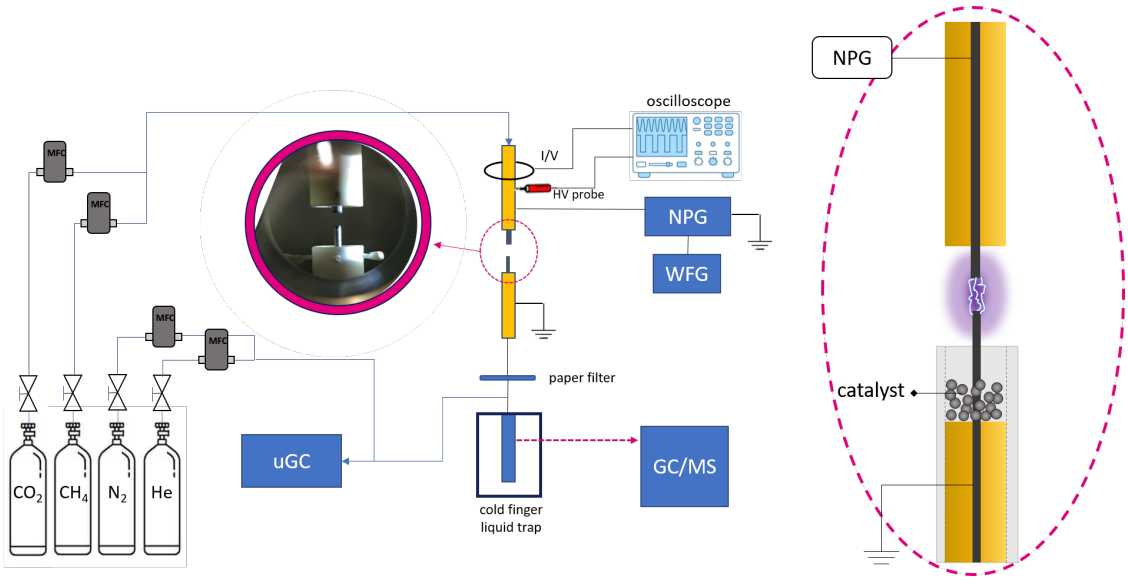

Figure 5.10. Schematic of the plasma-catalytic DRM experimental setup for post-plasma catalysis with powder catalysts. The dotted circle encloses the pin-to-pin electrodes and the catalyst compartment is shown in the section.

The experimental setup schematic of the main configuration is shown in figure 5.10 and it is based on the general setup described in section 4.3. The discharge is operated at atmospheric pressure and the two tungsten electrodes are placed in a pin-to-pin configuration with a distance of (6.5± 0.5) mm. The reactant gas mixture is composed of 75 sccm CO_2 and 75 sccm CH_4. Before entering the μGC analyzer (Agilent 3000A), 300 sccm of N_2 and 7,2 sccm He are added as dilution agent and internal standard, respectively. The ground electrode (cathode) is embedded in a cylindrical MACOR holder, shown in figure 4.2 of section 4.3 and in figure 5.10. The holder is designed to have a crown protruding around the cathode rod, just above the gas outlet channels. This cylindrical slot can host the catalyst powder. Two different catalyst loadings were examined:

- 450 mg (ca. 0.6 mL of volume), for which the results in this chapter are reported, corresponding to a GHSV = 15'789 h^{-1};
- 1100 mg (ca. 1,4 mL of volume), corresponding to a GHSV = 6'429 h^{-1}.

The reduced catalyst was enclosed between two quartz wool layers in the ceramic crown of the cathode holder. Once the reactor was closed, it was first pumped down, then conditioned at atmospheric pressure for 30 min with 500 sccm of N_2 flux. Then, only the reactant gas mixture of CH_4 and CO_2 was flowed in the reactor, and a first chromatographic sequence was run with the discharge off to record the plasma blank measure. After this step, the discharge was turned on at fixed energy and frequency, and the same chromatographic sequence was repeated after the steady-state condition was reached. The measure with discharge on was carried out for one hour. Unfortunately, it was not possible to conduct longer stability tests, as the system suffered from severe coking, which caused the reactor to become obstructed and internal pressure to increase significantly after such a time.

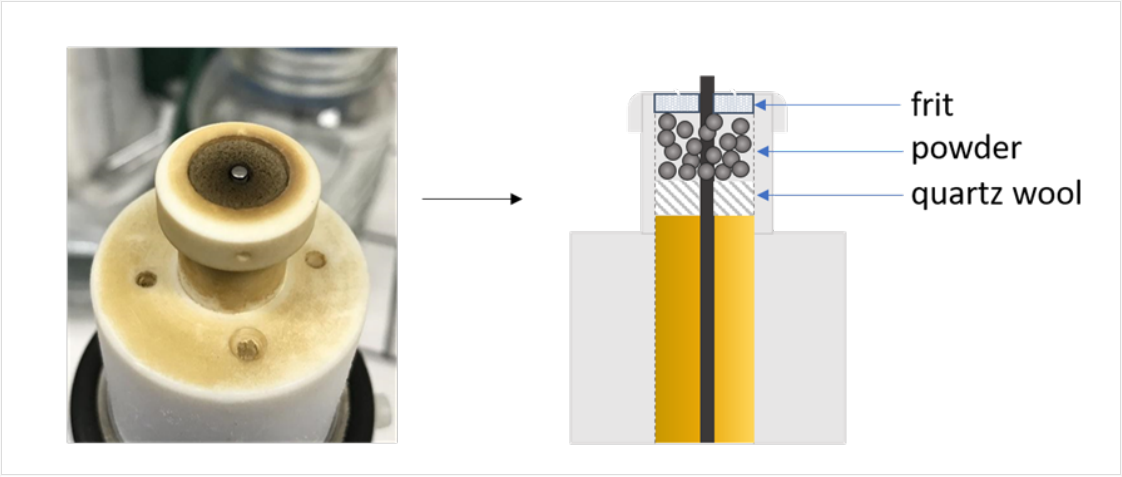

Figure 5.11. Catalyst configuration at the cathode stage with quartz frit integration at the cathode stage. On the left, a picture of the cathode stage is shown after DRM reaction, showing coking on its surface. On the right, a section of the cathode stage is shown in a sketch to illustrate the layering of the frit, catalyst and quartz wool.

The chosen pulsing scheme was a continuous mode, where a single pulse frequency characterises the signal. Different plasma powers were investigated, spanning in the frequency range [450, 1000] Hz, which roughly corresponded to SEIs [2, 6.5] kJ/dm^3.

Another design solution was tested to make sure the catalyst could be at a closer and more precise distance from the discharge. This solution is illustrated in figure 5.11 and involved the use of a porous quartz frit of 1 mm thickness. The commercial frit was drilled in the center to allow the passage of the ground electrode, and it was held in place by an additional ceramic cap. The cap was shaped in such a way that the frit surface remained completely exposed. This solution was later improved to guarantee better accuracy and reliability. The optimized configuration relied on an additional reactor piece, custom made of MACOR, which served as a catalyst vessel (CAD design and picture in the reactor are shown in figure 5.12. The catalyst vessel made it easier to load and unload the catalyst powders, quartz wool and frit. It could also be removed from the reactor to weigh its mass difference before and after the experiment. Despite the advantages stated above, none of these configurations showed a measurable impact on the DRM reaction results.

5.6 DRM results

DRM results are discussed by studying the conversions of CO_2 and CH_4 and the selectivities of the products as a function of Specific Energy Input (SEI). The results of the plasma-catalytic experiments are always shown together with the results obtained with plasma alone, so that a comparison can be drawn and a catalyst effect can be investigated. Every data point in the graphs is representative of one single measure and its error bars account for 1σ of the propagated statistical error.

Figure 5.13 shows the reactants percent conversions as a function SEI of the continuous pulsed discharge with and without the reduced 40NiHT catalyst. The results are reported for a catalyst loading of ca. 450 mg.

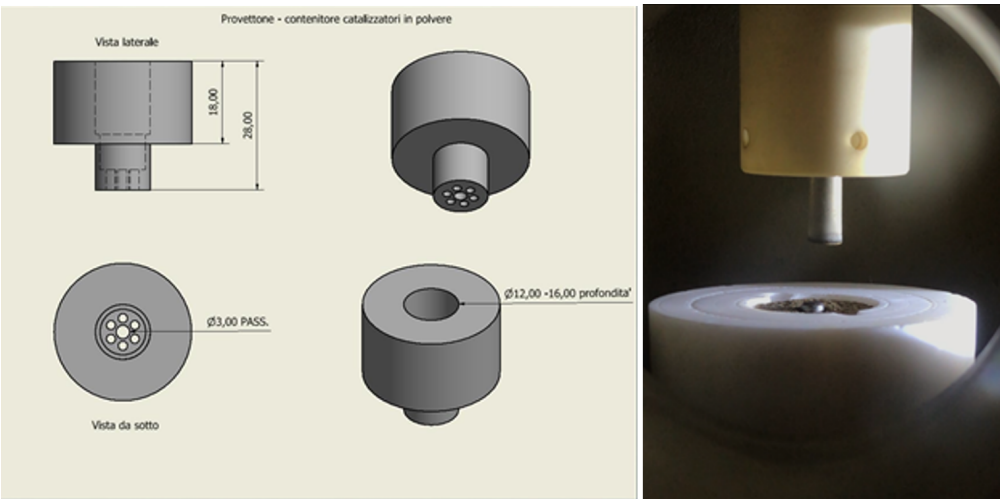

Figure 5.12. On the left, the CAD sketch of the ceramic catalyst vessel. On the right, a picture showing it mounted in the reactor configuration.

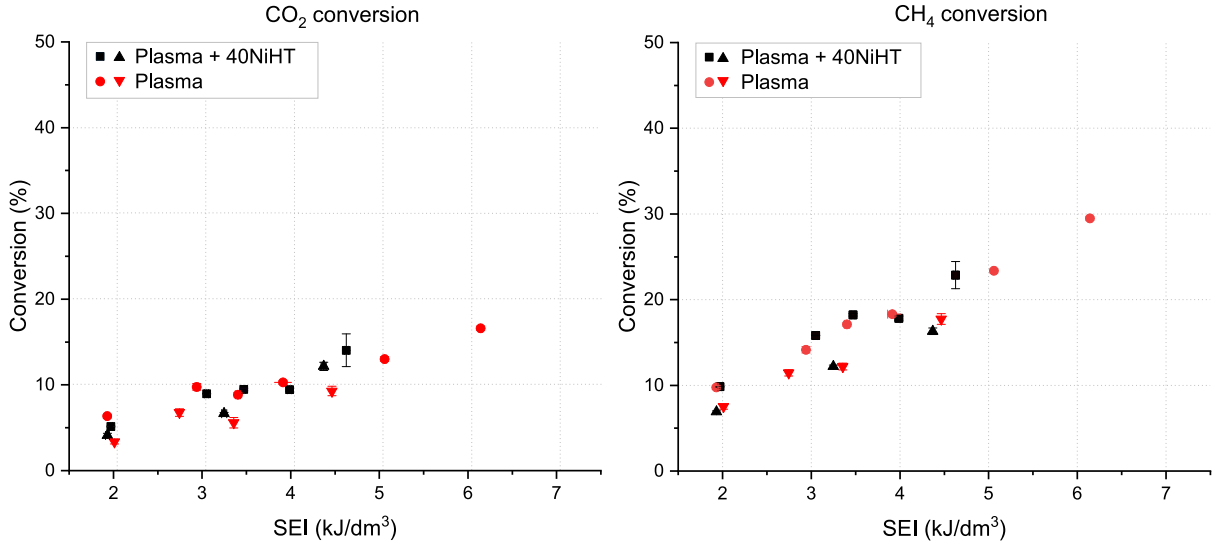

Figure 5.13. On the left, CO_2 conversion as a function of plasma specific energy input (SEI). On the right, CH_4 conversion as a function of SEI.

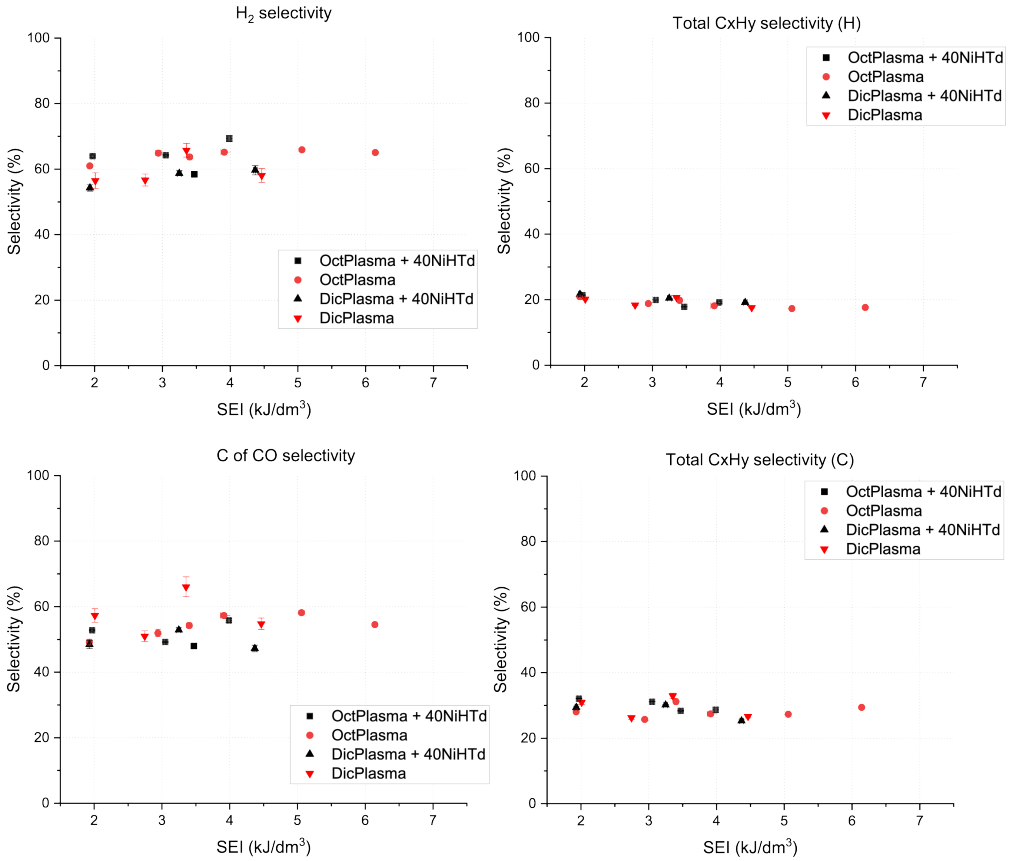

Figure 5.14. Top row: Hydrogen selectivity of the H_2 molecule and for the sum of the detected C2 hydrocarbons (C2H2, C2H4 and C2H6). Bottom row: Carbon selectivity of the CO molecule and for the sum of the detected C2 hydrocarbons (C2H2, C2H4 and C2H6).

Both methane and carbon dioxide conversions increase linearly with the SEI, though with a steeper slope for CH_4 conversion. Unfortunately no apparent distinction between conversions with or without the catalyst is measured. The minimum conversion for CO_2 is about 5% at minimum SEI of ca. 2 kJ/dm^3 for both sets, while a maximum conversion of 14% is measured in the plasma-catalytic setup, at a corresponding SEI of 4.6 kJ/dm^3. The conversion of CH_4 is characterized by about 10% conversion at the lowest SEI, and a maximum value about 23% for the plasma-catalysis configuration at SEI of 4.6 kJ/dm^3.

The minimum SEI value was obtained with a continuous discharge at pulse frequency of 450 Hz. The second reference SEI was obtained with a continuous pulsed discharge at 900 Hz. These results are in line with the ones obtained for plasma alone by Montesano [66] and Scapinello [150].

If we consider the products of reaction, syngas (H_2 and CO) is the main product, accounting for about 85-90% of the total detected products. C2 hydrocarbons (C_2H_2, C_2H_4 and C_2H_6) are the second most abundant category of products, with acetylene being the most abundant (5-6%). Ethylene and ethane are less than 2%, while C3-C4 plus carboxylic acids are detected in traces.

The selectivities of the syngas molecules and the sum of the hydrocarbons group are shown in figure 5.14. They maintain a constant trend to SEI variations, both in the plasma and plasma-catalytic sets. Again, a catalyst's presence does not unequivocally emerge from the datasets comparison, where possible

deviations of the plasma-catalysis selectivities from the plasma-alone one do not seem to follow a trend, but rather be stochastic deviations.

The most abundant hydrocarbon product is C_2H_2 (acetylene), with an average selectivity towards carbon of 15% and towards hydrogen of 5%, as shown in figure 5.15.

Concerning the mass balance and C/H/O lacks, at higher SEIs the balance for a slightly increased mass amount, which is not detected. The strong scattering of the data is caused by the difficulty in detecting such small concentration variations in a highly diluted system as this one. For the same reason, it is also not easy to say whether there are differences between the plasma and plasma-catalytic trends.

5.7 Characterization of the spent catalyst

The XRD patterns recorded for the spent catalysts after 1h DRM reaction at pulse frequencies of 600, 700 and 900 Hz and relative SEIs of 3.3, 3.8 and 4.6 kJ/dm^3 are depicted in figure 5.17. All catalysts exhibited reflections originating from metallic nickel phase (ICOD 01-087- 0712) and Mg(Ni, Al)O nano mixed oxides with periclase like structure (reflections at 2ϑ: 38, 43, 63°; ICOD 01-087-0652).

5.8 Summary

This chapter aimed to investigate the potential enhancement of Dry Reforming of Methane (DRM) using Ni-based powder catalysts in a post-plasma configuration with a Nanosecond Repetitively Pulsed (NRP) discharge. The study involved the synthesis and characterisation of Ni-based hydrotalcite-derived catalysts and Ni/Al_2O_3 catalysts, followed by plasma-catalytic experiments. The catalyst performance was evaluated by comparing the reaction performance parameters in the plasma-alone and plasma-catalytic configurations. The reaction performance was evaluated by measuring reactant conversions and product selectivities as a function of the Specific Energy Input (SEI) using a µGC system.

The results indicated no significant difference in DRM performance between the plasma-alone and plasma-catalytic setups. Both CH_4 and CO_2 conversions increased linearly with SEI, reaching maximum values of approximately 23% and 14% respectively at 4.6 kJ/dm^3. Syngas (H_2 and CO) remained the primary product, accounting for 85-90% of detected products, with C2 hydrocarbons as the second most abundant category. The presence of the catalyst did not measurably alter these trends or the selectivities of other measured products.

The lack of observable catalytic effect can be primarily attributed to the mild conditions in the post-plasma catalysis configuration. The low gas temperature (below 80°C) at the catalyst bed was insufficient to activate thermal catalytic mechanisms. Additionally, the post-plasma setup likely limited the interaction between short-lived plasma species and the catalyst surface, reducing potential synergistic effects. It's worth noting that while comprehensive characterisation data (including BET, H_2-TPR, CO_2-TPD, and XRD) were eventually obtained for the catalysts, the disruptions caused by the COVID-19 pandemic delayed their availability. Consequently, this information could not be used to select the most promising catalyst for the plasma-catalytic experiments. However, even with an optimally chosen catalyst, the mild conditions of the post-plasma configuration would likely have been insufficient for significant catalyst activation.

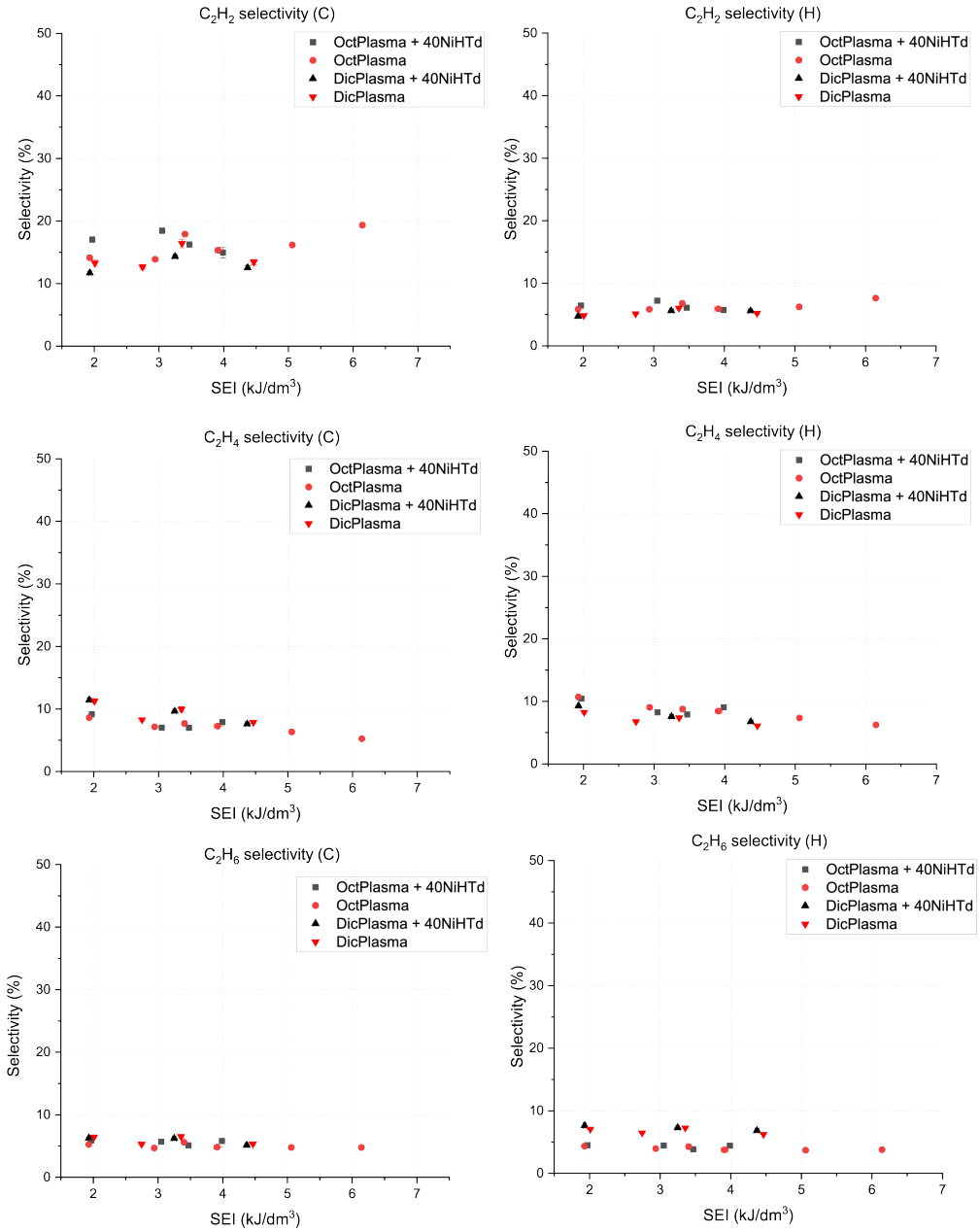

Figure 5.15. C2 hydrocarbons selectivities to carbon (left column) and hydrogen (right column).

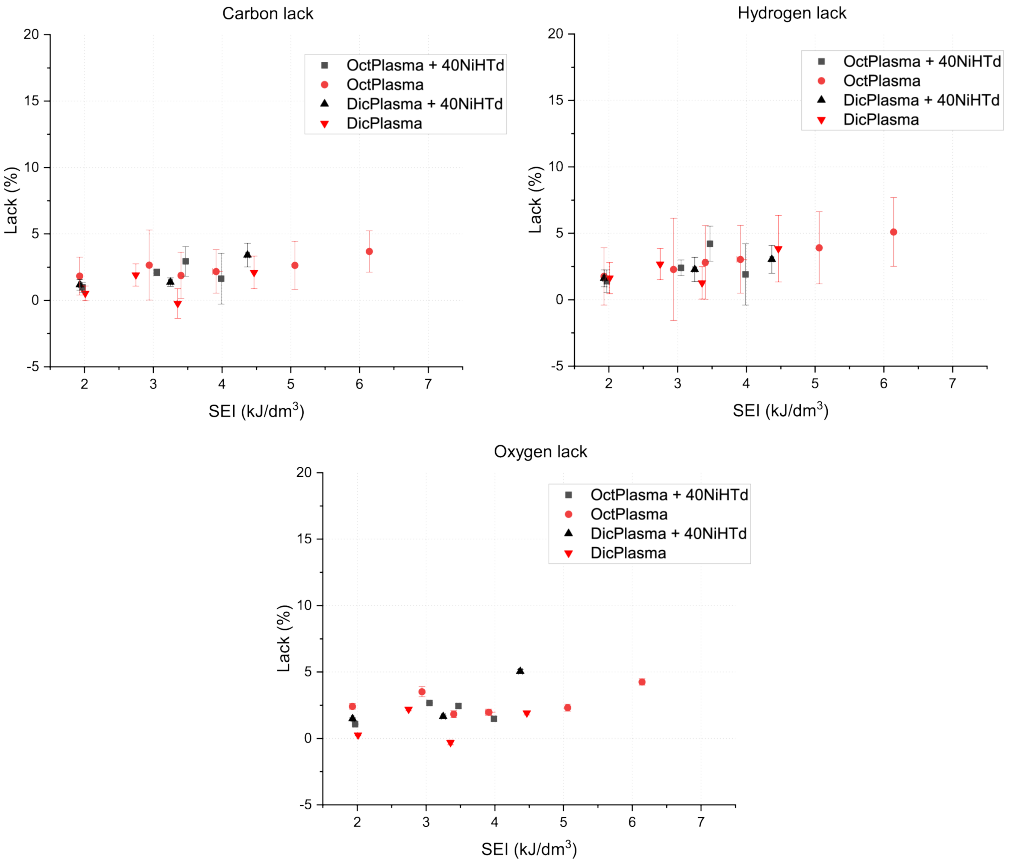

Figure 5.16. Carbon, hydrogen and oxygen lacks as a function of the discharge specific energy input (SEI).

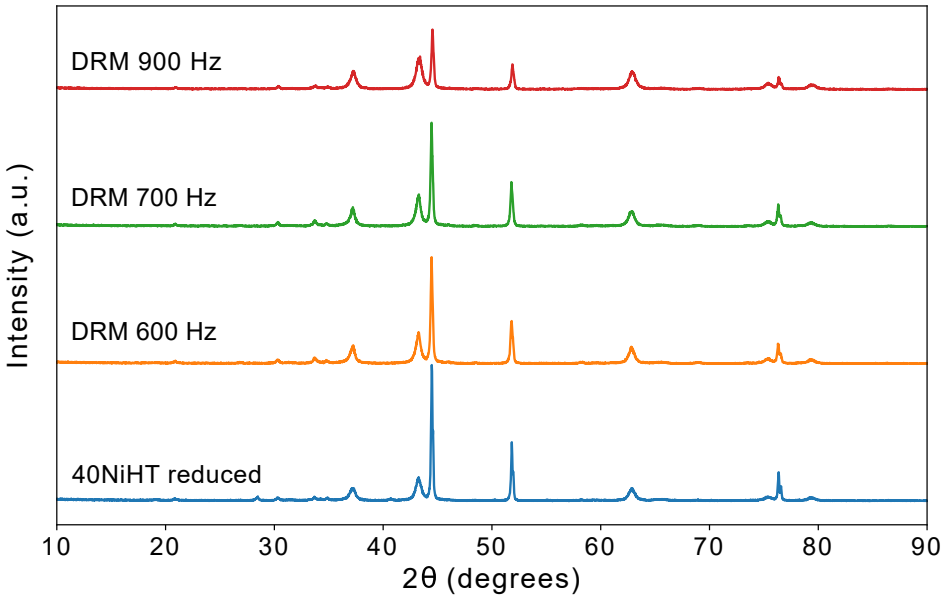

Figure 5.17. Comparison between XRD patterns obtained by 40wt% NiHT (bottom to top): reduced and spent catalyst in DRM at 600Hz, 800Hz and 900Hz pulsed plasma discharge, corresponding to a SEI interval [3.3-4.6] kJ/dm^3.

Future work should focus on exploring alternative plasma-catalyst configurations to enhance interaction between active plasma species and the catalyst surface. This could include a closer catalyst placement to the discharge, in the case of the NRP discharge. This possibility will be explored in the following chapters. Additionally, when possible, comparing the catalyst's performance in conventional thermal catalysis with plasma-catalytic performance could help isolate the impact of the plasma environment. Finally, investigating other catalyst compositions that have shown potential in the performed characterisations may yield more positive results in this specific NRP discharge setup.

Chapter 6

Monolith foam catalyst coupling

6.1 Introduction

There are two phases in the study of monolith foams. The first one focused on the catalyst Ni/Al2O3 obtained from the alumina foam by coating it with gamma alumina and then Ni. These three preparation steps of the final catalysts were tested separately in plasma to verify the contribution of each of them. Then, the confinement effect of the foam surrounding the plasma was investigated with foams of different bulk materials, without any coating. Due to high availability, low cost and relatively good performances with respect to noble metals, Ni-based catalysts are widely considered in thermal and plasma-catalytic DRM. In addition, the nature of the catalytic support is associated with important catalyst properties for the DRM reaction such as metal-support interaction, basicity, oxygen storage capacity, reducibility, porosity and surface area. The common supports used in Ni-based catalysts are metal oxides like Al2O3, La2O3, SiO2, ZrO2, and multi-element porous supports such as zeolites and hydrotalcites. To overcome the issue encountered in previous experiments of powder catalysts too distant from the plasma discharge in a PPC configuration, a Ni/Al2O3 monolith foam catalyst has been synthetized. The monolith is a porous tube that surrounds the discharge from a close distance in a co-axial geometry.

6.2 The foam replica method

The foam replica method, patented by Schwartzwalder and Somers in 1963 [151], is a versatile and widely employed technique for the preparation of ceramic monolith catalysts and catalyst supports [152, 153, 154]. This approach enables the production of highly porous structures with controlled morphology, making it particularly valuable in the field of heterogeneous catalysis. The process begins with the selection of a polyurethane foam template, which serves as a sacrificial scaffold. The choice of template determines the final pore structure of the ceramic foam. Typically, open-cell PU foams with pore sizes ranging from 10 to 100 pores per inch (ppi) are preferred, as these templates are commercially available, cost-effective and offer a wide variety of pore sizes and densities. The next step involves the preparation of a ceramic slurry, which typically consists of ceramic powder, binders, dispersants, and other additives suspended in a liquid solvent, usually water. The composition of the slurry is carefully optimised to ensure proper coating of

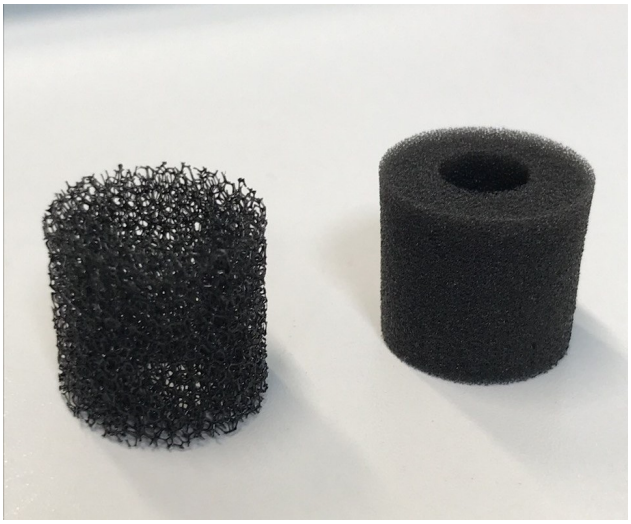

Figure 6.1. PU foams of different pore densities: 30 PPI and 90 PPI.

the PU template and to achieve the desired properties in the final ceramic foam. The PU foam is then impregnated with the ceramic slurry. This is commonly achieved through dip-coating, where the foam is soaked in the slurry. The excess slurry is removed to ensure that only a thin, uniform coating remains on the PU struts. This removal is typically achieved through compression, centrifugation, or the application of air pressure. Following impregnation, the coated foam undergoes a drying process to remove the liquid medium from the slurry. This step requires careful control to prevent cracking or deformation of the coating. Slow, controlled drying is often necessary to maintain the integrity of the structure. Once dried, the coated foam is subjected to a thermal treatment process. This involves two primary stages: pyrolysis and sintering. During pyrolysis, which typically occurs between 300°C and 800°C, the PU template is burned out, leaving behind a ceramic skeleton that replicates the original foam structure. The subsequent sintering stage, conducted at higher temperatures (often above 1000°C), consolidates the ceramic particles and imparts strength to the foam structure. The resulting ceramic foam exhibits a network of interconnected pores, closely mimicking the structure of the original PU template. This high porosity and interconnectivity are advantageous for catalytic applications, as they facilitate mass transfer and provide a large surface area for catalyst deposition.

For catalytic applications, the ceramic foam can be further functionalized by coating it with catalytically active components [155]. This is typically achieved through methods such as impregnation, washcoating, or in-situ synthesis of active phases. The foam replica method offers several advantages for catalyst preparation. It allows for precise control over the pore structure, which can be tailored to specific reaction requirements. The high porosity of the resulting foams enhances mass and heat transfer properties, which are crucial for many catalytic processes. Additionally, the method is versatile and can be applied to a wide range of ceramic materials, including alumina, zirconia, and perovskites. However, the technique also presents certain challenges. The removal of excess slurry and the drying process require careful control to ensure uniformity and prevent defects. Furthermore, the thermal treatment stage can lead to shrinkage and potential cracking of the structure.

6.3 Part I: Study of Ni/Al_2O_3 coated monolith foam catalyst

6.3.1 Ceramic foam synthesis

The structure of the ceramic monolith foam is obtained by the *foam replica method*, as a replica of a polyurethane foam of chosen porosity (90 PPI-pores per inch) and dimensions. The polyurethane (PU) foams (ARE Articoli Resine Espanse – Milano Italy) of 90 pores per inch (PPI) porosity were laser cut into hollow cilynders of 20 mm height, 20 mm ext. diameter and 10 mm int. diameter. A slurry is first obtained mixing α-Al_2O_3 powder, distilled water and a dispersant agent in the proportions reported in table 6.1. Zirconia milling spheres are added to the slurry in a 1:1 weight ratio with the alumina powder and they are mixed in a turbula heavy-duty shaker-mixer for 2 hours. After separation of the milling spheres, the slurry is de-aired for 5 min with a vacuum pump. A binding agent is added in the right proportions (table 6.1) and the final slurry is stirred for 2 hours at 200 rpm velocity.

Table 6.1. Weight percent composition of the alumina slurry used for the foam replica method of α-alumina monolith foams.

Proportion	Component
67.21 wt.%	α-Al_2O_3 (Altamis D50 = 0.5 µm)
25.63 wt.%	distilled water
1.11 wt.%	dispersant agent (Darvan 821 A)
6.06 wt.%	binder (Duramax B1014)

The sponges are plunged in the alumina slurry and squeezed to remove the excess. A weak jet of compressed air is used to open all the pores. This procedure is repeated twice to make sure that the sponge is coated as uniformly as possible. The thermal treatment leading to PU pyrolisis and alumina sintering is carried on in a muffle furnace (Nabertherm, T_{max} = 1600 °C equipped with C42 controller). The temperature is first increased to 400°C with a heating rate of 10°C, then from 400 to 1100°C with a heating rate of 2°C/min. The temperature is kept at 1100 °C for 1:30 h, then it is increased to 1550°C with a heating rate of 0.5°C and kept at 1500°C for another 1:30 h. The cooling down was free.

6.3.2 Surface functionalisation with Ni/Al_2O_3 catalyst

The as-prepared α-Al_2O_3 has a solid and mechanically stable structure, but naturally presents a low surface area. Typically, the Brunauer-Emmett-Teller (BET) surface area of corundum is less than 5 $m^2\ g^{-1}$, with a pore volume below 0.5 $cm^3\ g^{-1}$ [156]. To overcome this issue and increase this parameter, a γ-Al_2O_3 coating is performed on the foam surface, prior to the nickel deposition.

The alpha-alumina surface is first pre-treated with a light chemical etching treatment. This step is performed to improve the adhesion and uniformity of subsequent coatings by increasing the surface roughness. The monoliths are immersed in a 1 M nitric acid solution solution for 30 s and then thoroughly washed with distilled water to remove any residual acid. The rinsed foams are dried in air at 120°C for 2 h. Subsequently,

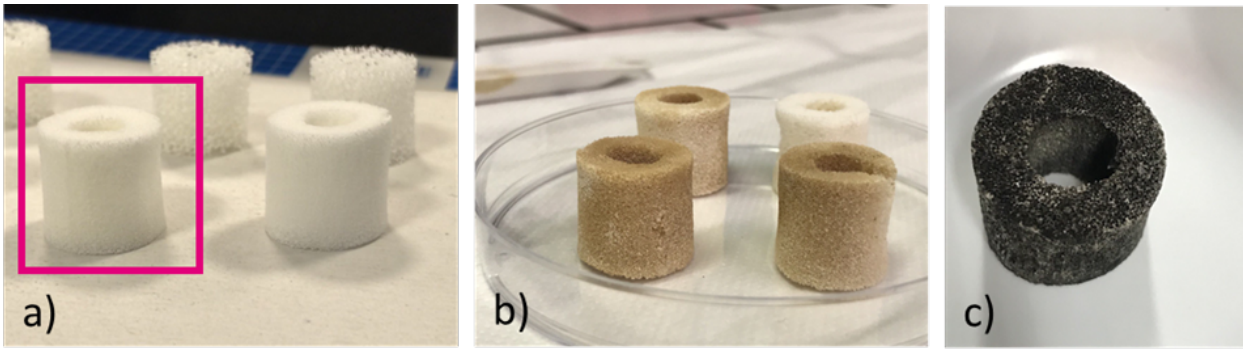

Figure 6.2. Three stages of the monolith foam catalyst preparation: a) α-Al2O3 foams, 90 ppi porosity; b) calcined γ- Al2O3 coated foams and c) calcined Ni-coated foam

the γ-alumina phase is deposited on the monolith surface through an impregnation method. The monolith is submerged in an aqueous solution containing 15 wt.% aluminium nitrate (Acros Organics, 99+% purity) for a period of 10 minutes. The foam is then calcined in air at 400°C for 2 hours. The final stage of preparation involves the introduction of nickel on the newly formed γ-alumina layer by impregnation. The monoliths are submerged in a solution of 15 wt% Ni(II) nitrate (Acros Organics, 99% purity) in deionised water for 10 minutes. The nickel-impregnated foam is then subjected to a final calcination at 500°C for 1 hour.

6.3.3 Materials characterization

Due to the peculiar structure of the ceramic foams and the impracticability of some characterizations on them, some preliminary analyses were done on α-Al2O3 flat that underwent the same coating procedures as the foams. The different coating stages on the discs were studied with X-ray diffraction technique (XRD) and SEM microscopy. The latter was also performed on a reduced Ni-coated foam.

XRD

XRD results for the discs are shown in figure 6.3 and figure 6.4. All the steps of preparation show diffractograms with sharp lines, associated with a crystalline structure. All the samples present a dominant crystallographic pattern, corresponding with the crystalline structure of corundum, i.e. the crystalline structure of the alpha-alumina. The gamma-alumina layer is not directly detected in the XRD pattern. This could be due to the thinness of the deposited layer. Ni-coated and reduced samples show three characteristic reflections of metallic Ni^0 (JCPDS 04-0850).

6.3.4 H2-TPR

Figure 6.5 illustrates the reduction curve obtained for the calcined Ni/γ-Al_2O_3 impregnated on the α-Al_2O_3 monolith foam. The profile displays three reduction peaks, indicating the presence of different Ni species with varying degrees of interaction with the support. The dominant peak at 359°C is attributed to the reduction of well-dispersed NiO species weakly interacting with the γ-Al_2O_3 support. This peak's high intensity and relatively low temperature suggest that a significant portion of the nickel is present in this form.

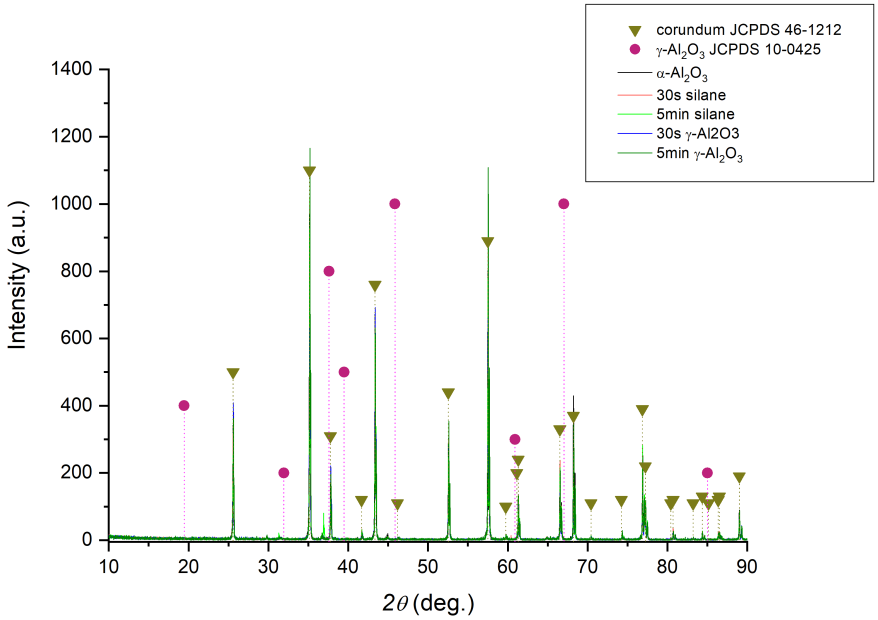

Figure 6.3. XRD diffractograms of α-Al2O3 discs (black line), after silanization (red and light green lines), and after γ-Al2O3 deposition (blue and green lines). The corundum structure pattern, associated with α-Al2O3 in the literature, is marked by green triangles and dotted lines. The pattern of γ-Al2O3 (JCPDS 10-0425) is marked by purple circles and dotted lines

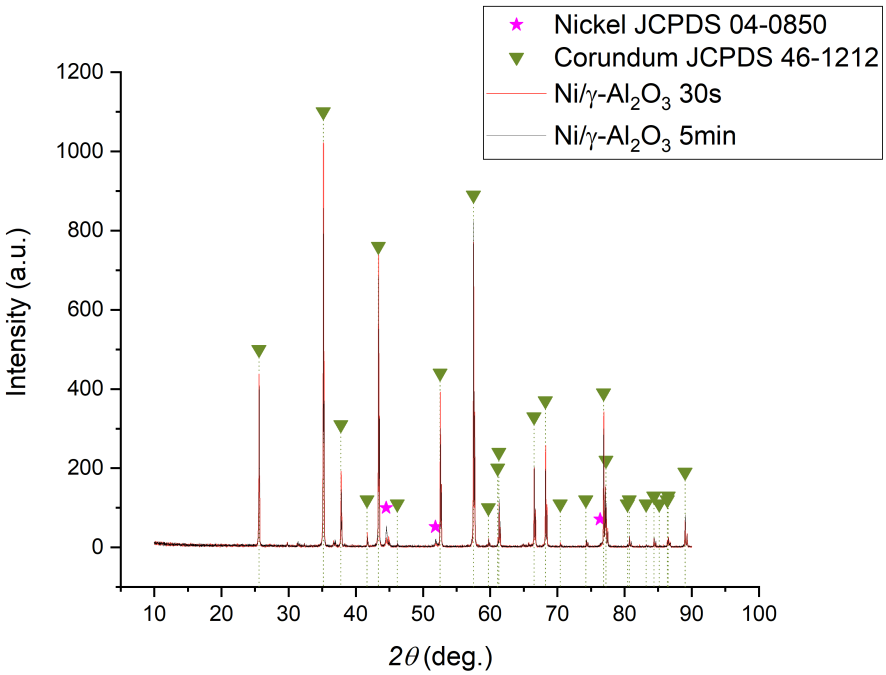

Figure 6.4. XRD diffractograms of Ni-coated Al2O3 discs (orange and grey lines), after reduction. The corundum structure pattern, associated with α-Al2O3 in the literature, is marked by green triangles and dotted lines. The pattern of metallic Ni (JCPDS 46-1212) is marked by pink stars and dotted lines.

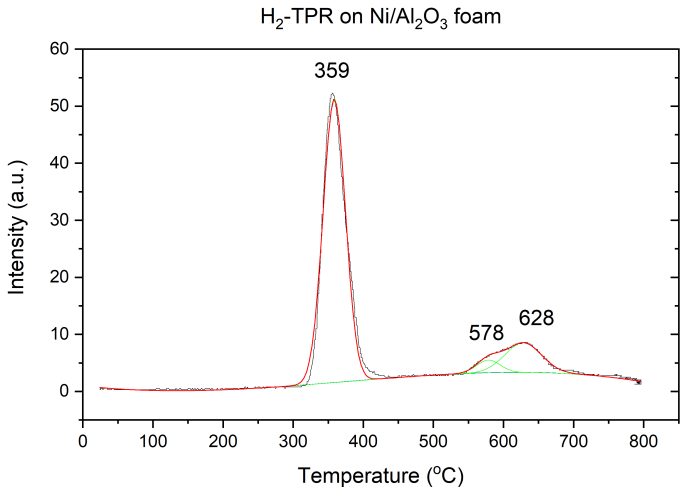

Figure 6.5. H_2-TPR curve of the Ni/Al_2O_3 monolith foam. The reduction peaks were fitted and the temperature values for the center of the fitted peaks are reported.(Source: own developement).

Two smaller, higher-temperature peaks are observed at 578 and 628°C. These peaks likely correspond to the reduction of nickel species with stronger interactions with the support. The presence of these higher-temperature peaks indicates a heterogeneous distribution of the Ni phase on the support, with some forming stronger bonds with the alumina.

6.3.5 DRM experimental setup

The experimental setup schematic is based on the general setup described in section 4.3. The novelty introduced is the monolith foam stage, which is illustrated in figure 6.6. The monolithic foam catalyst is placed co-axial with the electrodes axis, around the discharge gap. Considering the axis of the electrodes, the average distance of the plasma discharge from the monolith's internal walls is 3.5 mm. The foam tube is held in place by two custom-designed MACOR ceramic caps. These supports are interlocked with the anode and cathode stage ceramic supports, and they serve multiple purposes:

1. set the coaxial alignment with the electrodes' axis;
2. create an upper and lower boundary for the plasma-activated gas, which is forced to exit the reactor through the foam structure;
3. create an easily removable *catalyst stage*, minimizing material loss and foam damage in the reactor charge-discharge operations. The catalyst stage can therefore be removed to operate the discharge alone and it can be weighed separately before and after DRM experiments.

The electrode gap was reduced to a distance of (5 ± 0.2) mm to prevent direct contact between the discharge and the monolith foam surface, necessary to preserve the structural integrity of the catalyst. A series of preliminary tests were conducted using a prototype reactor and a transparent surrogate monolith to determine the optimal electrode separation distance and optimal internal diameter of the foam. These studies

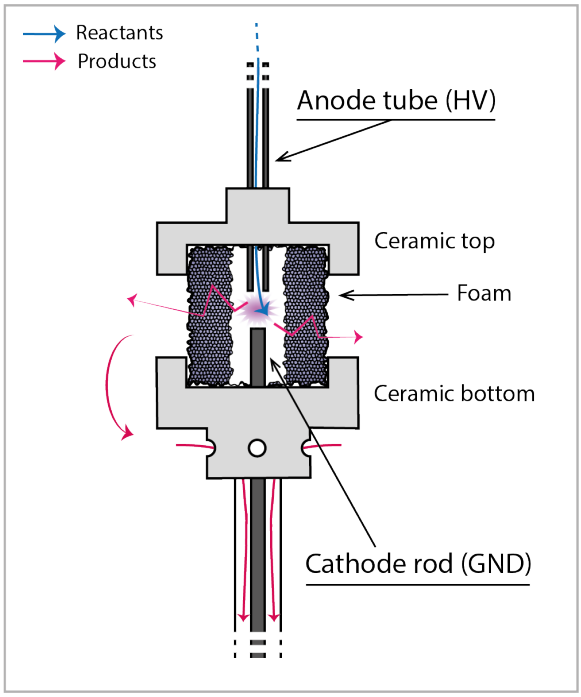

Figure 6.6. Foam reactor sketch.

facilitated the identification of a gap that ensures the pin-to-pin nanosecond repetitively pulsed discharge remains confined within the hollow cylindrical space, coaxial to the electrode axis, without bridging to the catalyst surface. The discharge is operated at atmospheric pressure.

While the measurements with the powder catalysts were carried out changing SEI at constant reactant flux $\Phi^{in}_{CH_4+CO_2}$, in the experiments with the foam catalysts we did the opposite. Knowing that the close presence of the discharge could heat up the monolith foam, we were interested in studying the catalytic performance as a function of the maximum temperature reached by it. Thus, by changing both f_p and $\Phi^{in}_{CH_4+CO_2}$ in the same proportion, we kept the SEI constant and influenced the maximum temperature reached by the monolith foam, as it is visible from figure 6.7. An IR camera monitored the temperature reached by the external wall of the monolith foam.

Three conditions, given by the tuples (f_p ,$\Phi^{in}_{CH_4+CO_2}$), were chosen as the following:

- (700 Hz, 150 sccm);
- (1200 Hz, 300 sccm);
- (2100 Hz, 450 sccm).

all three corresponding to a SEI = $(3.5 \pm 0.1) kJ/dm^3$.

In these experiments, for each of the previous conditions the three main preparation stages of the Ni/alumina catalyst have been studied separately: α-Al2O3, γ-coated and Ni-coated foam, which can be observed in figure 6.2.

Once the reactor is closed, 30 min of conditioning with 500 sccm N2 flux are performed in the reactor chamber. Then, only the reactant gas mixture of CH_4 and CO_2 flow is allowed in the reactor, and a first chromatographic sequence is run with the discharge off as a reference. After this step, the discharge is

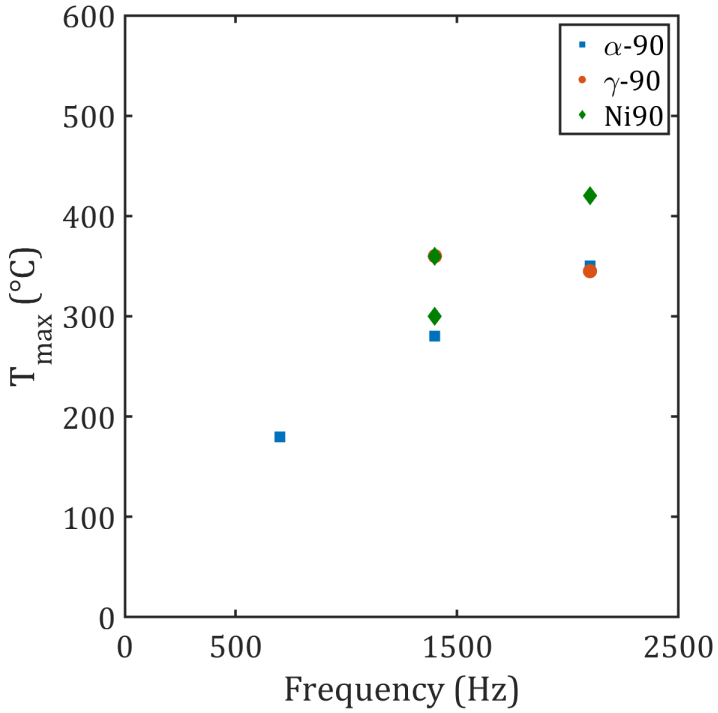

Figure 6.7. The maximum temperature measured on the foam's external wall is proportional with the plasma's pulse frequency in the continuous mode. Blue squares are α-Al2O3 foams, Red circles are γ-Al2O3 coated foams and Yellow diamonds are Ni-coated foams.

turned on at fixed energy and frequency, and the same chromatographic sequence is repeated. The steady-state condition is reached after the first 10 min from the discharge ignition.

The measure with discharge on was carried out for one hour. Unfortunately, it was not possible to conduct longer stability tests, as the system suffered from severe coking, which caused the reactor to become obstructed and internal pressure to increase significantly after such a time.

6.3.6 DRM results

The DRM results of these experiments are reported in figure 6.8, 6.9 and 6.10. The red dotted lines represent the results obtained with the plasma discharge alone at the same SEI of 3.5 kJ/dm3. We observed that all the foams produce an increase in the reactants conversions and an effect on the products selectivities, regardless of their preparation stage. In particular, the starting alpha-alumina foam shows a linear increase in conversions with temperature in the investigated range 180-380°C. Instead, the conversions with the Ni-coated foam tend to decrease with higher temperatures.

Selectivities on the syngas products is also affected by the presence of the foams, with a lower production of carbon monoxide detected, which needs to be investigated further.

Considering the selectivities of the lighter hydrocarbons C_2H_2, C_2H_4 and C_2H_6, we see that they change when the foams are included in the system, with a preference towards acetylene production and less ethane and ethyne with respect to the plasma-alone condition.

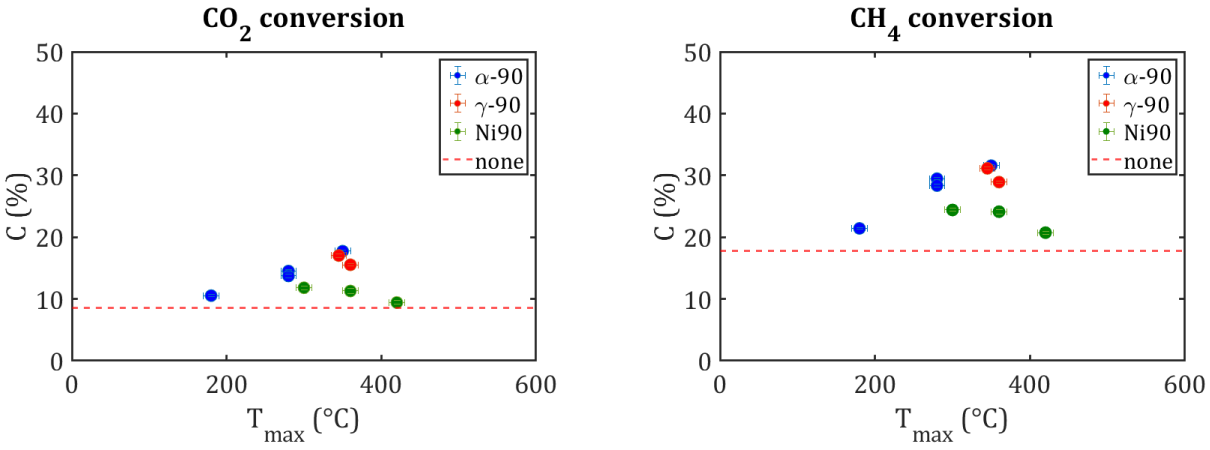

Figure 6.8. CO_2 conversion (left panel) and CH_4 conversion (right panel) in the DRM plasma-catalytic reaction with: alpha-alumina (blue marker), gamma-alumina (red marker) or Ni-coated (green marker) foams. The red dotted line is the plasma-alone result reference. The SEI is constant at 3.5 kJ/dm^{-3}. (Source:own developement).

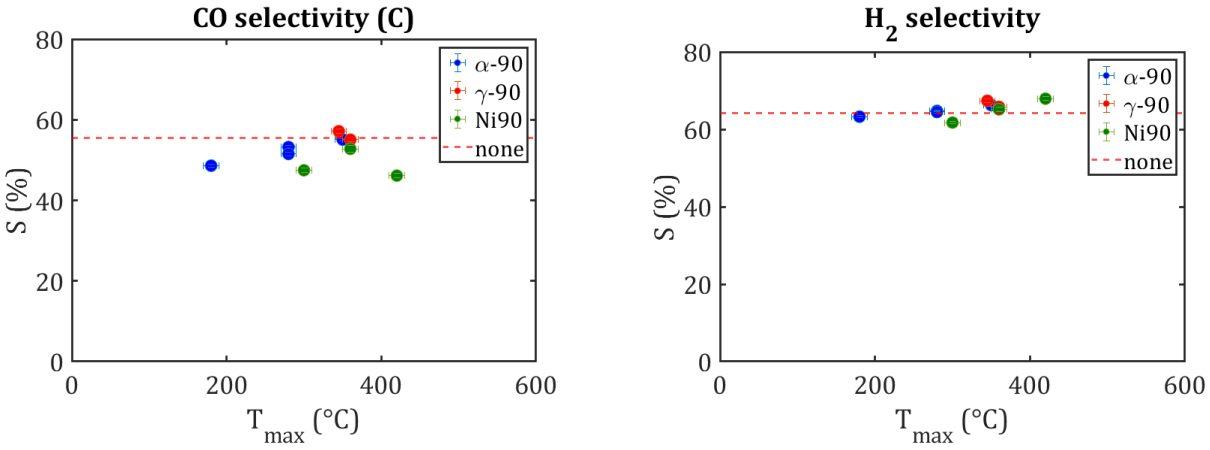

Figure 6.9. From left to right: carbon selectivity of acetylene (C_2H_2), ethane (C_2H_4) and ethyne (C_2H_6)in the DRM plasma-catalytic reaction with: alpha-alumina (blue marker), gamma-alumina (red marker) or Ni-coated (green marker) foams. The red dotted line is the plasma-alone result reference. The SEI is constant at 3.5 kJ/dm^{-3}.

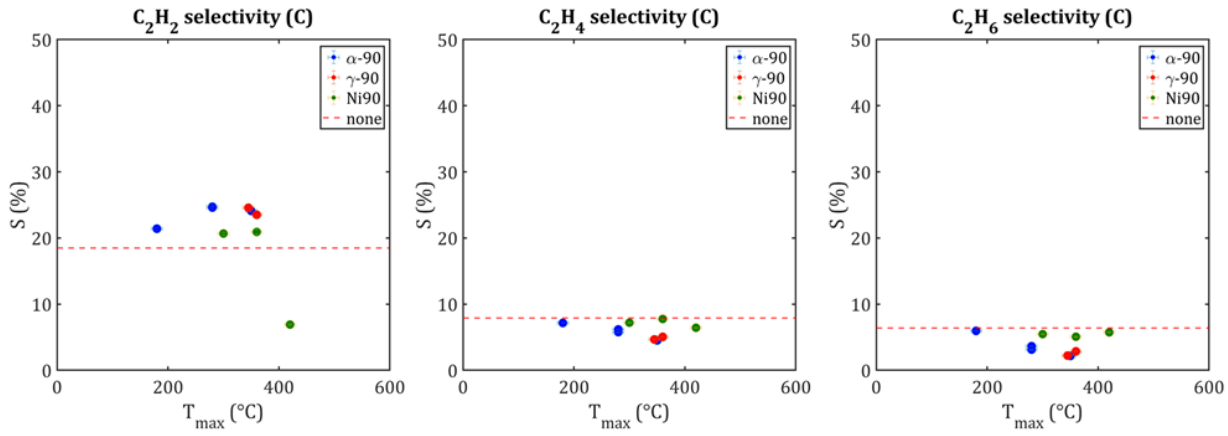

Figure 6.10. Enter Caption

6.3.7 Characterization of the spent catalyst

XRD

The X-ray diffraction (XRD) patterns are presented in figure 6.11 for the Ni/Al_2O_3 foams spent in the three experimental conditions.

The diffractograms exhibit a series of well-defined peaks, indicating the presence of crystalline phases within the catalyst samples. The peaks associated with metallic nickel (Ni^0) are clearly visible and correspond to the reference pattern JCPDS 04-0850, denoted by the pink stars in the figure. These peaks are observed at approximately 2ϑ of 44.5, 52, and 76 °, characteristic of the face-centred cubic (fcc) structure of metallic Ni. The catalyst exposed to 1400 Hz appears to exhibit the most intense Ni peaks, potentially indicating a higher degree of nickel crystallinity or larger nickel particles in this experimental condition.

6.4 Part II: Study of discharge confinement with different monolith foam supports

The second part of this study is meant to assess the role of the foam support material in the interaction with the plasma. The foams of this study were synthesised in Krakow with an optimised procedure that made the structure more mechanically stable and resistant. The materials chosen for this study were α-Al_2O_3 and 8 wt.% yttria-stabilised zirconia (YSZ or 8YSZ, also referred to in this text as simply zirconia). The latter material was chosen because of its suitability to substitute alumina in the developed synthesis procedure. The results are evaluated in terms of the DRM performance.

6.4.1 Ceramic foam synthesis

The structure of the ceramic monolith foam is obtained through the *foam replica method*, as a replica of a polyurethane foam of chosen porosity (90 PPI-pores per inch) and dimensions. The polyurethane (PU) foams (ARE Articoli Resine Espanse – Milano Italy) of 90 pores per inch (PPI) porosity were laser cut into hollow cilynders of 20 mm height, 20 mm ext. diameter and 10 mm int. diameter. A slurry of 67.21

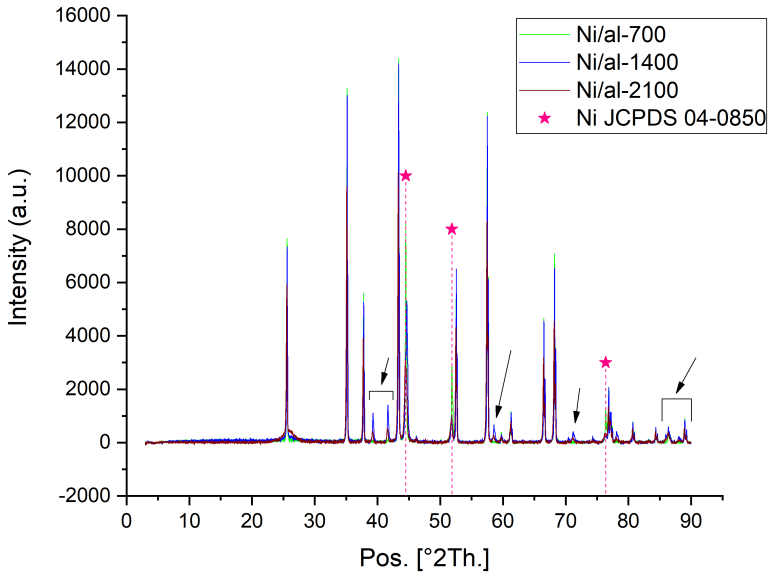

Figure 6.11. Comparison of the XRD diffractometries of the spent foams in the three different frequency conditions: 700 Hz, 1400 Hz, 2100 Hz.

wt.% α-Al_2O_3 powder (Almatis D50 = 0.5 µm), 25.63 wt.% distilled water and 1.11 wt.% dispersant agent (Darvan 821 A) is obtained and mixed in a planetary ball mill (Retsch PM 100) with an equal weight of zirconia milling spheres as the powders for 2 h. At this point, the remaining 6.06 wt.% of binder (Duramax B1014) is added. The mixture is stirred with a magnetic anchor at 200 rpm for 2 h. The polymeric template foam is immersed in the slurry, squeezed to remove the excess and left drying overnight at 80°C. During a slow heat treatment in a high temperature furnace (Carbolite Gero HTF 1700), the samples are heated up to 1550 °C in air. The heating treatment steps are the following:

- Ramp 1: RT-400°C, 2°C/min;
- Plateau 1: 400°C, 2 h;
- Ramp 2: 400-1100°C, 1°C/min;
- Plateau 2: 1100°C, 2 h;
- Ramp 3: 1100-1550°C, 1 °C/min;
- Plateau 3: 1550°C, 2 h;
- Ramp 4: 1550-1100°C, 2 °C/min;
- Ramp 5: 1100°C-RT, free cooling.

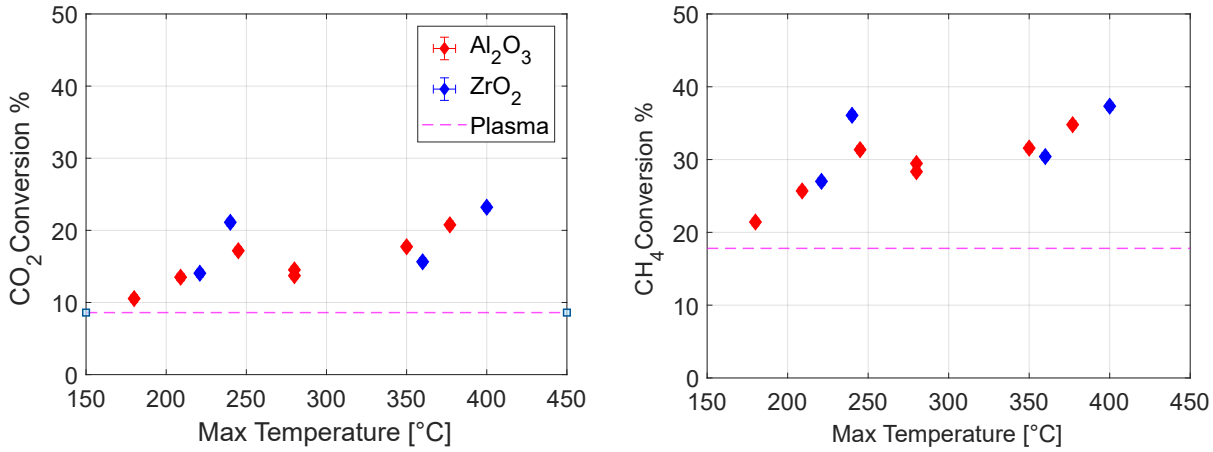

Figure 6.12. CO_2 conversion (left panel) and CH_4 conversion (right panel) in the DRM plasma-catalytic reaction with: alpha-alumina (red marker) and YSZ (red marker) foams. The purple dotted line is the plasma-alone result reference. The SEI is constant at 3.5 kJ/dm^{-3}. (Source:own developement).

6.4.2 DRM results

Figures 6.12, 6.13 and 6.14 show respectively the comparison between the measured reactant conversions and main products selectivities of α-Al_2O_3 and YSZ monolith foams.

From figure 6.12 it is clear that the zirconia foam behaves in the same way as the alumina foam. The two linear behaviours follow the same trend, suggesting that the foam composition is not a key factor that influences CO_2 or CH_4 conversion.

As for the selectivities shown in figure 6.13 and figure 6.14, the data are here more scattered but, nonetheless, the two distributions seem follow the same patterns.

These results suggest that the composition of the monolith foams support is not an influence factor in the interaction with the plasma-produced species and the foam surface. To justify the different reaction performance with and without a monolith foam, research should be shifted in investigating the confinement effect brought by the foam presence, which could influence the reaction performance in a physical rather than chemical way.

6.5 Summary

The investigation of discharge confinement was undertaken to address the limitations observed in post-plasma catalyst placement. Monolith foam-supported catalysts in a coaxial geometry were explored as a potential solution. This configuration was designed to position the catalyst in closer proximity to the plasma discharge, enhancing the interaction between the plasma-generated species and the catalyst surface.

The structure of the ceramic monolith foam was obtained by the foam replica method [151], as a replica of a polyurethane foam of chosen porosity and geometry. The foam is a hollow cylinder surrounding the discharge in a coaxial configuration. The proximity of the foam to the active plasma region facilitated expo-

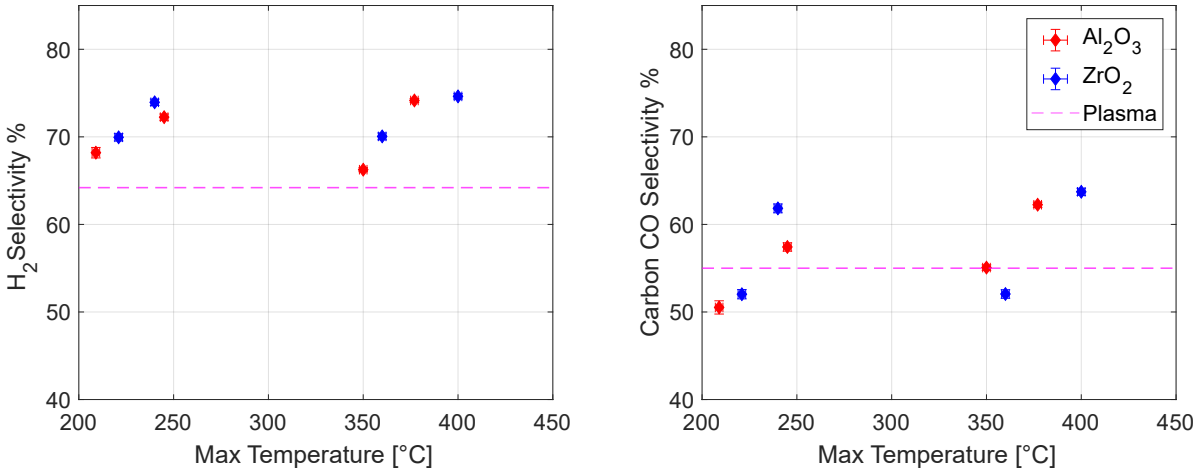

Figure 6.13. H_2 selectivity towards hydrogen (left panel) and CO selectivity towards carbon (right panel) in the DRM plasma-catalytic reaction with: alpha-alumina (red marker) and YSZ (red marker) foams. The purple dotted line is the plasma-alone result reference. The SEI is constant at 3.5 kJ/dm^{-3}. (Source:own developement).

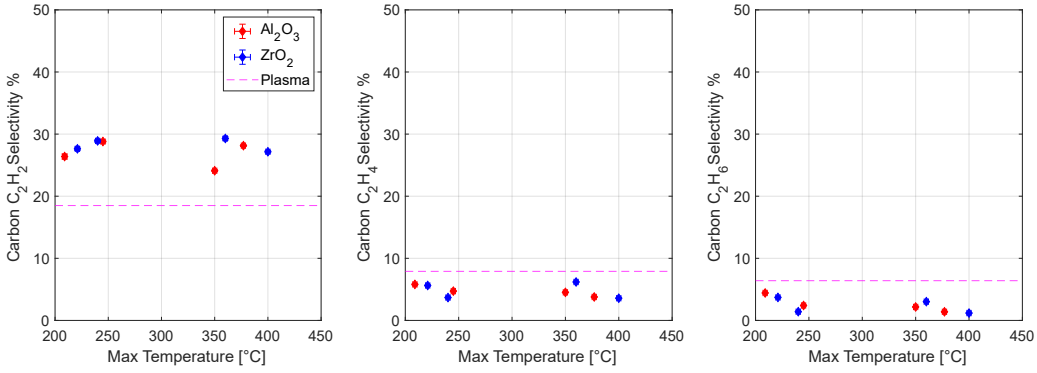

Figure 6.14. C2 hydrocarbons selectivities towards carbon in the DRM plasma-catalytic reaction with: alpha-alumina (red marker) and YSZ (red marker) foams. The purple dotted line is the plasma-alone result reference. The SEI is constant at 3.5 kJ/dm^{-3}. (Source:own developement).

sure to reactive species and indirect heating by the plasma. This dual activation mechanism, which combines thermal and plasma effects, was hypothesised to enhance catalytic performance.

To investigate the influence of foam composition, two support materials were compared: Y_2O_3-ZrO_2 and α-Al_2O_3. Additionally, the α-Al_2O_3 foam was functionalised by impregnation with γ-Al_2O_3 and 15 wt% Ni/γ-Al_2O_3 to examine the contribution of a catalyst on the foam surface.

A critical aspect of the experimental design was the ability to modulate the foam temperature while maintaining a constant SEI. This was achieved by proportionally adjusting the discharge power and reactant flux. A calibrated IR thermocamera was used to measure the temperature of the foam's external surface, enabling correlation with conversion and selectivity results.

The experimental findings revealed that the foam presence improved the DRM performance, compared to plasma alone. Both Y_2O_3-ZrO_2 and α-Al_2O_3 supports exhibited a linear increase in CO_2 and CH_4 conversions with rising temperature, surpassing plasma-only conditions. However, the composition of the foam was not a discriminant factor. Conversely, Ni-coated foams demonstrated a decrease in conversions at higher temperatures.

The presence of foams also altered product selectivities, with a decrease in CO production and a shift towards acetylene over ethane and ethene. Notably, these effects were observed even with uncoated foam structures, suggesting that the foam itself plays a crucial role in modifying the plasma-catalytic process.

These results indicate that the foam structure influences the reaction through multiple potential mechanisms. These may include temperature modulation, altered gas dynamics, or enhanced surface interactions.

Chapter 7

Powder catalyst in quartz wool nest coupling

7.1 Introduction

In the previous chapter, the structure of the monolith foam was investigated, with the aim of having a catalyst as close to the discharge as possible while avoiding direct contact with it. Although the monolith foam catalyst succeeded in improving the conversions in the DRM reaction, it suffered from numerous limitations.

First, the foam bulk material had to comply with the requirements posed by its synthesis method. The foam replica method requires materials that can form stable, high-solid-content slurries with appropriate rheological properties for uniform coating of polyurethane templates. The chosen materials must also exhibit suitable sintering behaviour, thermal stability, and mechanical strength to maintain the foam structure during processing and subsequent catalytic use. In addition, the foam substrate required functionalisation through impregnation or washcoating to improve its low surface area and add an active material on its surface. However, despite functionalisation through impregnation, the foams exhibited low surface areas, and the technique lacked control over the dispersion of the active phase.

Despite these limitations, monolith foam catalysts demonstrated potential as a foundation for further studies. Based on the original idea, we sought to create a structure that could hold the catalyst close to the plasma, like monolith foams, but offered the variety, adaptability, and tunability of powder catalysts.

The key structure used in these experiments is what we called a *quartz wool nest*. This structure is obtained by pressing a constant volume of quartz wool into a custom made plastic mold, and by needle felting the wool into a firm, self-sustaining structure. The geometry chosen in our case is that of a hollow cylinder, which is meant to surround the plasma discharge from a close distance. The quartz wool nest frame can host any type of catalyst beads or powders, opening the way to infinite catalyst customisation possibilities.

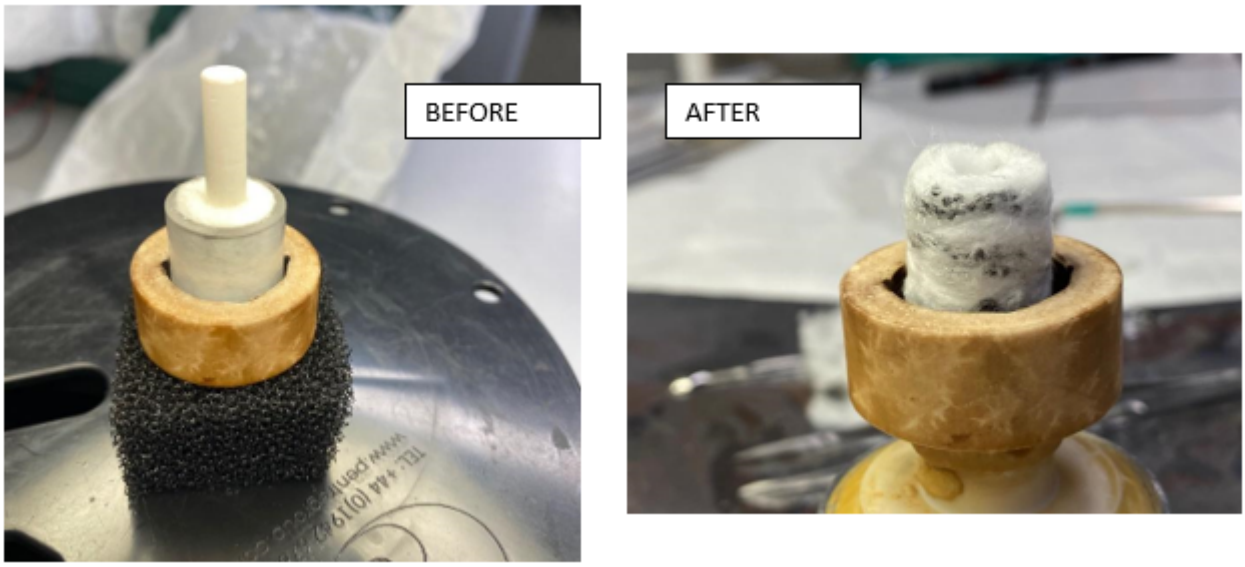

Figure 7.1. Quartz wool nest structure while being in the shaping mold (Before) and after the mold has been removed.

7.2 Experimental setup

The experimental setup schematic is based on the general setup described in the methods chapter, section 4.3 and in the monolith foam chapter (section 6.3.5), where the monolith foam stage is implemented (figure 6.6). The quartz wool nest is placed co-axial with the electrodes axis, around the discharge gap. In-line analysis of the effluent mixture is carried out by a gas-chromatographer (990 uGC, Agilent Technologies Inc.). This time the IR thermal camera is not equipped, as the temperature of the catalyst could not be monitored, due to the quartz wool shielding.

The discharge is operated at atmospheric pressure, with an electrode gap of (5 ± 0.2) mm. The DRM reaction was performed in two conditions, corresponding to different SEI values. In fact, in both cases the reactant gases were CO_2 and CH_4 in proportion 1:1, with a constant total flow rate of 300 sccm. As for the NRP discharge, it was operated in continuous mode with two different frequencies: 1400 Hz and 2100 Hz. The two conditions allowed to explore the SEI values of (3.3 ± 0.4) kJ/dm^3 and (5.0 ± 0.4) kJ/dm^3, respectively.

The duration of each measure was set at 25 minutes. Each SEI condition has been studied in four distinct configurations, where the plasma blank, quartz wool blank and catalyst support blank are considered:

1. only plasma (indicated as “plasma”),
2. quartz wool nest alone (“qw”),
3. quartz wool nest with γ-Al_2O_3 catalyst support powder (“qw + Al_2O_3”)
4. quartz wool nest with 10 wt.% Ni/γ-Al_2O_3 powder catalyst (“qw + Ni/Al_2O_3”).

7.2.1 Catalyst preparation

The chosen catalyst used in this study is a powder 10 wt.% Ni/Al_2O_3 catalyst. Its synthesis and characterisation are described in detail in chapter 5 of this thesis. It was synthesised with a standard incipient wetness impregnation method at AGH University. The catalyst was calcined at 550° C for 4 h in air.

Finally, the powder catalyst was reduced under 200 sccm of 5% H_2/Ar flow at 650°C for 4 hours in a tubular furnace, after a ramp of 10°/min. The operation was done *ex situ*, before packing it into the quartz wool nest.

7.2.2 Quartz wool nest preparation

In order to control that the density and other quartz wool nest properties were the same every time, we weighed the quartz wool to 1300 mg and used a constant volume of catalyst powder, corresponding to 230 mg of the 10 wt.% Ni/Al_2O_3 catalyst. The quartz wool was then arranged into long strips, onto which the catalyst powder was uniformly distributed, which were wrapped into quartz wool snakes. These were finally layered on top of one another in the plastic hollow cylinder mold, and needle felted until the structure became firm and compact and the mold could be removed. These two final stages of the quartz wool nest preparation are shown in figure 7.1.

7.2.3 Calibration of systematic error

During the whole measurement campaign, the μGC was calibrated twice. To account for a systematic error related to the difference in the two calibrations, we compared the response factors obtained from the calibration regression lines for each analyzed species. The biggest distance between tuples of response factors was generalized as the systematic error of calibration for all the gas species. On the percentage molar fractions given by the μGC software, this systematic error is $\pm 4\%$. The propagation of this error is computed for all the derived quantities and given separately in the results discussion.

7.3 DRM results

The plasma-catalytic dry reforming of methane (DRM) reaction was investigated under two specific energy input (SEI) conditions: (3.3 ± 0.4) kJ/dm^3 and (5.0 ± 0.4) kJ/dm^3. These conditions corresponded to plasma pulse frequencies of 1400 Hz and 2100 Hz, respectively, with a total reactant flow of 300 sccm.

For each condition, the molar fractions obtained from the µGC were re-scaled (see equation (4.31) and equation (4.32)) to determine the mass balances towards carbon, hydrogen and oxygen in time. These mass balances were initially verified for consistency. Subsequently, their average values in time were calculated and integrated with the molar fractions of water, which were obtained from the Karl Fischer analysis of the liquid products. This way, an assessment of the comprehensive mass balances could be done, before proceeding. The systematic error in mass balances due to µGC calibration was estimated to be ± 6 mass balance points.

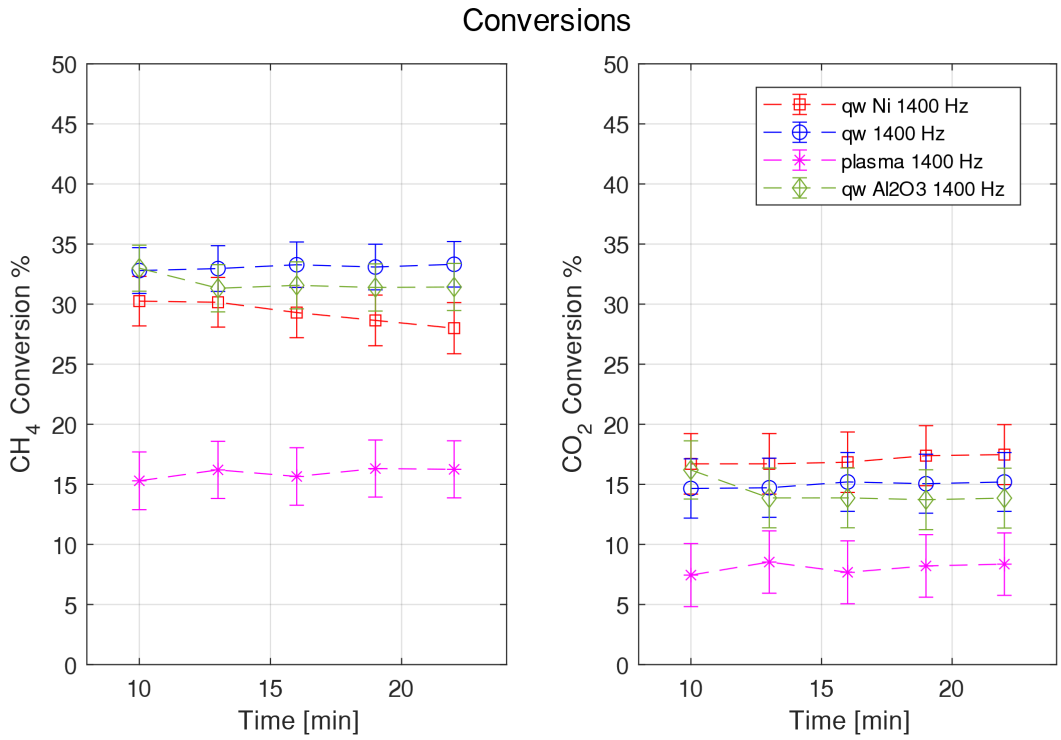

Figure 7.2. Conversions of CH_4 and CO_2in time at 1400 Hz - SEI = 3,5. Different colours and symbols refer to the 4 different configurations studied.

Conversion values were calculated at each time step, and their behaviour in time is presented. Selectivities for the µGC-detected products were also calculated at each time step. As these selectivities exhibited a constant behaviour in time, their time-averaged values are reported. These average selectivities are compared with the selectivities for water production.

Unless otherwise specified, all error bars in the graphical representations account for $\pm 2\sigma$, where σ represents the standard deviation. This approach ensures a 95% confidence interval for the reported results.

7.3.1 Condition at SEI = 3.3 kJ/l

The conversions rates of CH_4 (left) and CO_2 (right) over time are reported in figure 7.2 for different experimental configurations and for the plasma-catalytic DRM reaction at 1400 Hz.

We first observe that the quartz wool (qw) configurations with Ni catalyst, Al_2O_3 support, and qw alone all show significantly higher conversion rates for both CH_4 and CO_2compared to plasma alone. These configurations roughly double the conversion rates of both reactants. CH_4 conversion ranges from about 15-18% for plasma alone to about 30-35% for the qw configurations, whereas CO_2conversion ranges from about 8-10% for plasma alone to about 15-18% for the qw configurations. However, the difference between the nest and catalyst blanks (qw and qw+Al2O3) and the Ni/Al2O3 catalyst is not as strong as we would expect. A significant overlap in error bars for the different qw configurations suggests that differences between them may not be statistically significant.

All configurations show relatively stable conversion rates over the 25-minute reaction period, with only minor fluctuations. An exception seems to be that of CH_4 conversion with the Ni/Al2O3 catalyst, which shows a slight negative trend. This could potentially be attributed to several factors. The gradual decrease in CH_4 conversion might indicate a progressive deactivation of the Ni catalyst. This could be due to carbon deposition (coking) on the catalyst surface, which is a common issue in methane reforming reactions. Competing reactions could also be taking place, forming methane again, such as reverse methanation ($CO_2 + 4\,H_2 \longrightarrow CH_4 + 2\,H_2O$) or from hydrogenation of carbon deposits ($C + 2\,H_2 \longrightarrow CH_4$). This last hypothesis should should be confirmed by variations in the conversion of $CO_2$and in the formation of hydrogen and water, which is not the case, as we will see. Other influencing factors could be related to temperature effects or mass transfer limitations in the nest. As the reaction progresses, there might be changes in the gas flow dynamics or diffusion limitations within the catalyst structure, which could affect the overall conversion.

The average selectivities towards carbon, hydrogen and oxygen are reported in figures 7.3 to 7.5 for the detected species. A comparison is shown for the different configurations.

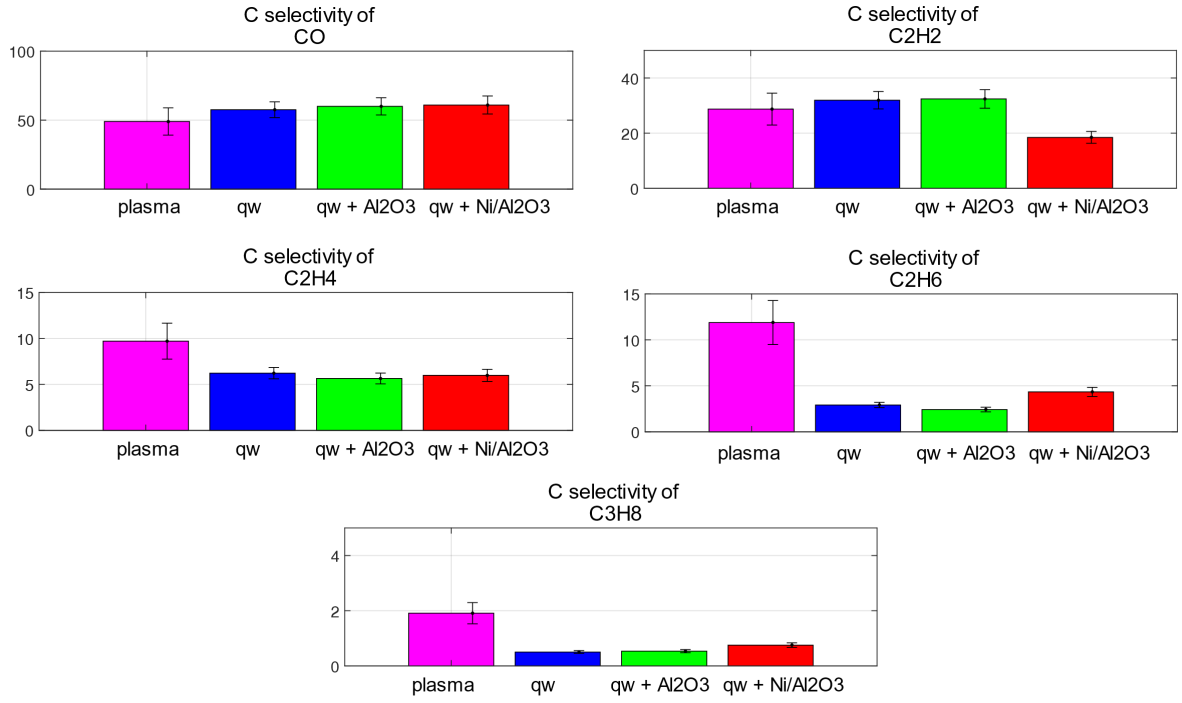

Figure 7.3. Conversions of CH_4 and CO_2in time at 1400 Hz - SEI = 3,5. Different colours and symbols refer to the 4 different configurations studied.

We observe that syngas is the main product across all configurations. The selectivities of H2 (about 75-80% towards hydrogen) and CO (about 65-70% towards carbon) remain relatively consistent across the different configurations, suggesting that the core DRM reaction pathways are maintained regardless of the catalyst or support presence.

Among light hydrocarbons, acetylene (C_2H_2) is the most abundant product, with carbon selectivities ranging about 8-12%. Here, the Ni/Al2O3 catalyst configuration shows a slightly lower C_2H_2 selectivity compared to the other configurations. At the same time, the Ni catalyst appears to promote ethane (C_2H_6)

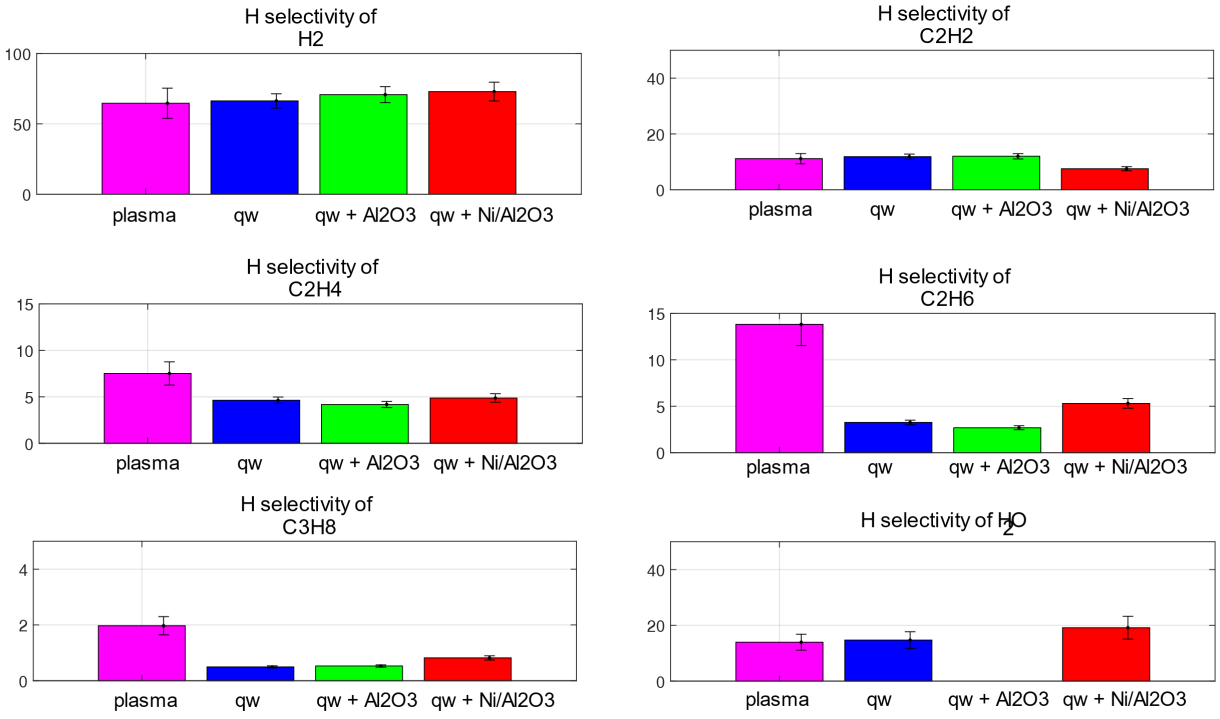

Figure 7.4. Conversions of CH_4 and CO_2in time at 1400 Hz - SEI = 3,5. Different colours and symbols refer to the 4 different configurations studied.

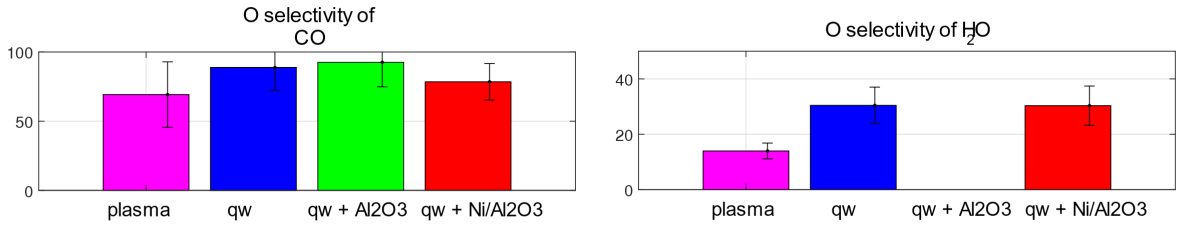

Figure 7.5. Conversions of CH_4 and CO_2in time at 1400 Hz - SEI = 3,5. Different colours and symbols refer to the 4 different configurations studied.

production, compared to the other qw configurations. In general, the plasma-alone configuration exhibits higher selectivities for C_2H_4, C_2H_6 and C_3H_8 (propane) compared to the configurations with quartz wool (qw) structures. This suggests that the confined reaction volume and increased surface area provided by the qw structure influence reaction pathways, possibly through enhanced radical recombination or secondary reactions.

The selectivity data towards water is missing for the Al2O3 support in quartz wool configuration. From the oxygen selectivities, however, we see that Water production seems slightly increased in the qw configurations compared to plasma alone. This could be due to enhanced surface reactions or local temperature effects promoting water-forming side reactions.

Overall, these selectivity patterns indicate that the quartz wool structure influences the product distribution, particularly by suppressing the formation of larger hydrocarbons (C_2H_4, C_2H_6, C_3H_8) and promoting

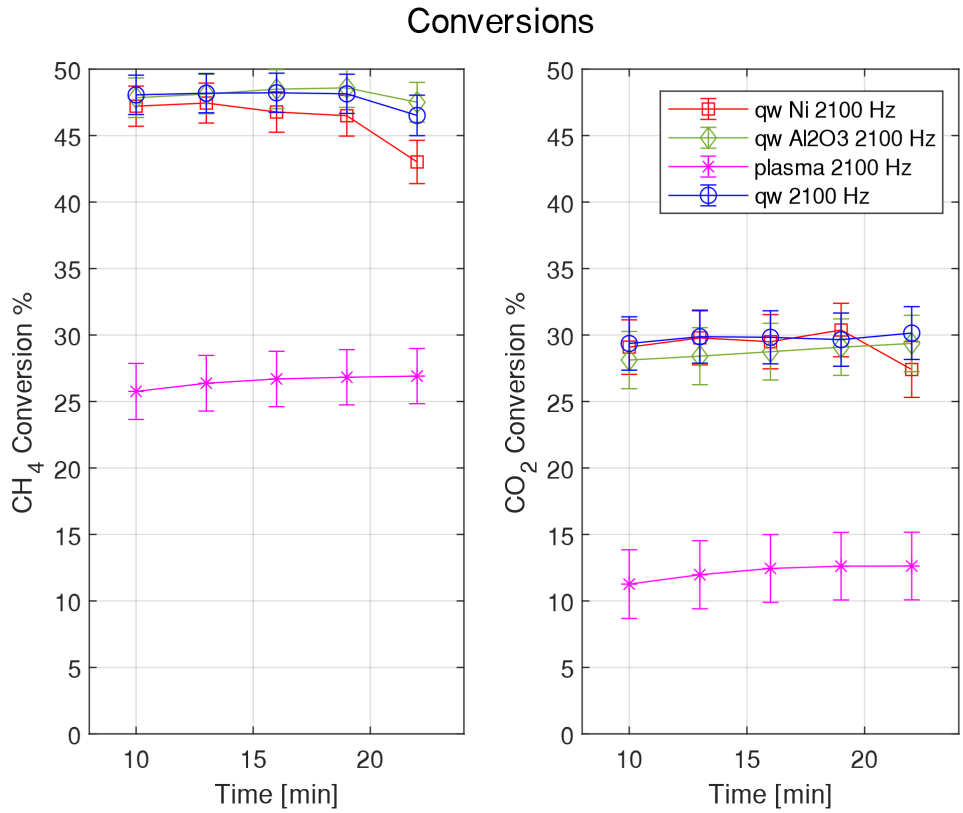

Figure 7.6. Conversions in time for the 2100 Hz condition.

water formation. The selectivity pattern indicates that the qw structures, regardless of catalyst loading, promote syngas formation while suppressing the production of larger hydrocarbon molecules compared to plasma alone.

7.3.2 Condition at SEI = 5.0 kJ/l

Figure figure 7.6 shows the conversion rates for CH_4 (left) and CO_2(right) over time at a higher specific energy input (SEI) of 5.0 kJ/dm^3, compared to the previous 3.3 kJ/dm^3 condition. Compared to the lower SEI condition, both CH_4 and CO_2conversion rates have shifted up for all configurations. This is expected due to the higher energy input promoting more reactive species and collisions.

Again, we notice a clear distinction between the configurations with or without a nest structure. CH_4 conversion ranges from about 25-28% for plasma alone to about 45-50% for the quartz wool (qw) configurations. CO_2conversion ranges from 11-13% for plasma alone to 28-31% in the quartz wool nest configurations.

The difference between the blanks (qw and qw+Al2O3) and the Ni catalyst configuration is almost always negligible. However, a noticeable distinction is visible in CH_4 conversion for the Ni catalyst configuration, where conversion starts to decrease around 15-20 min from the start of the discharge. This negative trend is more pronounced than in the lower SEI condition, possibly indicating accelerated catalyst deactivation or more significant competing reactions at higher energy inputs. CO_2conversion remains relatively stable for all configurations over time.

The average selectivities towards carbon, hydrogen and oxygen are reported in figures 7.7 to 7.9 for the detected species. A comparison is shown for the different configurations.

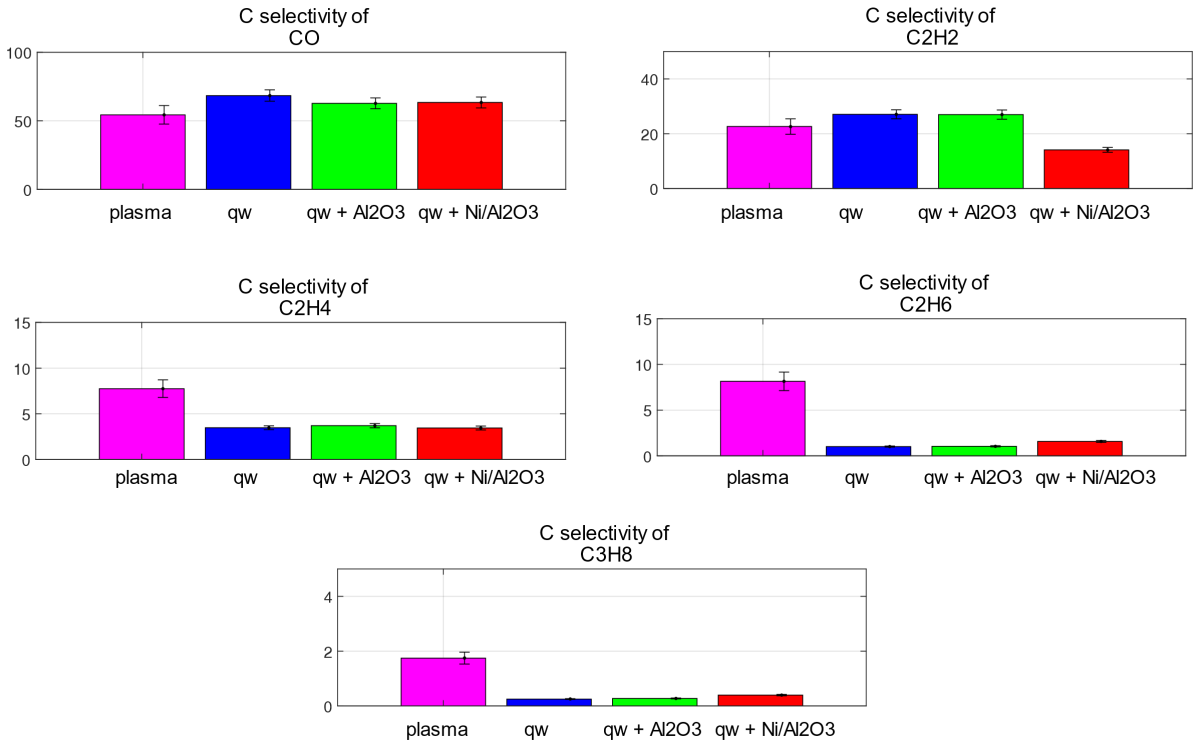

Figure 7.7. Average Carbon selectivities in the 2100 Hz condition.

From here, again, we can see that the main product remains syngas in all the configurations, and the selectivities of H2 and CO appear relatively consistent across the different configurations. H2 selectivity to hydrogen ranges around 70-80%, while CO selectivity towards carbon is about 60-70%.

Among the light hydrocarbons, acetylene (C_2H_2) remains the majority product, exhibiting selectivities in the range of 5-10%, despite showing notable variations across different configurations. The Ni catalyst demonstrates a marked suppression on acetylene formation, reducing its selectivity compared to other quartz wool (qw) setups. This observation suggests an enhanced catalytic activity for acetylene conversion at higher energy inputs, possibly leading to carbon deposition or further reaction to other products.

The selectivities for ethylene (C_2H_4), ethane (C_2H_6), and propane (C_3H_8) generally fall below 5%, showing a decrease compared to the lower SEI condition. Interestingly, the plasma-alone configuration consistently yields higher selectivities for these C2 and C3 hydrocarbons, compared to the qw configurations. This trend highlights the significant impact of the qw structure on reaction pathways, likely through altered residence times and enhanced surface interactions.

Water formation, with selectivities ranging around 15-20%, is not showing a remarkable difference between the plasma alone and qw configurations.

Again, the strongest information we get from these selectivities is the difference between the behaviour of plasma alone vs plasma coupled with a nest structure in the selectivities of C_2H_4, C_2H_6 and C_3H_8. For

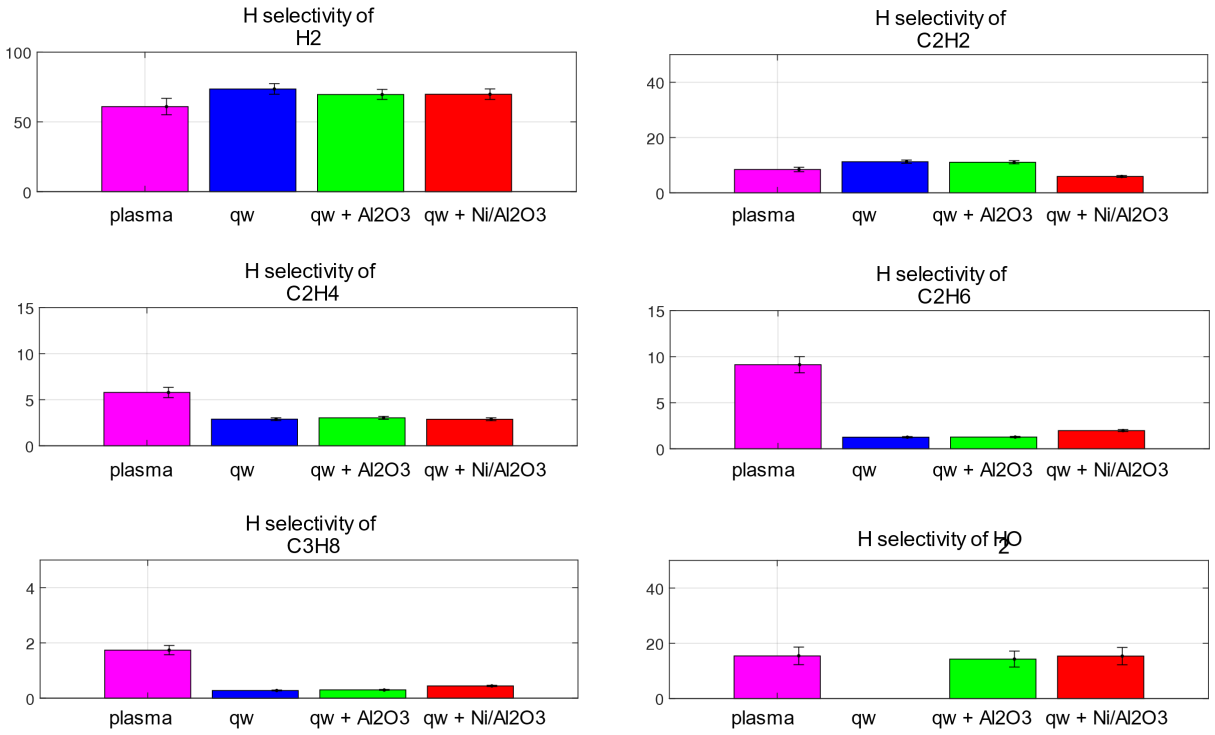

Figure 7.8. Average Hydrogen selectivities in the 2100 Hz condition.

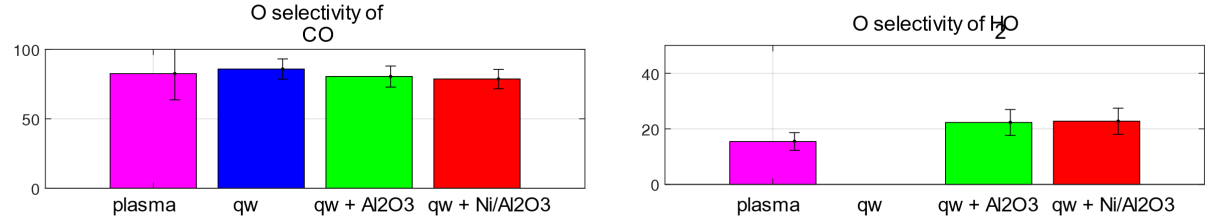

Figure 7.9. Average Oxygen selectivities in the 2100 Hz condition.

the plasma alone case, the formation of ethane, ethylene and propane is encouraged with respect to the nest structure case.

The selectivity patterns observed at 2100 Hz generally mirror those at 1400 Hz, but with intensified effects. The disparities in selectivities between plasma alone and qw configurations for certain products, particularly C_2H_4, C_2H_6 AND C_3H_8, appear more pronounced at the higher SEI. This amplification underscores the role played by energy input in determining the effectiveness of both the catalyst and confinement structure in shaping product distributions.

7.3.3 Syngas ratio

The last data analysis segment concerns syngas and the syngas ratio, which is an important parameter in the dry reforming reaction. Syngas ratio is defined as the fraction between the molar fractions of hydrogen and carbon monoxide (H2/CO). We checked whether the change in configuration was mirrored by a change in

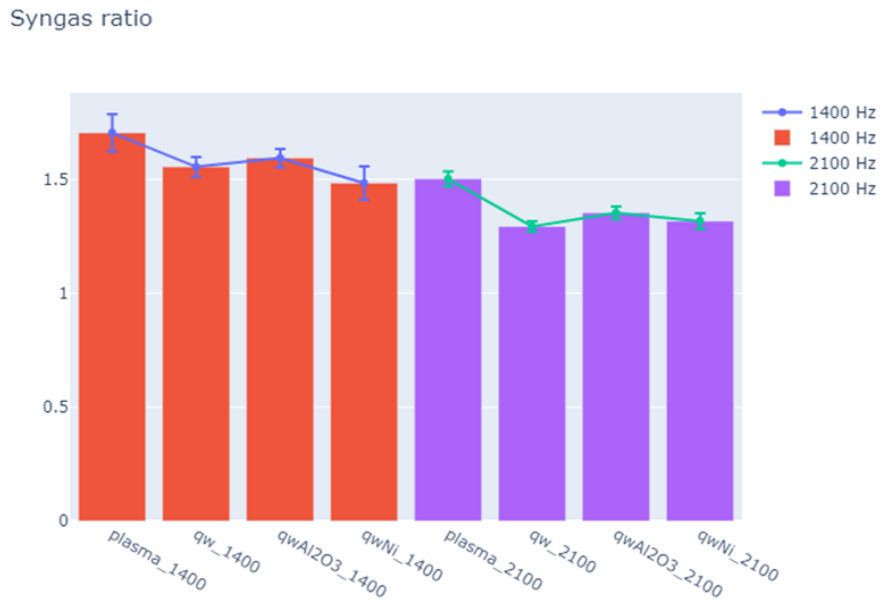

Figure 7.10. Syngas ratios (H2/CO) for the different configurations examined. The range spans from 1.7 to 1.3. The red bars refer to the 1400 Hz, lower SEI condition, while the purple bars to the 2100 Hz, higher SEI condition.

this ratio, which is a key parameter in the synthesis gas utilization processes. The results are displayed in figure 7.10 where, this time, the measure uncertainties account for $\pm 1\sigma$.

We can see that the maximum syngas ratio is obtained in the lower energy, plasma-alone condition (1400 Hz, SEI = 3.3 kJ/L), with H2/CO =(1.70±0.08). The minimum values, instead, correspond to the nested conditions at higher frequency (2100 Hz, SEI = 5 kJ/L), with a ratio around 1.3. In general, the nested configurations behave similarly in the same reaction conditions and do not show a correlation with the catalyst type. Instead, the nest presence seems sufficient to lower the syngas ratio, with respect to the plasma-alone case.

7.4 Characterization of the spent catalyst

The catalyst used in the 1400 Hz pulse frequency condition was selected for XRD analysis. The XRD diffractogram of the spent catalyst is shown in figure 7.11. Reflections originating from the alumina phase are present (ICOD 96-120-0016) at values of 2ϑ about 38, 39.5, 46, 67°. We can also confidently assign the reflections of the reduced Ni^0 phase at 2ϑ of 44.5, 52 and 76.5°(ICOD 96-901-2970). In addition, two reflections ascribable to graphitic carbon are identified. These are found at values of 2ϑ of 26 and 44°(ICOD 96-120-0018).

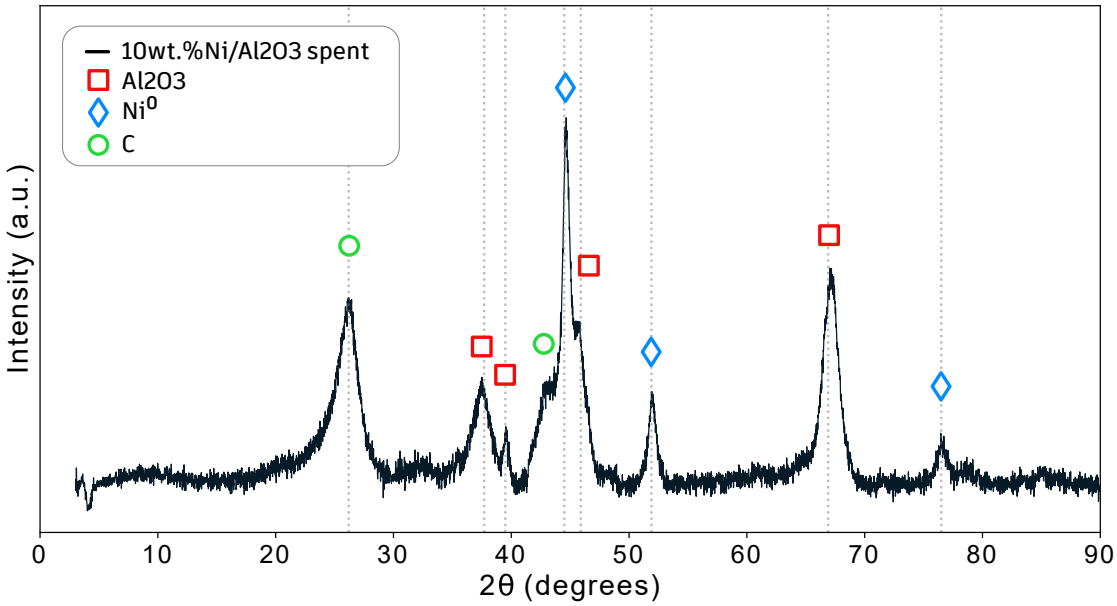

Figure 7.11. XRD of 10 wt.% Ni/Al_2O_3 powder catalyst after DRM reaction at 1400 Hz pulse frequency.

7.5 Summary

A plasma-catalytic coupling in the dry reforming reaction was obtained by combining a ns discharge plasma in pin-to-pin configuration with a co-axial nest structure, made with quartz wool, where the catalyst powder was hosted. The experiments were meant to assess the differences between a plasma-alone case and the plasma-catalytic configuration with the nest structure and, within the latter, to investigate a contribution from the selected 10 wt.% Ni/Al2O3 powder catalyst.

The nest structure alone, loaded with the catalyst support or with the Ni catalyst, shows a similar behavior, with some exceptions. The conversions of $CO_2$and methane approximately double the ones obtained with plasma alone, and the factor slightly increases for CO_2conversion at higher SEI. ¬As for product selectivities, the main products of reactions are always CO and H2, with no significant variation between configurations. Immediately after syngas, acetylene and water have the highest selectivities, with C_2H_2 production decreasing in presence of the Ni catalyst. Other simple hydrocarbons, such as ethylene, ethane and propane are favored more in the plasma-alone configuration and suppressed when a nest structure is introduced in the coupling.

Although more statistics is needed for further insights in the process, we could suggest a first interpretation of the data:

- The confinement of the discharge has always a positive effect on the conversion of $CO_2$and CH_4, whether a catalyst is present or not. The causes could be many, but the main processes involved could be: an increase of the temperature in the confined volume, the presence of a surface enhancing the interaction of the produced radicals and species with the surface, and a change in the fluid dynamics of the process;

- The role of the nest structure in suppressing the production of ethylene, ethane and propane and its promotion of water production could be related with a decomposition of the produced hydrocarbons, due to the increase in the provided thermal energy and the presence of a surface;
- The lower selectivities of acetylene in presence of the Ni catalyst could be associated with a decomposition of these products to favour the formation of carbon deposits at the reached temperatures, as found by Baker et al. [157]. This hypothesis is supported by the observed correlation with the carbon lack.

Chapter 8

Concluding Remarks and Future Work

This thesis investigated the plasma-catalytic dry reforming of methane reaction (DRM) with a nanosecond repetitively pulsed (NRP) discharge plasma, with a focus on achieving synergistic effects through post-plasma catalyst placement.

In **chapter 1** we presented the motivations of this thesis in the context of climate crisis that we are living, and the urgent need for greenhouse gas mitigation was discussed, considering plasma-catalysis for CO_2 utilization as a promosing route. The chapter introduced the concept of plasma-catalysis, emphasizing the potential synergies between non-thermal plasmas and heterogeneous catalysts. A critical review of the literature on plasma-catalytic DRM highlighted the research gaps, particularly the lack of studies using nanosecond repetitively pulsed (NRP) discharges, setting the stage for the thesis objectives.

In **chapter 4** a detailed description of the experimental techniques and analytical methods used throughout the thesis was presented. It covered a wide range of catalyst characterization techniques, including XRD, FTIR, CO_2-TPD, N2 adsorption, and H2-TPR, emphasizing their importance in understanding catalyst properties and performance. The chapter also described the general reactor design for the NRP discharge, highlighting the challenges and solutions in creating a suitable environment for plasma-catalytic reactions. Particular attention was given to the electrical diagnostics of the NRP discharge and the analytical methods used to evaluate reaction performance, including gas chromatography and the Karl Fischer technique. This comprehensive methodology chapter ensured reproducibility and provided a solid foundation for the experimental work presented in subsequent chapters.

In **chapter 5** we explored the use of Ni-based powder catalysts in a post-plasma configuration with the NRP discharge. Despite thorough catalyst selection from the literature review and a precise characterisation, no significant enhancement in DRM performance was observed compared to plasma-alone conditions. This result highlighted the challenges of achieving effective plasma-catalyst synergy in post-plasma configurations, likely due to the short lifetimes of reactive plasma species. While the initial hypothesis was not confirmed, these findings were crucial in guiding the subsequent research directions, emphasising the need for alternative catalyst placement strategies.

In **chapter 6** we introduced monolith foam catalysts in a co-axial configuration to bring the catalyst closer to the plasma discharge. The study demonstrated improved CO_2 and CH_4 conversions compared to plasma-alone conditions, with a linear increase in conversion as foam temperature increased and a shift in

products selectivities, registering a decrease in CO production and a shift towards acetylene over ethane and ethene. Interestingly, the composition of the foam (Al_2O_3 vs. $Y_2O_3-ZrO_2$) did not significantly affect performance, suggesting a primarily physical rather than chemical effect. However, the synthesis of the monolith foams is costly, it imposes strict restrictions to the choice of the catalyst material, and functionalisation of the surface needs further optimisation. The valuable insights provided by this chapter opened the way for a new co-axial configuration.

In **chapter 7** we introduced a novel quartz wool nest structure that combines the proximity advantages of foam catalysts with the flexibility of powder catalysts. This innovative design approximately doubled CO_2 and CH_4 conversions compared to plasma-alone conditions. The study also revealed an influence of the nest structure on product selectivities. The minimal differences observed between catalyst-loaded and support alone experiments highlighted the importance of physical confinement effects in plasma-catalytic systems. This chapter demonstrated the potential of tailored reactor designs in enhancing plasma-catalytic performance for DRM.

Overall, this thesis has advanced the understanding of plasma-catalytic DRM using NRP discharges. It has highlighted the complexities of plasma-catalyst interactions, demonstrated the importance of reactor and catalyst design, and opened new routes for the development of plasma-catalytic systems for CO_2 utilisation.

Future work might benefit from the development and implementation of in-situ diagnostics techniques to better understand the plasma-catalytic interface, including species lifetimes, surface reactions and local temperature effects. The work of Garcia Soto on *in situ* FTIR transmission on CeO_2 pellets in fluidised bed is a good example in this direction.

In order to study the physical effects brought by the co-axial catalytic structures, such as temperature modulation and altered gas dynamics, fluido-dynamic models of this configuration can be developed. This would help the understanding of the leading mechanisms at play and improve plasma reactor and catalyst design.

Acknowledgements

Appendix A

Determination of the spurious delay τ

We will describe here the calibration procedure to determine the spurious delay τ between the voltage signal V(t) and the current signal I(t) for the NRP discharge setup in Trento. An in-depth discussion of this procedure can be found in the doctoral work of Montesano [140]. His results are summarized here.

To estimate τ, the voltage and current signals need to be measured in a purely reactive load configuration, rather than resistive. This happens when a breakdown of the discharge is prevented, and only reactive power is transmitted between the electrodes. As a consequence, the measured conduction current $I_m(t)$ is the same as the displacement current $I_d(t)$:

$$I_m(t) = I_d(t) = C \cdot \frac{dV(t-\tau)}{dt} \tag{A.1}$$

where C represents the total capacitance of the system, resulting from the reactor and probes.

As a consequence of this scenario, the energy calculated with equation (4.41) should be zero over the pulse interval. By shifting the voltage signal V(t) with respect to I(t) to bring the resulting pulse energy to zero, τ can be determined. Furthermore, the system's total capacitance can be estimated from traces acquired without breakdown.

To include potential inductive contributions, the zero-crossing of the energy of the pulse can be studied as a function of the time shift between I(t) and V(t). The secant method was used to minimize E_p. The resulting total capacitance and spurious delay are reported here:

$$C_{fit} = (20.76 \pm 0.04)pF \tag{A.2}$$

$$\tau_{fit} = (0.47 \pm 0,03)ns \tag{A.3}$$

Experimentally, absence of breakdown can be achieved by filling the reactor chamber with a substance causing a breakdown voltage high enough, that the discharge cannot be ignited. In our case, the reactor was filled with 500 mbar of Freon-113 and 500 mbar of air.

Appendix B

Measure of system characteristic response time

The ignition of a plasma discharge provokes a sudden change in the gas mixture in the reactor that must be registered downstream by our analytical system. We performed a test to estimate the characteristic time it takes for our μGC to converge to the changed analyte peak area. For the test we set short, 1 min distanced analyzes on the μGC continuously running and flew 300 sccm of CO2 in the reactor. At time t = 0, we switched off the CO2 flow and injected an equal amount of N2 in the line, to keep the flow and pressure in the reactor constant. Every minute, a μGC analysis registered the CO2 peak area in a chromatogram. As shown in Figure 1.3, this area is plotted versus time and fitted with the exponential function $e^{(-t/\tau)}$, to determine the characteristic response time of the system, τ. A time of 5τ, corresponding to 7,7 minutes, is established as the initial time between the ignition of the discharge and the start of the μGC analysis.

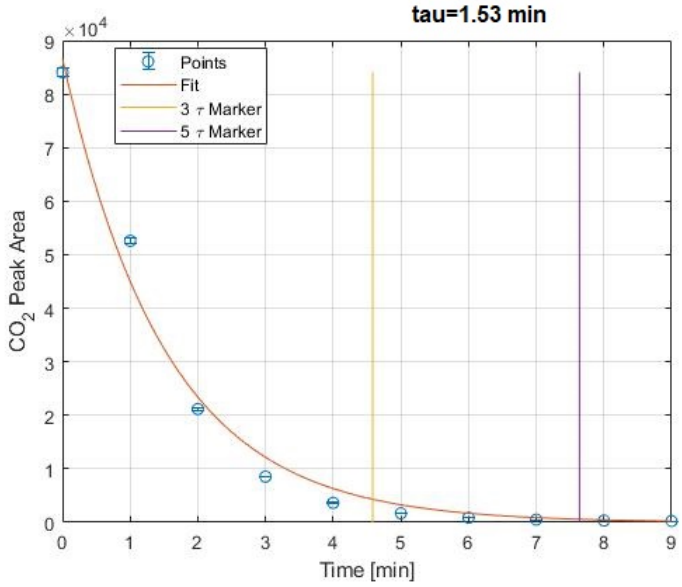

Figure B.1. Determination of the system characteristic response time.

List of Figures

List of Abbreviations

µGC micro Gas Chromatographer. 48, 52

BET Brunauer Emmett Teller. 59

BJH Barrett Joyner Halenda. 59

BW bandwidth. 44, 47

CAD Computer-Aided Design. v, 45

CCUS Carbon capture, utilisation and storage. iv, 5

DBD Dielectric Barrier Discharge. 16

DRIFT Diffuse Reflectance Infrared Fourier Transform. 63

DRM Dry Reforming of Methane. 10, 52, 77

ECN Effective Carbon Number. 49

EDS Energy Dispersive Spectroscopy. 34

EMI electro magnetic interference. 45, 47

EU European Union. 5

FID Flame Ionization Detector. 49

FTIR Fourier-transform infrared spectroscopy. 59

FWHM Full Width at Half Maximum. 54, 55

GHG Greenhouse gas. 3

IPC in-plasma catalysis. iv, 24

IS Internal Standard. 52

IWI Incipient Wetness Impregnation. 62, 68

MACOR Machinable Glass Ceramic For Industrial Applications. 46, 47, 73, 74, 86

NPG nanosecond pulse generator. 44

NRP Nanosecond Repetitively Pulsed. v, vi, 33, 44, 45, 54–57, 71, 77

NTPs Non-thermal plasmas. 15

RWGS Reverse Water-Gas Shift. 10, 11

SEI Specific Energy Input. 54, 57, 74, 77

SEM Scanning Electron Microscopy. 34

SSA Specific Surface Area. 64

STP Standard Temperature and Pressure. 54

TRL Technology Readiness Level. 6

WGSR Water-Gas Shift Reaction. 6, 10

XPS X-ray photoelectron spectroscopy. 39, 40

XRD X-ray diffraction. 38, 59

Bibliography

[1] R. Dębek, M. Motak, D. Duraczyska, F. Launay, M. E. Galvez, T. Grzybek, and P. D. Costa, "Methane dry reforming over hydrotalcite-derived Ni–Mg–Al mixed oxides: the influence of Ni content on catalytic activity, selectivity and stability," *Catalysis Science & Technology*, vol. 6, pp. 6705–6715, Aug. 2016. Publisher: The Royal Society of Chemistry.

[2] Intergovernmental Panel on Climate Change (IPCC), *Climate Change 2021 – The Physical Science Basis: Working Group I Contribution to the Sixth Assessment Report of the Intergovernmental Panel on Climate Change*. Cambridge: Cambridge University Press, 2023.

[3] I. E. A. IEA, "CO2 Emissions in 2023 – IEA, Paris."

[4] N. G. C. Change, "Carbon Dioxide Concentration | NASA Global Climate Change."

[5] H. Ritchie, P. Rosado, and M. Roser, "CO2 and Greenhouse Gas Emissions," Dec. 2023.

[6] I. E. A. IEA, "Global Methane Tracker 2024 – Analysis."

[7] B. Metz, O. Davidson, H. de Coninck, M. Loos, and L. Meyer, eds., *Sources of CO2*. Cambridge University Press, UK, 2005.

[8] H. Ritchie and P. Rosado, "Electricity mix," *Our World in Data*, 2020. https://ourworldindata.org/electricity-mix.

[9] A. Dubey and A. Arora, "Advancements in carbon capture technologies: A review," *Journal of Cleaner Production*, vol. 373, p. 133932, Nov. 2022.

[10] M. Bui, C. S. Adjiman, A. Bardow, E. J. Anthony, A. Boston, S. Brown, P. S. Fennell, S. Fuss, A. Galindo, L. A. Hackett, J. P. Hallett, H. J. Herzog, G. Jackson, J. Kemper, S. Krevor, G. C. Maitland, M. Matuszewski, I. S. Metcalfe, C. Petit, G. Puxty, J. Reimer, D. M. Reiner, E. S. Rubin, S. A. Scott, N. Shah, B. Smit, J. P. M. Trusler, P. Webley, J. Wilcox, and N. M. Dowell, "Carbon capture and storage (CCS): the way forward," *Energy & Environmental Science*, vol. 11, pp. 1062–1176, May 2018. Publisher: The Royal Society of Chemistry.

[11] M. K. Mondal, H. K. Balsora, and P. Varshney, "Progress and trends in CO2 capture/separation technologies: A review," *Energy*, vol. 46, pp. 431–441, Oct. 2012.

[12] M. E. Boot-Handford, J. C. Abanades, E. J. Anthony, M. J. Blunt, S. Brandani, N. Mac Dowell, J. R. Fernández, M.-C. Ferrari, R. Gross, J. P. Hallett, R. S. Haszeldine, P. Heptonstall, A. Lyngfelt, Z. Makuch, E. Mangano, R. T. J. Porter, M. Pourkashanian, G. T. Rochelle, N. Shah, J. G. Yao, and P. S. Fennell, "Carbon capture and storage update," *Energy Environ. Sci.*, vol. 7, pp. 130–189, 2014.

[13] E. Rubin, J. C. Abanades, M. Akai, S. Benson, D. Keith, M. Mazzotti, B. Metz, B. Osman-Elasha, A. Palmer, K. Smekens, and M. Soltanieh, "Technical Summary," in *IPCC Special Report on Carbon dioxide Capture and Storage*, Cambridge University Press, UK, 2005.

[14] L. Brennan and P. Owende, "Biofuels from microalgae—A review of technologies for production, processing, and extractions of biofuels and co-products," *Renewable and Sustainable Energy Reviews*, vol. 14, pp. 557–577, Feb. 2010.

[15] K. Rabaey and R. A. Rozendal, "Microbial electrosynthesis — revisiting the electrical route for microbial production," *Nature Reviews Microbiology*, vol. 8, pp. 706–716, Oct. 2010. Publisher: Nature Publishing Group.

[16] C. Paulo, I. M. Power, A. R. Stubbs, B. Wang, N. Zeyen, and S. Wilson, "Evaluating feedstocks for carbon dioxide removal by enhanced rock weathering and co2 mineralization," *Applied Geochemistry*, vol. 129, p. 104955, 2021.

[17] N. Li, L. Mo, and C. Unluer, "Emerging co2 utilization technologies for construction materials: A review," *Journal of CO2 Utilization*, vol. 65, p. 102237, 2022.

[18] B. Jia, J.-S. Tsau, and R. Barati, "A review of the current progress of co2 injection eor and carbon storage in shale oil reservoirs," *Fuel*, vol. 236, pp. 404–427, 2019.

[19] P. Olasolo, M. Juárez, M. Morales, I. Liarte, *et al.*, "Enhanced geothermal systems (egs): A review," *Renewable and Sustainable Energy Reviews*, vol. 56, pp. 133–144, 2016.

[20] C. Fernández-Dacosta, V. Stojcheva, and A. Ramirez, "Closing carbon cycles: Evaluating the performance of multi-product CO2 utilisation and storage configurations in a refinery," *Journal of CO2 Utilization*, vol. 23, pp. 128–142, Jan. 2018.

[21] W. Wang, S. Wang, X. Ma, and J. Gong, "Recent advances in catalytic hydrogenation of carbon dioxide," *Chemical Society Reviews*, vol. 40, pp. 3703–3727, June 2011. Publisher: The Royal Society of Chemistry.

[22] A. I. Tsiotsias, N. D. Charisiou, I. V. Yentekakis, and M. A. Goula, "Bimetallic ni-based catalysts for co2 methanation: a review," *Nanomaterials*, vol. 11, no. 1, p. 28, 2020.

[23] N. Rui, X. Zhang, F. Zhang, Z. Liu, X. Cao, Z. Xie, R. Zou, S. D. Senanayake, Y. Yang, J. A. Rodriguez, *et al.*, "Highly active ni/ceo2 catalyst for co2 methanation: Preparation and characterization," *Applied Catalysis B: Environmental*, vol. 282, p. 119581, 2021.

[24] L. Li, W. Zeng, M. Song, X. Wu, G. Li, and C. Hu, "Research progress and reaction mechanism of co2 methanation over ni-based catalysts at low temperature: a review," *Catalysts*, vol. 12, no. 2, p. 244, 2022.

[25] S. Chai, Y. Men, J. Wang, S. Liu, Q. Song, W. An, and G. Kolb, "Boosting co2 methanation activity on ru/tio2 catalysts by exposing (001) facets of anatase tio2," *Journal of CO2 Utilization*, vol. 33, pp. 242–252, 2019.

[26] H. Arandiyan, K. Kani, Y. Wang, B. Jiang, J. Kim, M. Yoshino, M. Rezaei, A. E. Rowan, H. Dai, and Y. Yamauchi, "Highly selective reduction of carbon dioxide to methane on novel mesoporous rh catalysts," *ACS applied materials & interfaces*, vol. 10, no. 30, pp. 24963–24968, 2018.

[27] H. Jiang, Q. Gao, S. Wang, Y. Chen, and M. Zhang, "The synergistic effect of pd nps and uio-66 for enhanced activity of carbon dioxide methanation," *Journal of CO2 Utilization*, vol. 31, pp. 167–172, 2019.

[28] J. Ashok, S. Pati, P. Hongmanorom, Z. Tianxi, C. Junmei, and S. Kawi, "A review of recent catalyst advances in co2 methanation processes," *Catalysis Today*, vol. 356, pp. 471–489, 2020.

[29] G. A. Olah, A. Goeppert, and G. S. Prakash, *Beyond oil and gas: the methanol economy*. John Wiley & Sons, 2011.

[30] R. Guil-López, N. Mota, J. Llorente, E. Millán, B. Pawelec, J. Fierro, and R. Navarro, "Methanol synthesis from co2: a review of the latest developments in heterogeneous catalysis," *Materials*, vol. 12, no. 23, p. 3902, 2019.

[31] V. Ipatieff and G. Monroe, "Synthesis of methanol from carbon dioxide and hydrogen over copper-alumina catalysts. mechanism of reaction," *Journal of the American Chemical Society*, vol. 67, no. 12, pp. 2168–2171, 1945.

[32] S. Kuld, M. Thorhauge, H. Falsig, C. F. Elkjær, S. Helveg, I. Chorkendorff, and J. Sehested, "Quantifying the promotion of cu catalysts by zno for methanol synthesis," *Science*, vol. 352, no. 6288, pp. 969–974, 2016.

[33] M. González-Castaño, B. Dorneanu, and H. Arellano-García, "The reverse water gas shift reaction: a process systems engineering perspective," *Reaction Chemistry & Engineering*, vol. 6, no. 6, pp. 954–976, 2021.

[34] M. Liu, Y. Yi, L. Wang, H. Guo, and A. Bogaerts, "Hydrogenation of carbon dioxide to value-added chemicals by heterogeneous catalysis and plasma catalysis," *Catalysts*, vol. 9, no. 3, p. 275, 2019.

[35] A. Goguet, F. Meunier, J. Breen, R. Burch, M. Petch, and A. Faur Ghenciu, "Study of the origin of the deactivation of a pt/ceo2 catalyst during reverse water gas shift (rwgs) reaction," *Journal of Catalysis*, vol. 226, no. 2, pp. 382–392, 2004.

[36] J. Ding, R. Ye, Y. Fu, Y. He, Y. Wu, Y. Zhang, Q. Zhong, H. H. Kung, and M. Fan, "Direct synthesis of urea from carbon dioxide and ammonia," *Nature Communications*, vol. 14, p. 4586, July 2023.

[37] F. Barzagli, F. Mani, and M. Peruzzini, "From greenhouse gas to feedstock: formation of ammonium carbamate from co2 and nh3 in organic solvents and its catalytic conversion into urea under mild conditions," *Green chemistry*, vol. 13, no. 5, pp. 1267–1274, 2011.

[38] A. de Klerk, "Chapter 12 - transport fuel: Biomass-, coal-, gas- and waste-to-liquids processes," in *Future Energy (Second Edition)* (T. M. Letcher, ed.), pp. 245–270, Boston: Elsevier, second edition ed., 2014.

[39] E. le Saché and T. R. Reina, "Analysis of Dry Reforming as direct route for gas phase CO2 conversion. The past, the present and future of catalytic DRM technologies," *Progress in Energy and Combustion Science*, vol. 89, p. 100970, Mar. 2022.

[40] M. K. Nikoo and N. Amin, "Thermodynamic analysis of carbon dioxide reforming of methane in view of solid carbon formation," *Fuel Processing Technology*, vol. 92, no. 3, pp. 678–691, 2011.

[41] R. Chein, Y. Chen, C. Yu, and J. Chung, "Thermodynamic analysis of dry reforming of ch4 with co2 at high pressures," *Journal of Natural Gas Science and Engineering*, vol. 26, pp. 617–629, 2015.

[42] R.-Y. Chein and W.-H. Hsu, "Thermodynamic analysis of syngas production via chemical looping dry reforming of methane," *Energy*, vol. 180, pp. 535–547, 2019.

[43] C. Jensen and M. S. Duyar, "Thermodynamic analysis of dry reforming of methane for valorization of landfill gas and natural gas," *Energy Technology*, vol. 9, no. 7, p. 2100106, 2021.

[44] R. Dębek, *Novel catalysts for chemical CO2 utilization*. PhD thesis, AGH University of Science and Technology, 2016.

[45] A. G. S. Hussien and K. Polychronopoulou, "A review on the different aspects and challenges of the dry reforming of methane (drm) reaction," *Nanomaterials*, vol. 12, no. 19, 2022.

[46] P. Summa, B. Samojeden, and M. Motak, "Dry and steam reforming of methane. Comparison and analysis of recently investigated catalytic materials. A short review.," *Polish Journal of Chemical Technology*, vol. 21, pp. 31–37, June 2019.

[47] Z. Li, Q. Lin, M. Li, J. Cao, F. Liu, H. Pan, Z. Wang, and S. Kawi, "Recent advances in process and catalyst for co2 reforming of methane," *Renewable and Sustainable Energy Reviews*, vol. 134, p. 110312, 2020.

[48] I. V. Yentekakis, P. Panagiotopoulou, and G. Artemakis, "A review of recent efforts to promote dry reforming of methane (drm) to syngas production via bimetallic catalyst formulations," *Applied Catalysis B: Environmental*, vol. 296, p. 120210, 2021.

[49] T. Reina and E. le Saché, "Analysis of dry reforming as direct route for gas phase co2 conversion. the past, the present and future of catalytic drm technologies," *Progress in Energy and Combustion Science*, 2022.

[50] S. Andraos, R. Abbas-Ghaleb, D. Chlala, A. Vita, C. Italiano, M. Laganà, L. Pino, M. Nakhl, and S. Specchia, "Production of hydrogen by methane dry reforming over ruthenium-nickel based catalysts deposited on al2o3, mgal2o4, and ysz," *international journal of hydrogen energy*, vol. 44, no. 47, pp. 25706–25716, 2019.

[51] M. Usman, W. W. Daud, and H. F. Abbas, "Dry reforming of methane: Influence of process parameters—a review," *Renewable and Sustainable Energy Reviews*, vol. 45, pp. 710–744, 2015.

[52] X. Zhang, L. Zhang, H. Peng, X. You, C. Peng, X. Xu, W. Liu, X. Fang, Z. Wang, N. Zhang, *et al.*, "Nickel nanoparticles embedded in mesopores of alsba-15 with a perfect peasecod-like structure: A catalyst with superior sintering resistance and hydrothermal stability for methane dry reforming," *Applied Catalysis B: Environmental*, vol. 224, pp. 488–499, 2018.

[53] R. Dębek, M. Motak, M. E. Galvez, P. Da Costa, and T. Grzybek, "Catalytic activity of hydrotalcite-derived catalysts in the dry reforming of methane: on the effect of ce promotion and feed gas composition," *Reaction kinetics, mechanisms and catalysis*, vol. 121, pp. 185–208, 2017.

[54] K. Świrk, M. Motak, T. Grzybek, M. Rønning, and P. Da Costa, "Effect of low loading of yttrium on ni-based layered double hydroxides in co 2 reforming of ch 4," *Reaction kinetics, mechanisms and catalysis*, vol. 126, pp. 611–628, 2019.

[55] M. Akri, S. Zhao, X. Li, K. Zang, A. F. Lee, M. A. Isaacs, W. Xi, Y. Gangarajula, J. Luo, Y. Ren, *et al.*, "Atomically dispersed nickel as coke-resistant active sites for methane dry reforming," *Nature communications*, vol. 10, no. 1, p. 5181, 2019.

[56] Z. Shang, S. Li, L. Li, G. Liu, and X. Liang, "Highly active and stable alumina supported nickel nanoparticle catalysts for dry reforming of methane," *Applied Catalysis B: Environmental*, vol. 201, pp. 302–309, 2017.

[57] A. Fridman, *Plasma chemistry*. Cambridge university press, 2008.

[58] A. Milella and F. Palumbo, "Cold plasma," in *Encyclopedia of Membranes* (E. Drioli and L. Giorno, eds.), pp. 1–2, Springer Berlin Heidelberg.

[59] R. Snoeckx and A. Bogaerts, "Plasma technology – a novel solution for CO_2 conversion?," *Chemical Society Reviews*, vol. 46, no. 19, pp. 5805–5863, 2017.

[60] C. Montesano, S. Quercetti, L. M. Martini, G. Dilecce, and P. Tosi, "The effect of different pulse patterns on the plasma reduction of co2 for a nanosecond discharge," *Journal of CO2 Utilization*, vol. 39, p. 101157, 2020.

[61] S. Starikovskaia, "Plasma-assisted ignition and combustion: nanosecond discharges and development of kinetic mechanisms," *Journal of Physics D: Applied Physics*, vol. 47, no. 35, p. 353001, 2014.

[62] A. Starikovskiy and N. Aleksandrov, "Plasma-assisted ignition and combustion," *Progress in Energy and Combustion Science*, vol. 39, no. 1, pp. 61–110, 2013.

[63] F. Iza, J. L. Walsh, and M. G. Kong, "From submicrosecond- to nanosecond-pulsed atmospheric-pressure plasmas," *IEEE Transactions on Plasma Science*, vol. 37, no. 7, pp. 1289–1296, 2009.

[64] D. Rusterholtz, *Nanosecond repetitively pulsed discharges in atmospheric pressure air*. PhD thesis, Ecole Centrale Paris, 2012.

[65] C. Montesano, T. P. Salden, L. M. Martini, G. Dilecce, and P. Tosi, "Co2 reduction by nanosecond-plasma discharges: revealing the dissociation's time scale and the importance of pulse sequence," *The Journal of Physical Chemistry C*, vol. 127, no. 21, pp. 10045–10050, 2023.

[66] C. Montesano, M. Faedda, L. M. Martini, G. Dilecce, and P. Tosi, "CH4 reforming with CO2 in a nanosecond pulsed discharge. The importance of the pulse sequence," *Journal of CO2 Utilization*, vol. 49, p. 101556, July 2021.

[67] E. C. Neyts, K. K. Ostrikov, M. K. Sunkara, and A. Bogaerts, "Plasma Catalysis: Synergistic Effects at the Nanoscale," *Chemical Reviews*, vol. 115, pp. 13408–13446, Dec. 2015. Publisher: American Chemical Society.

[68] J. C. Whitehead, "Plasma–catalysis: the known knowns, the known unknowns and the unknown unknowns," *Journal of Physics D: Applied Physics*, vol. 49, p. 243001, may 2016.

[69] A. Bogaerts, X. Tu, J. C. Whitehead, G. Centi, L. Lefferts, O. Guaitella, F. Azzolina-Jury, H.-H. Kim, A. B. Murphy, W. F. Schneider, T. Nozaki, J. C. Hicks, A. Rousseau, F. Thevenet, A. Khacef, and M. Carreon, "The 2020 plasma catalysis roadmap," *Journal of Physics D: Applied Physics*, vol. 53, p. 443001, Aug. 2020. Publisher: IOP Publishing.

[70] J. Sun, Q. Chen, W. Qin, H. Wu, B. Liu, S. Li, and A. Bogaerts, "Plasma-catalytic dry reforming of CH4: Effects of plasma-generated species on the surface chemistry," *Chemical Engineering Journal*, vol. 498, p. 155847, Oct. 2024.

[71] A. Salden, M. Budde, C. A. Garcia-Soto, O. Biondo, J. Barauna, M. Faedda, B. Musig, C. Fromentin, M. Nguyen-Quang, H. Philpott, G. Hasrack, D. Aceto, Y. Cai, F. A. Jury, A. Bogaerts, P. Da Costa, R. Engeln, M. E. Gálvez, T. Gans, T. Garcia, V. Guerra, C. Henriques, M. Motak, M. V. Navarro, V. I. Parvulescu, G. Van Rooij, B. Samojeden, A. Sobota, P. Tosi, X. Tu, and O. Guaitella, "Meta-analysis of CO2 conversion, energy efficiency, and other performance data of plasma-catalysis reactors with the open access PIONEER database," *Journal of Energy Chemistry*, vol. 86, pp. 318–342, Nov. 2023.

[72] A. George, B. Shen, M. Craven, Y. Wang, D. Kang, C. Wu, and X. Tu, "A Review of Non-Thermal Plasma Technology: A novel solution for CO2 conversion and utilization," *Renewable and Sustainable Energy Reviews*, vol. 135, p. 109702, Jan. 2021.

[73] C. Richards, E. Jans, D. Mignogna, and I. V. Adamovich, "Time-resolved CO2, CO, and N2 vibrational population measurements in Ns pulse discharge plasmas," *Plasma Sources Science and Technology*, vol. 31, p. 094011, Oct. 2022. Publisher: IOP Publishing.

[74] L. M. Martini, N. Gatti, G. Dilecce, M. Scotoni, and P. Tosi, "Laser induced fluorescence in nanosecond repetitively pulsed discharges for CO2 conversion," *Plasma Physics and Controlled Fusion*, vol. 60, p. 014016, Oct. 2017. Publisher: IOP Publishing.

[75] A. Bogaerts and G. Centi, "Plasma technology for CO2 conversion: A personal perspective on prospects and gaps," *Frontiers in Energy Research*, vol. 8, p. 111, 2020.

[76] R. Snoeckx, R. Aerts, X. Tu, and A. Bogaerts, "Plasma-Based Dry Reforming: A Computational Study Ranging from the Nanoseconds to Seconds Time Scale," *The Journal of Physical Chemistry C*, vol. 117, pp. 4957–4970, Mar. 2013.

[77] Z. A. Allah and J. C. Whitehead, "Plasma-catalytic dry reforming of methane in an atmospheric pressure AC gliding arc discharge," *Catalysis Today*, vol. 256, pp. 76–79, nov 2015.

[78] A. Aziznia, H. R. Bozorgzadeh, N. Seyed-Matin, M. Baghalha, and A. Mohamadalizadeh, "Comparison of dry reforming of methane in low temperature hybrid plasma-catalytic corona with thermal catalytic reactor over ni/γ-al2o3," *Journal of Natural Gas Chemistry*, vol. 21, pp. 466–475, jul 2012.

[79] N. Bouchoul, H. Touati, E. Fourré, J.-M. Clacens, and C. Batiot-Dupeyrat, "Efficient plasma-catalysis coupling for CH4 and CO2 transformation in a fluidized bed reactor: Comparison with a fixed bed reactor," *Fuel*, vol. 288, p. 119575, mar 2021.

[80] Y. Diao, H. Wang, B. Chen, L. Wang, X. Zhang, and C. Shi, "Ordered mesoporous ni-la2o3/al2o3 catalysts towards efficient plasma-assisted dry reforming of methane," *Fuel Processing Technology*, vol. 243, p. 107676, May 2023.

[81] L. Dou, Y. Liu, Y. Gao, J. Li, X. Hu, S. Zhang, K. K. Ostrikov, and T. Shao, "Disentangling metallic cobalt sites and oxygen vacancy effects in synergistic plasma-catalytic co2/ch4 conversion into oxygenates," *Applied Catalysis B: Environmental*, vol. 318, p. 121830, Dec. 2022.

[82] B. Eliasson, C. jun Liu, and U. Kogelschatz, "Direct conversion of methane and carbon dioxide to higher hydrocarbons using catalytic dielectric-barrier discharges with zeolites," *Industrial & Engineering Chemistry Research*, vol. 39, pp. 1221–1227, apr 2000.

[83] H. J. Gallon, X. Tu, and J. C. Whitehead, "Effects of reactor packing materials on h2 production by CO2 reforming of CH4 in a dielectric barrier discharge," *Plasma Processes and Polymers*, vol. 9, pp. 90–97, nov 2011.

[84] A. H. Khoja, M. Tahir, N. A. S. Amin, A. Javed, and M. T. Mehran, "Kinetic study of dry reforming of methane using hybrid DBD plasma reactor over la2o3 co-supported ni/MgAl2o4 catalyst," *International Journal of Hydrogen Energy*, vol. 45, no. 22, pp. 12256–12271, 2020.

[85] T. Kroker, T. Kolb, A. Schenk, K. Krawczyk, M. Młotek, and K.-H. Gericke, "Catalytic conversion of simulated biogas mixtures to synthesis gas in a fluidized bed reactor supported by a DBD," *Plasma Chemistry and Plasma Processing*, vol. 32, pp. 565–582, mar 2012.

[86] M.-W. Li, C.-P. Liu, Y.-L. Tian, G.-H. Xu, F.-C. Zhang, and Y.-Q. Wang, "Effects of catalysts in carbon dioxide reforming of methane via corona plasma reactions," *Energy & Fuels*, vol. 20, pp. 1033–1038, mar 2006.

[87] Y. Li, H. Yu, J. Dai, Z. Zhang, Z. Zhang, H. Yu, and L. Liu, "Ch4 and co2 conversion over boron nitride-supported ni catalysts with b o defects in dbd plasma," *Fuel Processing Technology*, vol. 242, p. 107655, Apr. 2023.

[88] H. LONG, S. SHANG, X. TAO, Y. YIN, and X. DAI, "CO2 reforming of CH4 by combination of cold plasma jet and ni/γ-al2o3 catalyst," *International Journal of Hydrogen Energy*, vol. 33, pp. 5510–5515, oct 2008.

[89] H. M. Nguyen, N. M. Alawi, and L. Nguyen-Dinh, "Inductively-coupled plasma for co2 conversion to syngas over cu/al2o3 catalyst," in *THIRD VIRTUAL INTERNATIONAL CONFERENCE ON MATERIALS, MANUFACTURING AND NANOTECHNOLOGY*, AIP Publishing, 2022.

[90] K. L. Pan, W. C. Chung, and M. B. Chang, "Dry reforming of CH4 with CO2 to generate syngas by combined plasma catalysis," *IEEE Transactions on Plasma Science*, vol. 42, pp. 3809–3818, dec 2014.

[91] M. Pham, V. Goujard, J. Tatibouët, and C. Batiot-Dupeyrat, "Activation of methane and carbon dioxide in a dielectric-barrier discharge-plasma reactor to produce hydrocarbons—influence of la2o3/γ-al2o3 catalyst," *Catalysis Today*, vol. 171, pp. 67–71, aug 2011.

[92] D. Ray, P. M. K. Reddy, and S. Challapalli, "Glass beads packed DBD-plasma assisted dry reforming of methane," *Topics in Catalysis*, vol. 60, pp. 869–878, apr 2017.

[93] D. Ray, P. M. K. Reddy, and C. Subrahmanyam, "Ni-mn/γ-al2o3 assisted plasma dry reforming of methane," *Catalysis Today*, vol. 309, pp. 212–218, jul 2018.

[94] H. K. Song, J.-W. Choi, S. H. Yue, H. Lee, and B.-K. Na, "Synthesis gas production via dielectric barrier discharge over ni/γ-al2o3 catalyst," *Catalysis Today*, vol. 89, pp. 27–33, feb 2004.

[95] X. Tu, H. J. Gallon, M. V. Twigg, P. A. Gorry, and J. C. Whitehead, "Dry reforming of methane over a ni/al2o3 catalyst in a coaxial dielectric barrier discharge reactor," *Journal of Physics D: Applied Physics*, vol. 44, p. 274007, jun 2011.

[96] X. Tu and J. Whitehead, "Plasma-catalytic dry reforming of methane in an atmospheric dielectric barrier discharge: Understanding the synergistic effect at low temperature," *Applied Catalysis B: Environmental*, vol. 125, pp. 439–448, aug 2012.

[97] Q. Wang, Y. Cheng, and Y. Jin, "Dry reforming of methane in an atmospheric pressure plasma fluidized bed with ni/γ-al2o3 catalyst," *Catalysis Today*, vol. 148, pp. 275–282, nov 2009.

[98] L. Wang, Y. Yi, C. Wu, H. Guo, and X. Tu, "One-step reforming of CO2 and CH4 into high-value liquid chemicals and fuels at room temperature by plasma-driven catalysis," *Angewandte Chemie*, vol. 129, pp. 13867–13871, sep 2017.

[99] H. Wang, J. Han, Z. Bo, L. Qin, Y. Wang, and F. Yu, "Non-thermal plasma enhanced dry reforming of CH4 with CO2 over activated carbon supported ni catalysts," *Molecular Catalysis*, vol. 475, p. 110486, oct 2019.

[100] H. Wang, B. Zhao, L. Qin, Y. Wang, F. Yu, and J. Han, "Non-thermal plasma-enhanced dry reforming of methane and CO2 over ce-promoted ni/c catalysts," *Molecular Catalysis*, vol. 485, p. 110821, apr 2020.

[101] Y. Zeng, X. Zhu, D. Mei, B. Ashford, and X. Tu, "Plasma-catalytic dry reforming of methane over γ-al2o3 supported metal catalysts," *Catalysis Today*, vol. 256, pp. 80–87, nov 2015.

[102] X.-G. Zheng, S.-Y. Tan, L.-C. Dong, S.-B. Li, H.-M. Chen, and S.-A. Wei, "Experimental and kinetic investigation of the plasma catalytic dry reforming of methane over perovskite LaNiO3 nanoparticles," *Fuel Processing Technology*, vol. 137, pp. 250–258, sep 2015.

[103] W.-C. Chung and M.-B. Chang, "Dry reforming of methane by combined spark discharge with a ferroelectric," *Energy Conversion and Management*, vol. 124, pp. 305–314.

[104] W. Xu, L. C. Buelens, V. V. Galvita, A. Bogaerts, and V. Meynen, "Improving the performance of gliding arc plasma-catalytic dry reforming via a new post-plasma tubular catalyst bed," *Journal of CO2 Utilization*, vol. 83, p. 102820.

[105] H. Long, S. Shang, X. Tao, Y. Yin, and X. Dai, "CO2 reforming of CH4 by combination of cold plasma jet and ni/γ-al2o3 catalyst," *International Journal of Hydrogen Energy*, vol. 33, no. 20, pp. 5510–5515.

[106] K. Li, J.-L. Liu, X.-S. Li, X.-B. Zhu, and A.-M. Zhu, "Post-plasma catalytic oxidative CO2 reforming of methane over ni-based catalysts," *Catalysis Today*, vol. 256, pp. 96–101, 2015.

[107] X. Tu and J. Whitehead, "Plasma-catalytic dry reforming of methane in an atmospheric dielectric barrier discharge: Understanding the synergistic effect at low temperature," *Applied Catalysis B: Environmental*, vol. 125, pp. 439–448, 2012.

[108] W. Wang, H.-H. Kim, K. Van Laer, and A. Bogaerts, "Streamer propagation in a packed bed plasma reactor for plasma catalysis applications," *Chemical Engineering Journal*, vol. 334, pp. 2467–2479, 2018.

[109] X. Tu, H. J. Gallon, M. V. Twigg, P. A. Gorry, and J. C. Whitehead, "Dry reforming of methane over a Ni/Al $_2$ O $_3$ catalyst in a coaxial dielectric barrier discharge reactor," *Journal of Physics D: Applied Physics*, vol. 44, p. 274007, July 2011.

[110] L. Brune, A. Ozkan, E. Genty, T. Visart De Bocarmé, and F. Reniers, "Dry reforming of methane via plasma-catalysis: influence of the catalyst nature supported on alumina in a packed-bed DBD configuration," *Journal of Physics D: Applied Physics*, vol. 51, no. 23, p. 234002, 2018.

[111] X. Chen, Z. Sheng, S. Murata, S. Zen, H.-H. Kim, and T. Nozaki, "CH4 dry reforming in fluidized-bed plasma reactor enabling enhanced plasma-catalyst coupling," *Journal of CO2 Utilization*, vol. 54, p. 101771, 2021.

[112] D. Lasic Jurkovic, J.-L. Liu, A. Pohar, and B. Likozar, "Methane dry reforming over ni/al2o3 catalyst in spark plasma reactor: Linking computational fluid dynamics (CFD) with reaction kinetic modelling," *Catalysis Today*, vol. 362, pp. 11–21, 2021.

[113] X. Chen, H.-H. Kim, and T. Nozaki, "Plasma catalytic technology for CH4 and CO2 conversion: A review highlighting fluidized-bed plasma reactor," *Plasma Processes and Polymers*, vol. 21, no. 1, p. 2200207, 2024. _eprint: https://onlinelibrary.wiley.com/doi/pdf/10.1002/ppap.202200207.

[114] P. Hinde, V. Demidyuk, A. Gkelios, and C. Tipton, "Plasma catalysis: A review of the interdisciplinary challenges faced: Realising the potential of plasma catalysis on a commercial scale," *Johnson Matthey Technology Review*, vol. 64, no. 2, pp. 138–147, 2020. Publisher: Johnson Matthey.

[115] K. Krawczyk, M. Mlotek, B. Ulejczyk, and K. Schmidt-Szalowski, "Methane conversion with carbon dioxide in plasma-catalytic system," *Fuel*, vol. 117, pp. 608–617, 2014.

[116] D. Mei, M. Sun, S. Liu, P. Zhang, Z. Fang, and X. Tu, "Plasma-enabled catalytic dry reforming of CH4 into syngas, hydrocarbons and oxygenates: Insight into the active metals of γ-al2o3 supported catalysts," *Journal of CO2 Utilization*, vol. 67, p. 102307, 2023.

[117] X. Zhang, B. Dai, A. Zhu, W. Gong, and C. Liu, "The simultaneous activation of methane and carbon dioxide to c2 hydrocarbons under pulse corona plasma over la2o3/-al2o3 catalyst," *Catalysis Today*, 2002.

[118] L. M. Martini, S. Lovascio, G. Dilecce, and P. Tosi, "Time-resolved co 2 dissociation in a nanosecond pulsed discharge," *Plasma Chemistry and Plasma Processing*, vol. 38, pp. 707–718, 2018.

[119] M. Ceppelli, T. Salden, L. M. Martini, G. Dilecce, and P. Tosi, "Time-resolved optical emission spectroscopy in co2 nanosecond pulsed discharges," *Plasma Sources Science and Technology*, vol. 30, no. 11, p. 115010, 2021.

[120] D. A. Shirley, "High-Resolution X-Ray Photoemission Spectrum of the Valence Bands of Gold," *Physical Review B*, vol. 5, pp. 4709–4714, June 1972. Publisher: American Physical Society.

[121] "NIST national Institute of Standards and Technology." https://www.nist.gov/. Accessed: 25-07-2024.

[122] M. A. Isaacs, J. Davies-Jones, P. R. Davies, S. Guan, R. Lee, D. J. Morgan, and R. Palgrave, "Advanced XPS characterization: XPS-based multi-technique analyses for comprehensive understanding

of functional materials," *Materials Chemistry Frontiers*, vol. 5, no. 22, pp. 7931–7963, 2021. Publisher: The Royal Society of Chemistry.

[123] M. Ronda-Lloret, S. Rico-Francés, A. Sepúlveda-Escribano, and E. V. Ramos-Fernandez, "CuOx/CeO2 catalyst derived from metal organic framework for reverse water-gas shift reaction," *Applied Catalysis A: General*, vol. 562, pp. 28–36, 2018.

[124] A. M. Venezia, "X-ray photoelectron spectroscopy (XPS) for catalysts characterization," *Catalysis Today*, vol. 77, pp. 359–370, Jan. 2003.

[125] G. Speranza and R. Canteri, "RxpsG a new open project for Photoelectron and Electron Spectroscopy data processing," *SoftwareX*, vol. 10, p. 100282, July 2019.

[126] Q.-Z. Zhang and A. Bogaerts, "Propagation of a plasma streamer in catalyst pores," *Plasma Sources Science and Technology*, vol. 27, p. 035009, mar 2018.

[127] S. Brunauer, P. H. Emmett, and E. Teller, "Adsorption of gases in multimolecular layers," *Journal of the American Chemical Society*, vol. 60, no. 2, pp. 309–319, 1938.

[128] E. P. Barrett, L. G. Joyner, and P. P. Halenda, "The determination of pore volume and area distributions in porous substances. i. computations from nitrogen isotherms," *Journal of the American Chemical Society*, vol. 73, no. 1, pp. 373–380, 1951.

[129] C. R. Paul, *Introduction to Electromagnetic Compatibility*. John Wiley & Sons, Inc., 2 ed., 2006.

[130] T. Huiskamp, "Nanosecond pulsed streamer discharges Part I: Generation, source-plasma interaction and energy-efficiency optimization," *Plasma Sources Science and Technology*, vol. 29, p. 023002, Feb. 2020.

[131] "MACOR machinable glass ceramic." https://www.corning.com/emea/en/products/advanced-optics/product-materials/specialty-glass-and-glass-ceramics/glass-ceramics/macor.html? Accessed: 23-07-2024.

[132] V. Kotov and P. M. J. Koelman, "Plug flow reactor model of the plasma chemical conversion of CO2," *Plasma Sources Science and Technology*, vol. 28, p. 095002, Sept. 2019. Publisher: IOP Publishing.

[133] "Agilent GC detectors reference." https://www.agilent.com/cs/library/quickreference/public/quick-reference-gc-detectors-5994-4919en-agilent.pdf. Accessed: 23-07-2024.

[134] J. T. Scanlon and D. E. Willis, "Calculation of Flame Ionization Detector Relative Response Factors Using the Effective Carbon Number Concept," *Journal of Chromatographic Science*, vol. 23, pp. 333–340, Aug. 1985.

[135] J. Slemr, F. Slemr, H. D'Souza, and R. Partridge, "Study of the relative response factors of various gas chromatograph–flame ionisation detector systems for measurement of C2–C9 hydrocarbons in air," *Journal of Chromatography A*, vol. 1061, no. 1, pp. 75–84, 2004.

[136] K. Fischer, "Neues verfahren zur maßanalytischen bestimmung des wassergehaltes von flüssigkeiten und festen körpern," *Angewandte Chemie*, vol. 48, p. 394–396, Apr 1935.

[137] L. Thomas, "What is the difference between coulometric and volumetric titration?," Jul 2023.

[138] N. Pinhão, A. Moura, J. Branco, and J. Neves, "Influence of gas expansion on process parameters in non-thermal plasma plug-flow reactors: A study applied to dry reforming of methane," *International Journal of Hydrogen Energy*, vol. 41, pp. 9245–9255, June 2016.

[139] A. Khomenko, V. Podolsky, and X. Wang, "Different approaches of measuring high-voltage nanosecond pulses and power delivery in plasma systems," *Electrical Engineering*, vol. 103, pp. 57–66, Feb. 2021.

[140] C. Montesano, *Experimental investigation of nanosecond pulsed discharges for CO2 recycling*. PhD thesis, University of Trento, 2023.

[141] X. Gao, Z. Ge, G. Zhu, Z. Wang, J. Ashok, and S. Kawi, "Anti-coking and anti-sintering ni/al2o3 catalysts in the dry reforming of methane: recent progress and prospects," *Catalysts*, vol. 11, no. 8, p. 1003, 2021.

[142] Y. Diao, X. Zhang, Y. Liu, B. Chen, G. Wu, and C. Shi, "Plasma-assisted dry reforming of methane over mo2c-ni/al2o3 catalysts: effects of β-mo2c promoter," *Applied Catalysis B: Environmental*, vol. 301, p. 120779, 2022.

[143] F. Cavani, F. Trifirò, and A. Vaccari, "Hydrotalcite-type anionic clays: Preparation, properties and applications.," *Catalysis Today*, vol. 11, no. 2, pp. 173–301, 1991.

[144] F. Schüth, M. Hesse, and K. K. Unger, "Precipitation and Coprecipitation," in *Handbook of Heterogeneous Catalysis*, pp. 100–119, John Wiley & Sons, Ltd, 2008.

[145] J. T. Kloprogge and R. L. Frost, "Fourier Transform Infrared and Raman Spectroscopic Study of the Local Structure of Mg-, Ni-, and Co-Hydrotalcites," *Journal of Solid State Chemistry*, vol. 146, pp. 506–515, Sept. 1999.

[146] C. Zhong, X. Guo, D. Mao, S. Wang, G. Wu, and G. Lu, "Effects of alkaline-earth oxides on the performance of a CuO–ZrO_2 catalyst for methanol synthesis via CO_2 hydrogenation," *RSC Adv.*, vol. 5, pp. 52958–52965, 2015.

[147] G. V. Oliveira, V. de Macedo, E. A. Urquieta-González, Z. M. Magriotis, and C. A. Pereira, "Fe2O3/γ-Al2O3 and NiO/γ-Al2O3 catalysts for the selective catalytic oxidation of ammonia," *Catalysis Today*, p. 114991, Aug. 2024.

[148] K. Zhao, Z. Li, and L. Bian, "CO2 methanation and co-methanation of CO and CO2 over Mn-promoted Ni/Al2O3 catalysts," *Frontiers of Chemical Science and Engineering*, vol. 10, pp. 273–280, June 2016.

[149] O. D. Pavel, D. Tichit, and I.-C. Marcu, "Acido-basic and catalytic properties of transition-metal containing Mg–Al hydrotalcites and their corresponding mixed oxides," *Applied Clay Science*, vol. 61, pp. 52–58, June 2012.

[150] M. Scapinello, L. M. Martini, G. Dilecce, and P. Tosi, "Conversion of CH4 /CO2 by a nanosecond repetitively pulsed discharge," *Journal of Physics D: Applied Physics*, vol. 49, p. 075602, Jan. 2016. Publisher: IOP Publishing.

[151] K. Schwartzwalder and A. V. Somers, "Method of making porous ceramic articles," May 1963.

[152] A. R. Studart, U. T. Gonzenbach, E. Tervoort, and L. J. Gauckler, "Processing Routes to Macroporous Ceramics: A Review," *Journal of the American Ceramic Society*, vol. 89, no. 6, pp. 1771–1789, 2006. _eprint: https://onlinelibrary.wiley.com/doi/pdf/10.1111/j.1551-2916.2006.01044.x.

[153] E. M. Cepollaro, S. Cimino, L. Lisi, M. Biesuz, B. Santhosh, and G. D. Sorarù, "Ru/Al2O3 on Polymer-Derived SiC Foams as Structured Catalysts for CO2 Methanation," *Catalysts*, vol. 12, p. 956, Sept. 2022. Number: 9 Publisher: Multidisciplinary Digital Publishing Institute.

[154] S. Carstens, K. Dammler, M. Scheffler, and D. Enke, "Reticulated Alumina Replica Foams with Additional Sub-Micrometer Strut Porosity," *Advanced Engineering Materials*, vol. 21, p. 1900791, Dec. 2019.

[155] T. Fey, U. Betke, S. Rannabauer, and M. Scheffler, "Reticulated Replica Ceramic Foams: Processing, Functionalization, and Characterization," *Advanced Engineering Materials*, vol. 19, no. 10, p. 1700369, 2017. _eprint: https://onlinelibrary.wiley.com/doi/pdf/10.1002/adem.201700369.

[156] G. Busca, "Chapter Three - Structural, Surface, and Catalytic Properties of Aluminas," in *Advances in Catalysis* (F. C. Jentoft, ed.), vol. 57, pp. 319–404, Academic Press, Jan. 2014.

[157] R. T. K. Baker, M. A. Barber, P. S. Harris, F. S. Feates, and R. J. Waite, "Nucleation and growth of carbon deposits from the nickel catalyzed decomposition of acetylene," *Journal of Catalysis*, vol. 26, pp. 51–62, July 1972.